Flicker propagation in radial and interconnected power systems

Sankika Tennakoon
University of Wollongong

Flicker Propagation in Radial and Interconnected Power Systems

A thesis submitted in fulfilment of the

requirements for the award of the degree

Doctor of Philosophy

from

University of Wollongong

by

Sankika Tennakoon, BSc(Eng)

School of Electrical, Computer and Telecommunications Engineering

March 2008

Dedicated to my parents...

Acknowledgements

This thesis would not have become a realisation without the contributions from many people.

First and foremost I wish to express my utmost gratitude to my supervisor, Associate Professor Sarath Perera for enabling me to pursue postgraduate studies at the University of Wollongong. You have always been more than a supervisor to me. I admire your commitment, patience and the academic and moral support given throughout my postgraduate studies. I am indebted to you for guiding me to grow up academically and personally over last few years.

I would also like to thank Dr. Duane Robinson, former co-supervisor for his assistance during the early stages of the project. Thanks also go to my current co-supervisor Professor Danny Sutanto as well for assistance provided. I am grateful to TransGrid for financially supporting the project and to Dr. Don Geddey for providing valuable technical inputs. The assistance received from Sean Elphick in setting up the laboratory experiments and data analysis is appreciated. Many thanks to Tracey and Roslyn in School office for their generous support at various occasions.

Very special thanks go to my friends Prabodha, Radley, Kalyani and Nishad for all the support given during good times as well as hard times along the way. I was lucky to have you all around me to share memories over the last few years in Wollogong.

I would also like to thank my husband, Chaminda who became a part of my life recently for being supportive and understanding especially during the final stages of the research.

Finally, my heartiest gratitude goes to my parents, sister, brother-in-law and two nephews for being such a wonderful family to me. Thank you so much for your endless love, encouragement, guidance and all the sacrifices you all made on behalf of me to come this far. I owe my success to you.

Certification

I, Sankika Tennakoon declare that this thesis, submitted in fulfilment of the requirements for the award of Doctor of Philosophy, in the School of Electrical, Computer and Telecommunications Engineering, University of Wollongong, is entirely my own work unless otherwise referenced or acknowledged. This manuscript has not been submitted for qualifications at any other academic institute.

Sankika Tennakoon

Abstract

Voltage fluctuations which cause lamp flicker tend to propagate from the point of origin to various parts of a power system exhibiting some level of attenuation depending on factors such as system impedances, composition of loads and frequency components of the fluctuating waveform. Maintaining the flicker levels at various busbars below the planning limits specified by the standards is crucial, and in this regard it is important to develop an insight into the manner in which the flicker propagates via systems operating at different voltage levels. This thesis presents flicker transfer analysis methodologies applicable for radial and interconnected power systems particularly considering the influence of induction motor loads on flicker attenuation.

In the first phase of the work, development of the foundations towards flicker transfer analysis methodologies is carried out by investigating the stand-alone behaviour of induction motors that are subjected to regular supply voltage fluctuations. The electrical and mechanical response of induction motors to two types of sinusoidal fluctuations in the supply voltage where (a) a positive or negative sequence sinusoidal frequency component is superimposed on the mains voltage and (b) mains voltage amplitude is sinusoidally modulated are examined. State space representation of induction motors is used to develop a linearised induction motor model describing the response of the stator current and the rotor speed to small voltage variations in the supply voltage. The results from the model reveal that various sub-synchronous and/or super-synchronous frequency components that exist in the supply voltage as small voltage perturbations can influence the dynamic response of the machine in relation to flicker. In particular, oscillations in the electromagnetic torque and rotor speed arising as a result of the applied voltage perturbations are found to be the key influencing factors controlling the stator current perturbations. It has been noted that, the speed fluctuation caused by a superimposed positive sequence voltage

perturbation tends to produce extra emf components in the rotor which in turn can reflect back to the stator. This concept of multiple armature reaction has been found to be significant in large motors especially when the superimposed frequencies are closer to the fundamental frequency.

The second phase of the work covers the development of systematic methods for evaluation of flicker transfer in radial and interconnected power systems taking the dynamic behaviour of induction motors into account. In relation to radial systems, small signal models are developed which can be used to establish the flicker propagation from a higher voltage level (upstream) to a lower voltage level (downstream) where induction motor loads are connected. Although this method can be applied for regular or irregular voltage fluctuations, emphasis has been given to sinusoidal voltage fluctuations arising from conventional sinusoidal amplitude modulation of upstream voltage. Moreover, the method examines the propagation of sub-synchronous and super-synchronous frequency components that exist in the supply voltage as side bands and hence determines the overall attenuation in the voltage envelope. The contribution of induction motors of different sizes and other influential factors such as system impedance, loading level of the motor are examined. It has been noted that in general higher frequency components of the upstream fluctuating voltage envelope tend to attenuate better at the downstream. A method is also presented which allows aggregation of induction motors at the load busbars in relation to flicker transfer studies.

In relation to interconnected systems, a frequency domain approach which can be used to investigate the flicker transfer is presented. This approach can be considered as an extension to the impedance matrix method as described in the literature and can overcome some of the limitations of the latter method. In the proposed approach, induction motor loads are modelled in a more realistic manner to replicate

their dynamic behaviour, thus enabling the examination of the frequency dependent characteristics of flicker attenuation due to induction motors and the influence of tie lines in compensating flicker at remote load busbars consisting of passive loads.

To verify some of the theoretical outcomes real time voltage waveforms captured from a large arc furnace site have been used, in addition to the experimental work using a scaled down laboratory set up of a radial power system.

List of Principal Symbols

δ_i	voltage angle of i$^{\text{th}}$ node [degree]
Δi	variation in stator current [pu]
Δi_{ds}, Δi_{qs}	d-q axes stator current variations [pu]
ΔP	active power drawn by the motor at frequency f_i [kW]
ΔQ	reactive power drawn by the motor at frequency f_i [kVAr]
Δv	magnitude of voltage fluctuation [pu]
Δv_s	variation in amplitude of the supply voltage [pu]
E_{Psti}	flicker emission limit of an individual load
F	coincidence factor
f_b	fundamental frequency [Hz]
f_c	cut-off frequency [Hz]
f_i	superimposed sub-synchronous or super synchronous frequency [Hz]
f_m	modulation frequency [Hz]
f_r	rotor speed (electrical) [Hz]
ϕ_b	phase angle of fundamental frequency [rad]
ϕ_m	phase angle of modulating signal [rad]
G_{Pst}	global flicker contribution
H	inertia constant
I_p	amplitude of line current
J	moment of inertia [kgm^2]
k	load torque constant
L_{Pst}	short term flicker planning level
m	modulation depth (factor)
ω_b	base angular frequency [rad/s]

ω_e	synchronous speed (angular) [elec rad/sec]
ω_m	modulation frequency (angular) [rad/sec]
ω_r	rotor speed (angular) [elec rad/sec]
p	$\frac{d}{dt}$ operator
P_{it}	instantaneous flicker sensation
P_{st}	short term flicker severity index
P_{lt}	long term flicker severity index
r'_r	rotor resistance (referred to the stator) [Ω]
r_s	stator resistance [Ω]
ψ_d, ψ_q	d-q axes flux linkages per second [V]
ψ'_d, ψ'_q	d-q axes flux linkages per second referred to the stator [V]
s	Laplace operator
S_i	consumer's agreed power [MVA]
S_{tMV}	total supply capacity at a MV busbar [MVA]
S_{tHV}	total supply capacity at a HV busbar [MVA]
T_e	electromagnetic torque [Nm]
T_L	load torque [Nm]
$T_{Pst_{AB}}$	flicker transfer coefficient from A to B
T_{LSB}, T_{USB}	transfer coefficients of lower and upper side band voltages
u	control (input) vector
v_d, v_q	dq axes voltages [V]
v'_d, v'_q	dq axes voltages referred to stator [V]
V_m	peak value (amplitude) of the modulating signal [V]
V_p	amplitude of line-to-neutral voltage [V]
x	state vector
X'_{lr}	stator leakage reactance (referred to the stator) [Ω]

X'_d	sub transient reactance of the generator
X_{ls}	stator leakage reactance [Ω]
X_M	mutual reactance [Ω]
y	output vector

subscripts:

s stator variables

r rotor variables

o steady state values

Publications arising from this Thesis

1. S. Tennakoon, L. Perera, S. Perera and D. Robinson, *Flicker Transfer Analysis in Radial Power System*, Proc. Auastralasian Universities Power Engineering Conference (AUPEC 2004), Paper ID: 190, September 2004, Brisbane, Australia.

2. S. Tennakoon, S. Perera and D. Robinson, *Response of Mains Connected Induction Motors to Low Frequency Voltage Fluctuations from a Flicker Perspective*, Proc. Auastralasian Universities Power Engineering Conference (AUPEC 2005) (ISBN: 1 86295 277 9), Volume 2 pp 610-614, September 2005, Hobart, Australia.

3. S. Tennakoon, and S. Perera, and D. Robinson, *Attenuation of Flicker by Induction Motor Loads: A Laboratory Investigation*, Proc. 12^{th} International Conference on Harmonics and Quality of Power (ICHQP 2006), October 2006, Cascais, Portugal.

4. S. Tennakoon, S. Perera, and D. Robinson, *Flicker Attenuation Part I: Response of Three-Phase Induction Motors to Regular Voltage Fluctuations*, Paper ID: TPWRD-00828-2006, IEEE Transactions on Power Delivery (in print).

5. S. Tennakoon, and S. Perera, and D. Robinson, *Flicker Attenuation - Part II: Transfer Coefficients for Radial Power Systems with Induction Motor Loads*, Paper ID: TPWRD-00829-2006, IEEE Transactions on Power Delivery (in print).

6. S. Tennakoon and S. Perera, and D. Sutanto, *Flicker Propagation in Interconnected Power Systems*, Proc. of IEEE PES PowerAfrica 2007, Conference and Exposition in Africa (ISBN: 1 4244 1478 4), July 2007, Johannesburg, South Africa.

Table of Contents

List of Figures

List of Tables

Chapter 1

Introduction

1.1 Statement of the Problem

An increased level of attention is now being paid to the quality of electrical power supply by utilities, customers and equipment manufacturers due to a number of reasons, including deregulation of the electricity industry. Among many power quality problems, voltage fluctuations leading to lamp flicker is well understood to be caused by active and reactive power variations of large intermittent loads such as electric arc furnaces. Such fluctuating loads are usually supplied through dedicated feeders connected to upstream high voltage (HV) busbars (point of common coupling - PCC) through which the generated voltage fluctuations can penetrate into other parts of the power system.

In relation to radial power systems, the flicker originating at the lower voltage level (downstream) transfers to the higher voltage level (upstream) with significant attenuation due to the large difference between the fault levels. However, flicker that is present at an upstream point (e.g. PCC of a fluctuating load) transfers to downstream busbars with little or some level of attenuation depending on factors such as feeder impedances, composition of loads at the downstream and frequency

components of the fluctuating voltage envelope.

Recent work related to flicker propagation has revealed that industrial loads consisting of a large proportion of dynamic loads, such as mains connected induction motors, assist in attenuating flicker better compared to residential loads which are normally considered to consist of passive components. Although significant research outcomes exist on general aspects of flicker propagation, such as evaluation of flicker levels in power systems with respect to the origin of flicker or PCC, the influence of dynamic loads on flicker propagation and attenuation has not been carefully investigated.

In existing flicker transfer analysis methods, the influence of downstream industrial loads containing induction motors on flicker attenuation has been justified using the argument that the dynamic impedance offered by an induction motor under fluctuating supply conditions is relatively small compared to its steady state impedance, which prevails under normal supply conditions. The definition of a constant dynamic impedance of an induction motor is a hypothetical concept and a representation of an induction motor by such a static impedance is not justifiable as the voltage fluctuations caused by a disturbing load normally contain numerous sub-synchronous and super-synchronous frequency components and the response of an induction motor to these frequency components could be different at each frequency, thus affecting the level of flicker attenuation to varying levels. As such, it is evident that existing flicker transfer analysis techniques do not provide theoretical relationships between the flicker levels and the busbar load composition and related aspects such as the influence of induction motor loads on flicker attenuation. These relationships can only be determined by modelling and investigating the response of the different load types to supply voltage variations and by incorporating the influence of the dynamic loads such as induction motors on flicker attenuation into flicker transfer analysis methods.

It is vital to develop an insight on the manner in which the voltage fluctuations and hence flicker propagate through different voltage levels in a power system. This is an aspect of flicker which can help further development of relevant standards.

1.2 Research Objectives and Methodologies

The aim of the work presented in this thesis is to broaden the understanding on flicker propagation in power systems by developing flicker transfer analysis methodologies applicable for radial and interconnected systems considering the influence of induction motor loads on flicker attenuation. These methodologies include extensions to existing techniques, development of new approaches and experimental work that can be used to comprehend the theoretical findings.

It is vital to understand the stand-alone behaviour of induction motors that are subjected to fluctuations in the mains voltage in order to identify their dynamic characteristics in relation to flicker attenuation. Thus, the first objective of the thesis is to investigate the electrical and mechanical response of induction motors subjected to small regular voltage fluctuations in the supply voltage using appropriate methods. This is accomplished by the development of a linearised induction motor model which can be used to determine the responses of the stator current and the rotor speed to sinusoidal voltage fluctuations in the supply. Two types of regular voltage fluctuations have been considered, where (a) a positive or negative sequence low frequency component is superimposed on the mains voltage and (b) amplitude of the mains voltage is sinusoidally modulated using a single low modulation frequency.

The second objective is to develop a methodical approach that can be used to investigate the flicker propagation from a higher voltage level (upstream) to a lower voltage level (downstream) of a radial system taking the dynamic behaviour of induction motor loads that are connected to the downstream into account. Small signal

models are extended in order to establish the propagation of voltage fluctuations caused by conventional sinusoidal amplitude modulation at the upstream, a case which is commonly referred to in flicker related studies. As the method is based on the sinusoidal voltage variations, determination of transfer coefficients takes the frequency of the voltage fluctuation into account. The propagation of individual voltage perturbations that exist as sub-synchronous or super-synchronous frequency components will be evaluated which in turn can be used to predict the overall attenuation in the voltage envelope at downstream.

The outcomes of the theoretical studies in relation to radial systems are supported through laboratory experiments. The test rig used for the experiments replicates a scaled down radial system of which the downstream consists of an induction motor and an equivalent passive load which can be tested independently. Flicker propagation in a typical sub-transmission system is also studied using real time waveform data with the objective of examining the validity of the theoretical predictions in relation to flicker transfer.

Another objective of this thesis is to broaden the flicker transfer analsyis methods in relation to interconnected systems. The existing methods are revised to develop a frequency domain approach suitable for determination of flicker transfer in meshed systems in a more realistic manner. The validity of the assumptions which are made in existing methods is examined with a view to make recommendations in relation to practical scenarios.

1.3 Outline of the Thesis

A brief description on the contents of the remaining chapters is given below:

Chapter 2 is a literature review on the background information required to carry out the work presented in the thesis. This chapter gives a brief overview on the past

developments in research related to flicker propagation and emphasises the procedures prescribed in standards to limit the flicker levels.

Chapter 3 describes the methodology and the results of preliminary investigations in relation to flicker transfer in radial systems using time domain simulations. The results which clearly demonstrate the influence of induction motor loads on flicker attenuation are utilised in later sections of the thesis to verify the findings from the theoretical modelling.

Chapter 4 presents the investigations which are carried out on the stand-alone behaviour of induction motors that are operating under fluctuating supply conditions. The first stage of this chapter examines the stator current and the rotor speed variations due to small voltage fluctuations in the supply using large signal analysis and a conventional d-q domain induction motor model. A linearised motor model is presented in the second stage which relates the rotor speed oscillations to the stator current. The model examines the dynamic behaviour of an induction motor caused by voltage fluctuations taking place at frequencies between 20Hz and 100Hz. This chapter also provides insight into the multiple armature reaction which arises as a result of voltage fluctuations.

The work presented in Chapter 4 is extended in Chapter 5 in order to develop a systematic approach to analyse the flicker propagation in a radial network that contains induction motor loads. A small signal model of an induction motor is presented in order to determine attenuation of flicker caused by sinusoidal amplitude modulation. Voltage transfer coefficients predicted from small signal models are compared with those established from large signal models. An effective sub-synchronous or super-synchronous impedance of the motor is defined in order to justify the frequency dependency of transfer coefficients. Investigations are carried out on induction motors of several ratings and the results of which are used to illustrate the depen-

dency of flicker attenuation on the rating of a motor. The advantages and limitations of small signal analysis in relation to flicker transfer studies are also discussed.

The methodology, measurements and the data analysis of laboratory experiments carried out using a scaled down radial network are explained in Chapter 6. Analysis of on-line and off-line flicker measurements are compared with the trends established from theoretical modelling in Chapter 4.

Chapter 7 describes the work related to flicker transfer in interconnected systems. The validity of the assumptions made in the existing methods are examined. A frequency domain method which allows the investigations of propagation of flicker caused by sinusoidal fluctuations in interconnected systems is presented. In the proposed method, induction motor loads are represented as dynamic entities rather than static impedances hence permitting assessment of frequency dependent characteristics in flicker attenuation. A method is also presented for aggregation of induction motors at the load busbars for flicker transfer studies.

Finally, Chapter 8 summarises the major outcomes of the work presented in the thesis and makes recommendations and suggestions for future work.

Chapter 2

Literature Review

2.1 Introduction

This chapter presents a brief introduction to voltage fluctuations and flicker followed by a critical review on the existing knowledge in relation to flicker propagation. Key concepts behind characterisation and measurement of flicker are briefly described. Principles of flicker propagation in radial and interconnected systems are discussed and the existing knowledge on the methods of analysis are reviewed. The major contributions made by other researchers to the subject of flicker studies are examined in order to identify the necessity for further research. An overview of the relevant standards on assessment and allocation of emission limits of fluctuating loads in both MV and HV systems is given emphasising the relevance of flicker transfer coefficient. Finally, data analysis of a synchronous flicker measurement campaign is presented which provides further supportive information for the latter parts of the thesis.

2.2 Voltage Fluctuations and Flicker

The International Electrotechnical Vocabulary (IEV 161-08-13) [1] defines flicker as 'the impression of unsteadiness of visual sensation induced by a light stimulus whose illuminance or spectral distribution fluctuates with time'. Thus flicker can be considered as a physiological quantity rather than simply a physical quantity since the impression of visual sensation may vary from person to person. Physically, flicker can be considered as variations in the illumination intensity of electric lighting devices caused by the fluctuations in its supply voltage. Although lamp flicker is caused by voltage fluctuations in the supply, the latter is commonly referred as voltage flicker simply to represent the overall power quality disturbance [2, 3]. For this reason, propagation of voltage fluctuations will be interchangeably used to refer to propagation of flicker.

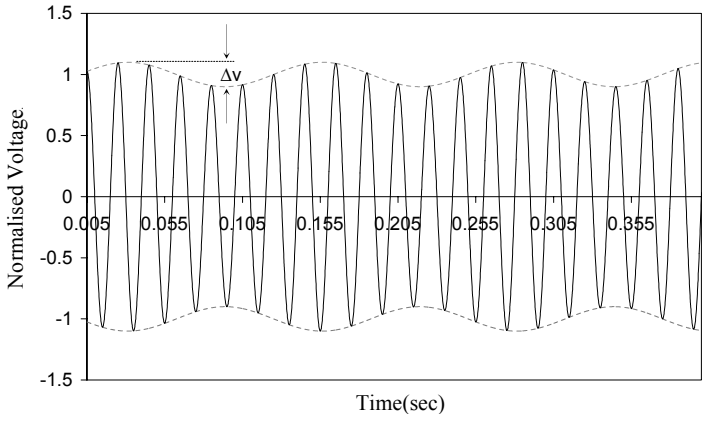

Figure 2.1: Sinusoidal flicker due to amplitude modulation of fundamental frequency with a single modulating component

Figure 2.1 illustrates the voltage fluctuations arising from sinusoidal amplitude modulation (AM), a classical case of flicker where the voltage envelope fluctuates sinusoidally. The corresponding instantaneous voltage can be expressed as:

$$v(t) = V_p(1 + m\sin(2\pi f_m t))\cos(2\pi f_b t) \tag{2.1}$$

where,

V_p	-	amplitude (nominal) of the fundamental ac voltage
f_b	-	fundamental frequency
f_m	-	modulation frequency
$m = \Delta v/2V_p$	-	modulation depth
Δv	-	magnitude of voltage fluctuation

The perceptibility of flicker depends on the magnitude (Δv) and the frequency (f_m) of voltage fluctuations. Flicker frequencies in the range of 0.05Hz-35Hz can cause perceptible flicker [3, 4]. The human eye is most sensitive to flicker around 8.8Hz and at this frequency Δv as small as 0.25% would be sufficient to produce perceptible flicker [4, 5].

The spectral components of the an AM signal given by (2.1) can be established as:

$$v(t) = V_p \cos(2\pi f_b t) + \frac{mV_p}{2} \sin 2\pi(f_b + f_m)t - \frac{mV_p}{2} \sin 2\pi(f_b - f_m)t \qquad (2.2)$$

According to (2.2), $v(t)$ contains two sidebands, one at a super-synchronous frequency ($f_b + f_m$) and another at a sub-synchronous frequency ($f_b - f_m$), in addition to the component at fundamental frequency (f_b). Associated with typical voltage fluctuations, such spectral components can exist individually or as combinations of various frequency components that are superimposed on the fundamental frequency. An individual frequency component of relatively significant magnitude can result in frequency beating with the fundamental, leading to oscillations in the voltage envelope [3]. Therefore, the definition of flicker cannot be restricted to amplitude modulation. Presence of interharmonics or modulated harmonics would also lead to voltage fluctuations causing lamp flicker [3, 6, 7]. The effective magnitude and the phase of

the envelope would obviously depend on the magnitude and the phase relationships between the existing voltage perturbations.

The main sources of voltage fluctuations and flicker are large intermittent loads such as electric arc furnaces (EAFs) that are normally supplied through dedicated feeders connected to HV or MV busbars. The chaotic variations in the active and reactive power drawn by an EAF arise due to stochastic variations in arc length and the resulting voltage fluctuations in the low voltage side of the installation transformer could be reflected onto the HV side. Other major sources of flicker include frequent starting and stopping of large induction motors, operation of wind turbine systems, welders and cycloconverters [3].

2.3 IEC Flickermeter and Flicker Measurement

The theory associated with the IEC flickermeter is used as the widely accepted approach in quantifying the severity of flicker. The original design of the flickermeter is based on the specifications recommended by the International Union for Electroheat (UIE). The flickermeter simulates the process of physiological and visual perception in order to indicate the reaction of a human observer to regular or irregular voltage fluctuations.

Characterisation of flicker is carried out using flicker severity indices obtained from an IEC flickermeter. Short term flicker severity index (P_{st}) is established using measurements over a period of 10 minutes, which can be used to evaluate the severity of the disturbances that exist for relatively short time periods. The IEC flicker curve for regular rectangular voltage fluctuations, which corresponds to $P_{st} = 1$ [4, 8] is depicted in Figure 2.2 for three operating voltages of the incandescent lamp. The long term flicker severity index (P_{lt}) is evaluated over a period of 2 hours using 12 consecutive values of P_{st} and is suitable for measurement of the severity of the

disturbances that may persist over a few hours, days or weeks. The threshold value of P_{st} for perceptibility is unity.

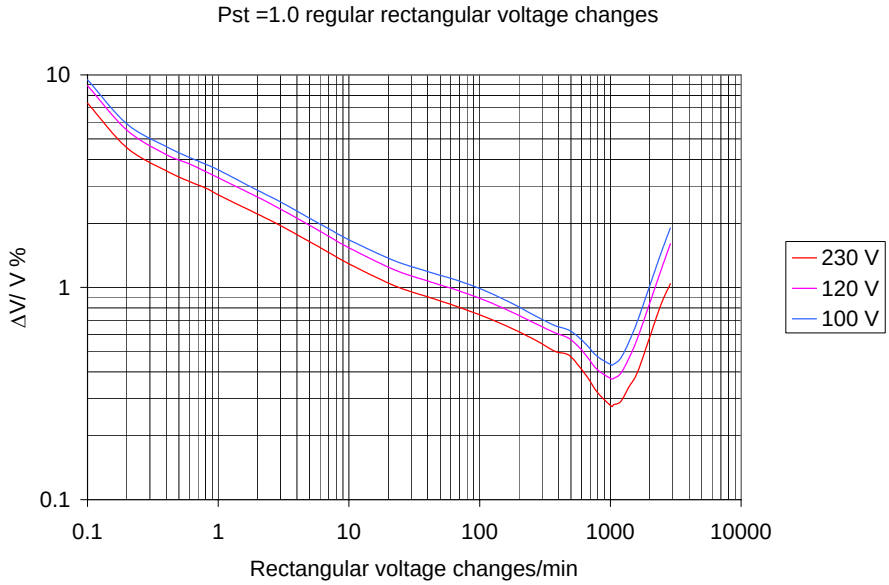

Figure 2.2: IEC flicker curve

The functional and design specifications of the flickermeter and the methodology of evaluating the flicker severity are described in IEC technical report [8] and has been adopted in Australia as a near identical Australian Standard AS/NZS 61000.4.15 [4]. The strategy for evaluating the flicker severity entails simulating the interaction of the fluctuating voltage signal with the non-linear combined lamp-eye-brain chain effect and associated statistical evaluation. The flickermeter monitors the individual and sequential voltage fluctuations in order to indicate the severity of flicker for regular or irregular voltage fluctuations independent of the flicker source.

Figure 2.3 illustrates the major blocks of the IEC flickermeter. A brief description of the functionality of each block is given below:

- Block-1 performs the normalisation of the mean rms value of the input voltage

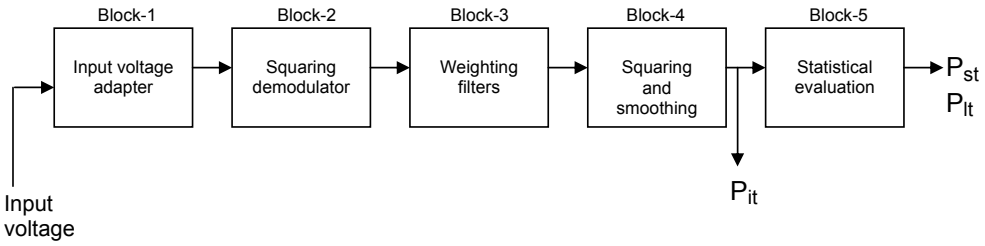

Figure 2.3: Major blocks of the IEC flickermeter

signal in order to make the measurement independent of very slow voltage fluctuations. It also provides an internal reference level for further calculations.

- Block-2 is a quadratic demodulator which extracts the fluctuating voltage signal by squaring the scaled input voltage thus simulating the behaviour of a lamp.

- Block-3 is composed of three filters connected in series. The first is a first order high-pass filter used to eliminate the dc component. The second is a sixth order Butterworth low-pass filter with a 35Hz, 3dB cut-off frequency and used to remove the signal components at twice the mains frequency at the demodulator output. The last filter provides a very specific weighting function which is a band-pass response, within the range of interest between 0.05 and 35Hz centred at 8.8Hz. The response is normalised for 8.8Hz sinusoidal modulation.

- Block-4 simulates the non linear eye-brain perception through the squaring of the weighted filter signal. In addition, it implements a sliding mean operator with a 300ms time constant to simulate the storage effect in the brain. The output of Block-4, the instantaneous flicker sensation (P_{it}) represents the visual perception of the average human observer.

- Block-5 performs the on-line statistical analysis of the flicker signal, P_{it}, which yields the flicker severity indices, P_{st} and P_{lt}.

Recent studies in relation to flicker measurement report many analytical techniques that can be employed to assess the flicker. Some of them utilise different implementation methods of IEC flickermeter [3] whereas some describe evaluation of flicker severity using approaches which are not in compliance with the IEC flickermeter [9]. In [3] a digital implementation of IEC flickermeter is described using time and frequency domain approaches. High computational efficiency can be achieved with time domain based measurements whereas frequency domain based measurements are seen to be relatively better in accuracy involved with demodulation and defining the weighting filters.

2.4 Flicker Propagation and Attenuation

2.4.1 An Overview on General Aspects

The voltage fluctuations caused by a large disturbing load are often substantially compensated at the premises itself by employing appropriate mitigation techniques such as static VAr compensators. Nevertheless, the secondary side of the HV/MV transformer of the installation may still carry relatively significant levels of real and reactive power fluctuations, leading to voltage fluctuations which eventually penetrate into the neighbouring parts of the power system through the connecting impedances. Propagation of flicker would take place with some level of attenuation depending on factors such as line and transformer impedances, the composition of loads and the frequency components that are present in the envelope of the fluctuating voltage. Thus, a single disturbing load can affect a large number of MV and LV customers unless the generated voltage fluctuations are adequately compensated.

There exists substantial research outcomes on general aspects of flicker yet few work is reported in relation to flicker propagation. Analysis of flicker propagation

using synchronous field measurements for establishment of transfer coefficients at various busbars of a network has been investigated in [10, 11, 12]. Correlation analysis has been used to demonstrate the transfer and attenuation of flicker. In addition to field measurements, [12] reports on modelling of arc furnace behaviour, yet the modelling of the other network components have not been discussed. Investigations on various case studies in relation to propagation of flicker caused by arc furnaces are reported in [13, 14, 15]. These are primarily based on time domain simulation work and hence lack detailed theoretical explanations on the manner in which the voltage fluctuations get attenuated at various voltage levels.

The principles of flicker propagation from a lower voltage level to a higher voltage level and vice versa and the existing knowledge on flicker transfer analysis methods for radial and interconnected systems will be explained in the following section.

2.4.2 Radial Systems - Downstream to Upstream Flicker Transfer

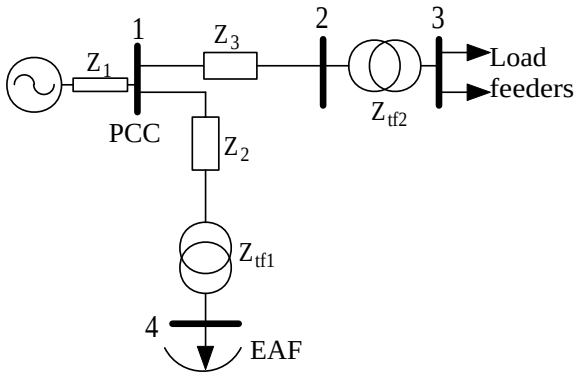

Figure 2.4: Radial system

The flicker transfer coefficient (T_{PstAB}) which determines the level of flicker at one location (B) with respect to another location (A) is defined by the ratio between the

P_{st} values measured over the same period as per [10]:

$$T_{PstAB} = \frac{P_{stB}}{P_{stA}} \tag{2.3}$$

The performance of the flickermeter is linear for voltage fluctuations of identical waveform shapes and hence P_{st} can be assumed to be proportional to the relative voltage change ($\frac{\Delta v}{v}$). With this assumption, for the radial network illustrated in Figure 2.4, flicker transfer coefficient in relation to upstream (busbar 1) and downstream (busbar 4) where the fluctuating load is connected can be established as:

$$T_{Pst41} = \frac{\Delta v_1 / v_1}{\Delta v_4 / v_4} = \Big| \frac{Z_1}{Z_1 + Z_{tf1} + Z_2} \Big| \tag{2.4}$$

where, Z_1 is the source impedance at the upstream, Z_2 is the line impedance and Z_{tf1} is the HV/MV transformer impedance, where all impedances are referred to the HV side. It is clear from (2.4) that due to the relatively large short circuit levels of the upstream busbars ($Z_1 << Z_{tf1} + Z_2$), flicker would be significantly attenuated as it transfers from downstream to upstream.

In a majority of the work reported in the literature in relation to radial networks, attention has been given to downstream to upstream flicker transfer especially in order to assess the flicker level at the PCC. Correlation analyses performed in [11, 12, 15] clearly demonstrate the reduction of flicker at the upstream locations as per (2.4).

In general, the short circuit levels are specified as contractual values in relation to voltage fluctuations related studies for MV and HV systems. Calculating the short circuit levels as per definitions specified in IEC standard [16] may result in conservative values which could lead to significant differences in measured and calculated flicker transfer coefficients between the downstream and the upstream PCC [17, 18]. The evaluation process of more realistic 'virtual' short circuit levels based on the

reactive power fluctuations arising as a result of the loads present and the actual operating voltage of the system is described in [17].

2.4.3 Radial Systems - Upstream to Downstream Flicker Transfer

Determination of flicker transfer from a higher voltage (upstream) to a lower voltage (downstream) is not as straightforward as that in relation to downstream to upstream, a difficulty arising as a result of the downstream loads. Upstream (HV PCC) to the downstream (MV) flicker transfer coefficients can be established as per (2.5), noting that the impedance offered by a downstream load to small voltage fluctuations in the supply is its dynamic value rather than the steady state static impedance. Again, all impedances in (2.5) are referred to the HV side.

$$T_{Pst13} = \frac{\Delta v_3/v_3}{\Delta v_1/v_1} = \left| \frac{Z'_{load}}{Z'_{load} + Z_{tf2} + Z_3} \times \frac{Z_{load} + Z_{tf2} + Z_3}{Z_{load}} \right| \tag{2.5}$$

where,

- Z_{tf2} - HV/MV transformer impedance
- Z_3 - line impedance
- Z_{load} - steady state impedance of the downstream load
- Z'_{load} - dynamic impedance of the downstream load

For a load mainly consisting of static components such as lighting and heating devices $Z_{load} \approx Z'_{load}$ and hence $T_{Pst13} \approx 1$. However, if the load consists of a significant proportion of induction motors, the combined dynamic load impedance would be relatively small compared to the corresponding steady state impedance, mainly arising as a result of the manner in which the motors behave when they are subjected to supply voltage fluctuations [10]. There has been no accepted definition on the dynamic impedance of an induction motor. However, Z'_{load} can be approximated as either the

transient impedance of the well known third order induction model or the locked rotor impedance as per [10, 19]. Accordingly the corresponding flicker transfer coefficient would be less than unity.

Equation (2.5) can also be used to examine the dependency of T_{Pst13} on the loading level of the transformer. If the downstream busbars are lightly loaded, i.e. relatively large Z_{load} and Z'_{load}, the flicker transfer coefficient would be close to unity.

Although the concept of dynamic impedance supports the argument behind the flicker attenuation due to the induction motor loads, the concept is deficient in providing a complete insight into the dynamics of motor loads which influence flicker attenuation. As suggested in [10, 19], the dynamic impedance is defined at mains frequency and hence the analysis would be restricted to rms variations in the fundamental supply voltage. In practice the voltage envelope may contain distinct flicker frequency components and the dependency of flicker transfer coefficient on the frequency of voltage fluctuation cannot be examined with such a fixed representation of induction motor loads.

The influence of dynamic loads on flicker attenuation has been noted in [10, 15, 11] through analysis of field measurement campaigns, yet the detailed theoretical studies are not seen to exist. The effect of loading level has been examined in [20], where a stochastic theory based method is employed to investigate the propagation of equivalent 10Hz flicker. However, the loads are modelled as P-Q elements and hence the influence of dynamic loads on flicker attenuation has not been taken into account.

2.4.4 Flicker Transfer in Interconnected Systems

Flicker propagation in interconnected systems can be noted to be one of the areas that has received least attention among other flicker related issues. Compared to radial systems, investigation of flicker propagation in interconnected networks needs

further refined methods which take the interaction between various busbars into account. Three possible methods can be found in the literature in relation to analysis of propagation of flicker in interconnected networks. Amongst them, the first method (a. Simplified Short Circuit Method) is proposed by IEC technical report 61000-3-7 [21] and AS/NZS 61000.3.7 [22]. Apart from the informative explanations given in [21] and [22], the aspect of flicker transfer in interconnected systems is studied only in [19] which suggests the second and the third methods (b. Impedance Matrix Method and c. Load Flow Method).

a. Simplified Short Circuit Method [21, 22]:

This approach is valid for the cases where a significant proportion of the sources of the short-circuit power at busbars can be considered to be electrically independent. Flicker transfer from node A to an adjacent node, B has been approximated by (2.6).

$$T_{PstAB} = \frac{S''_{cc,AB}}{S''_{cc,A} - S''_{cc,BA}} \tag{2.6}$$

where, $S''_{cc,A}$ is the fault level at A, $S''_{cc,AB}$ is the fault infeed at node B from node A and $S_{cc,BA}$ is the fault infeed at A from B. The main limitation associated with this method is the determination of fault infeed at one node from another when the two nodes are not adjacent to each other.

b. Impedance Matrix Method [19]:

This method is based on conventional short circuit analysis where the system admittance matrix is used to derive the transfer coefficients of voltage fluctuations between various busbars. Large induction motor loads are represented by their corresponding dynamic impedances, while all other loads are modelled as passive elements. As-

suming that all the impedances have the same angle, it can be shown that voltage fluctuations arising at i^{th} busbar due to voltage fluctuations at j^{th} bus is given by:

$$T_{Pstji} = \left| \frac{Z_{ij}}{Z_{jj}} \right| \tag{2.7}$$

where Z_{ij} and Z_{jj} are elements extracted from the impedance matrix. Since the network is analysed at the mains frequency, this method allows examination of the propagation of voltage disturbances in the rms voltage. Furthermore, due to the static representation of motor loads, determination of flicker transfer coefficient using the impedance matrix method does not take into account its modulation frequency dependency. The assumption of equal impedance angle would not be valid in general for all cases, especially for subtransmission and distribution systems.

c. Load Flow Method [19]:

In this approach loads are represented as P-Q nodes. The disturbing load is represented as an additional load that can be switched 'on' and 'off' at one of the nodes. The network is analysed with and without the additional load to determine the voltage change in the other nodes as:

$$\frac{\Delta v}{v} = \frac{|V_0| - |V_1|}{\frac{|V_0|+|V_1|}{2}} \tag{2.8}$$

where, V_0 is the voltage phasor without additional load and V_1 is the voltage phasor with the additional load node. Representation of the loads by constant power characteristics would lead to estimation of transfer coefficients based on static network impedances and hence the effect of dynamic loads has not been accounted for.

2.5 Electromagnetic Compatibility Standards for Flicker Allocation

2.5.1 The IEC Technical Report Type III (IEC 61000-3-7)/ Australian Standard (AS/NZS 61000.3.7)

The IEC technical report Type III, IEC 61000-3-7 [21] is considered to be an internationally accepted guide that can be used to manage flicker in MV/HV power systems. It outlines the methodologies for allocation of flicker to customers. It has also been adopted with subtle modifications by Standards Australia as a standard applicable in Australia and New Zealand (AS/NZS 61000.3.7) [22].

Standards Australia Guide Book HB 264 [23] is also available as a supplementary to AS/NZS 61000.3.7. Table 2.1 gives the indicative planning limits for high voltage (HV) and extra high voltage (EHV) systems as suggested by the standard [22].

Table 2.1: Indicative values of planning levels of flicker for HV and MV systems; 1kV<MV<35kV;35kV<HV<230kV

Index	MV	HV
P_{st}	0.9	0.8
P_{lt}	0.7	0.6

Maintaining the flicker levels at or below the planning levels at various voltage levels is crucial though it is not a mandatory requirement with many utilities at the moment unless called upon by codes or the regulator. However, the connection of a new fluctuating load to the existing HV or MV system may raise the total flicker level above an acceptable level and hence emission limits have to be allocated by the utility to individual customers during the planning phase. The emission level of a fluctuating load is the flicker level which would be produced at the PCC if no other fluctuating loads were present [22].

2.5.2 Global Flicker Emission in Radial Systems

Evaluation of an emission limit of a single fluctuating load requires determination of the 'global flicker contribution' (G_{Pst}), the total headroom available for the flicker emission at the corresponding voltage level in the given network. In determining G_{Pst} for a MV or HV system knowledge of the flicker transfer coefficient plays an important role. This can be explained using (2.9) which determines the global flicker emission for the medium voltage fluctuating loads (G_{PstMV}), where L_{PstMV} is the flicker planning level for the medium voltage level (downstream), L_{PstHV} is the flicker planning level for the high voltage level (upstream) and T_{PstHM} is the flicker transfer coefficient between HV and MV systems.

$$G_{PstMV} = \sqrt[3]{L_{PstMV}^3 - T_{PstHM}^3 L_{PstHV}^3} \tag{2.9}$$

A conservative value of unity can be used for T_{PstHM} in (2.9) without giving any consideration to the actual flicker transfer coefficient in the system. Nevertheless, a transfer coefficient less than unity (i.e. $T_{PstHM} < 1$) can be expected if the downstream (MV busbar) consists of a significant proportion of induction motor loads and consequently as per (2.9) more headroom would be available for medium voltage fluctuating loads for flicker emission. AS/NZS 61000.3.7 [22] does not spell out the means for deciding on T_{PstHM}. This can only be revealed either by analysing the downstream loads using suitable modelling techniques or by carrying out actual flicker measurements in the system.

Once the global flicker emission limit is determined, allocation of emission limits for individual fluctuating local loads (E_{Psti}) can be carried out based on the agreed power of consumer i (S_i) and the total supply capacity (S_{tMV}) of the MV system as per (2.10),

$$E_{Psti} = G_{PstHM} \sqrt[3]{\frac{S_i}{S_{tMV}} \frac{1}{F_{MV}}} \tag{2.10}$$

where, F_{MV} is the coincidence factor which has been used to accommodate the simultaneous operation of multiple fluctuating loads. However, based on the proposed revisions to IEC 61000-3-7 suggested by CIGRE-CIRED joint working group (JWG C41.03) [24], E_{Psti} will be determined as per (2.11) which ignores the coincidence factor (F_{MV}) all together.

$$E_{Psti} = G_{PstHM} \sqrt[3]{\frac{S_i}{S_{tMV} - S_{tLV}}} \tag{2.11}$$

where, S_{tLV} is the total power of the low voltage loads supplied directly including provision for future load growth.

2.5.3 Interconnected Systems

In relation to interconnected systems, determination of planning levels is poorly addressed in AS/NZS 61000.3.7. The standard does not describe methodology for the evaluation of the global flicker contribution. However, once a planning level for a given voltage level (e.g. HV) is established, apportioning the total planning level into individual loads can be carried out as per (2.12).

$$E_{Psti} = L_{PstHV} \sqrt[3]{\frac{S_i}{S_{tHV}}} \tag{2.12}$$

where, E_{PstHV} is the emission limit for user i, L_{PstHV} is the planning level for HV systems, S_i is the agreed power of consumer i and S_{tHV} is the total available power at the given busbar. As explained in [22], S_{tHV} can be calculated using (2.13), where the flicker contributions from neighbouring busbars, e.g. busbars B and C on another

busbar A, are taken into account using the influence coefficients K_{B-A} and K_{C-A}.

$$S_{tHV} = S_{tHVA} + K_{B-A}S_{tHVB} + K_{C-A}S_{tHVC} + ... \tag{2.13}$$

where S_{tHVB} and S_{tHVC} are the available power levels at busbars B and C respectively.

Similar to the radial system the influence coefficients K_{B-A} and K_{C-A} will depend on the composition of the loads connected at the various busbars. Establishment of influence coefficients can be carried out using one of the methods of analysis discussed in Section 2.4.4. Among those, the impedance matrix method has been found to be straightforward to implement as it is based on the principle of short circuit analysis at system mains frequency. The fluctuating load is considered as a current injection and the induction motor loads are represented by their dynamic impedances. Due to the crude representation of the dynamic loads, the effect of industrial load bases containing induction motors is not reflected in the calculated influential coefficients in a realistic manner.

2.6 Measurement of Emission and Establishment of Flicker Transfer Coefficient

Although IEC 61000-3-7 [21] and AS/NZS 61000.3.7 [22] outline the principles for assessing the emission limits for fluctuating loads to the public network, these documents do not prescribe methodologies on measurement and assessment of the emission level of a particular fluctuating load. Because of the background flicker, emission levels cannot be determined reliably by simply measuring the voltage fluctuations or flicker levels at the PCC.

The methods of assessing the emission level of a fluctuating load can be found in [18] and [25]. Among those, [25] describes three assessment methods. The first

method involves measurement of flicker levels at the secondary side of the installation transformer and transposing it to the primary side. However, this transposition is strictly valid only if the transformer is fully inductive and active power variations are negligible.

The second method proposed in [25] is based on a known impedance that can be considered as a reference impedance, such as the transformer feeding the fluctuating load. Simultaneous voltage waveform measurements on the two sides of reference impedance are used to calculate the emission level.

The third method involves measurements of the load current and the voltage at the PCC. The process of determination of emission level eliminates the background fluctuations by simulating the fluctuating component of the emission voltage, the voltage at the PCC due to the particular fluctuating load. This method can be considered as a refined approach compared to the first two methods. Assessment of emission level accounts for network resistance hence yields more accurate results compared to the second method, especially, when active power variations are significant and/or the network impedance angle is small.

Flicker transfer coefficient (T_{Pst}) from one location to another can be established using simultaneous flicker measurements carried out at the two locations [10, 11]. In this regard, scatter plots developed using short term flicker severity (P_{st}) or long term flicker severity (P_{lt}) indices are used to derive the flicker transfer coefficient. For example, Figure 2.5 illustrates the scatter plots of P_{st} values measured at two locations where P_{st} values at location 2 are plotted against P_{st} values at location 1 [11]. By forcing the linear regression line to pass through the origin, flicker transfer coefficient from location 1 to 2 ($T_{Pst_{12}}$), can be determined. The plots corresponding to three phases in Figure 2.5 indicate that the average value of $T_{Pst_{12}}$ is 0.841.

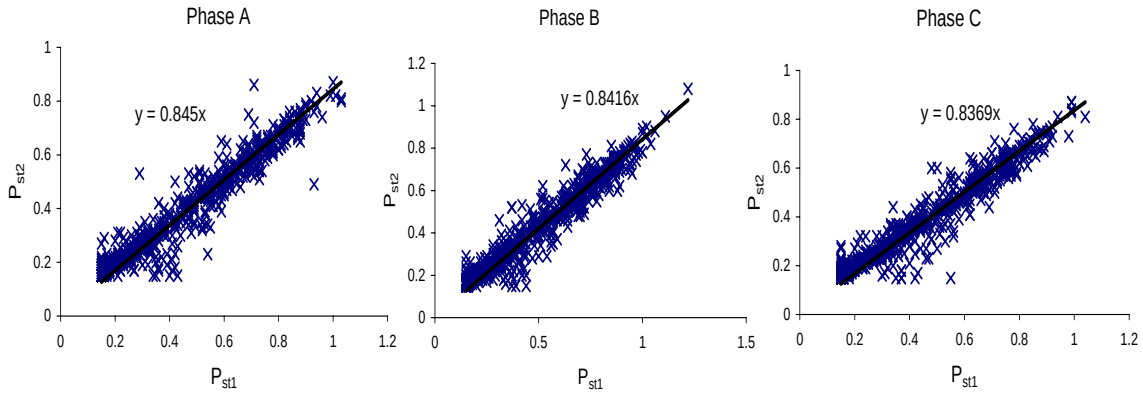

Figure 2.5: Scatter plot of the P_{st} values measured at two locations (1 and 2)

2.7 Summary

This chapter provided basic information in relation to voltage fluctuations and the related aspects such as measurement of flicker including the IEC flickermeter.

The existing knowledge and theory on flicker propagation and attenuation were covered in relation to radial and interconnected power systems.

Assumptions made in determining the flicker transfer from a upstream voltage level to a downstream voltage level are outlined. With regards to interconnected systems, the existing methods of analysis are discussed highlighting their relative merits and demerits.

A brief introduction to flicker allocation methodologies based on IEC methodologies was provided emphasising the relevance of flicker attenuation in establishing the emission limits to loads. The attenuation of flicker caused by dynamic loads such as induction motors was given due emphasis highlighting its relevance to flicker allocation methodologies.

Chapter 3

Preliminary Investigations on Flicker Transfer in Radial Systems using Time Domain Simulations

3.1 Introduction

As emphasised in Chapter 2, influence of industrial loads on flicker attenuation has been observed on a few occasions through field measurements [10, 11, 15], yet the behaviour of the motor loads under fluctuating supply conditions has not been the subject. Before embarking on theoretical modelling of induction machine dynamic behaviour, it is important to understand the fundamentals in relation to propagation of flicker from one voltage level to another in networks.

This chapter is focused on the methodology and analysis of results of time domain simulations of two major scenarios which are useful in the latter chapters of the thesis to compare with the outcomes of the theoretical work. The objective is to lay the foundation for the main body of the work in a simplistic yet methodical manner.

Section 3.2 of this chapter presents the analysis of a hypothetical radial network

representing a two busbar system using PSCAD/EMTDC transient analysis program. Measurement and analysis of data are discussed emphasising the important observations on major factors that influence the flicker transfer.

Section 3.3 covers the simulation of a sub-transmission network that consists of electrical arc furnace of 70MVA. The real time voltage waveforms captured on the 22kV side of the furnace installation transformer are used to regenerate the voltage fluctuations at the 132kV upstream PCC thus allowing examination of the propagation and attenuation of flicker at downstream busbars.

3.2 Simulation of a Hypothetical Radial Network Consisting of two Voltage Levels using PSCAD/EMTDC

3.2.1 Description of the Network and Flicker Measurement Criteria

Network Model:

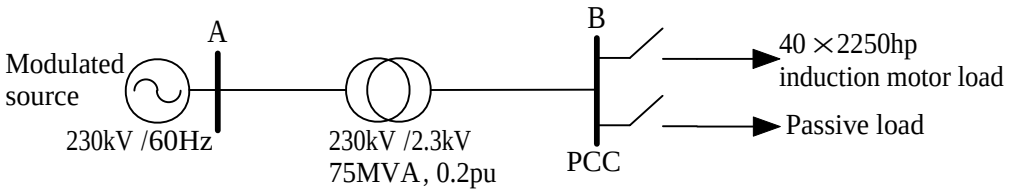

Figure 3.1: Radial system used for the simulations

The simple radial system shown in Figure 3.1 is used in the simulation work where only two voltage levels are considered for simplicity. Busbars A and B represent the upstream and downstream respectively. At downstream (B) individually switchable induction motor load and a passive R-L load are used allowing a pre-defined combination to be selected. The load classification is:

(a) Induction motor load: A cluster of 40, 2250hp motors. Specifications of a

single 2250hp motor are as given below:

rated voltage	-	2.3 kV
rated current	-	471 A
efficiency at full load	-	98.14%
power factor at full load	-	0.93 lagging
rated torque	-	9200Nm

The mechanical load on the induction motor is assumed to be pump type, of which the torque (T_L)-speed (ω_r) characteristics is given by:

$$T_L = k\omega_r^2 \tag{3.1}$$

where ω_r is the rotor speed and k is a constant. However, in Section 3.2.5 both pump type and constant torque type loads are used. Within PSCAD/EMTDC, each induction motor was modelled in EMTP type 40 format which takes deep bar effect into account.

(b) Passive load: A series connected passive R-L component of which the MVA rating and power factor are equivalent to those of the motor load at full load condition.

Upstream flicker is generated through sinusoidal amplitude modulation of the three phase voltage source - the process used is illustrated in Figure 3.2. The generated voltage fluctuations in the three phases is shown in Figure 3.3 for a modulation depth (m) of 0.05 and modulation frequency (f_m) of 10Hz.

Following aspects were investigated in the simulations carried out.

- Dependency of flicker attenuation on different downstream load compositions.
- Dependency of flicker attenuation on different downstream loading levels.

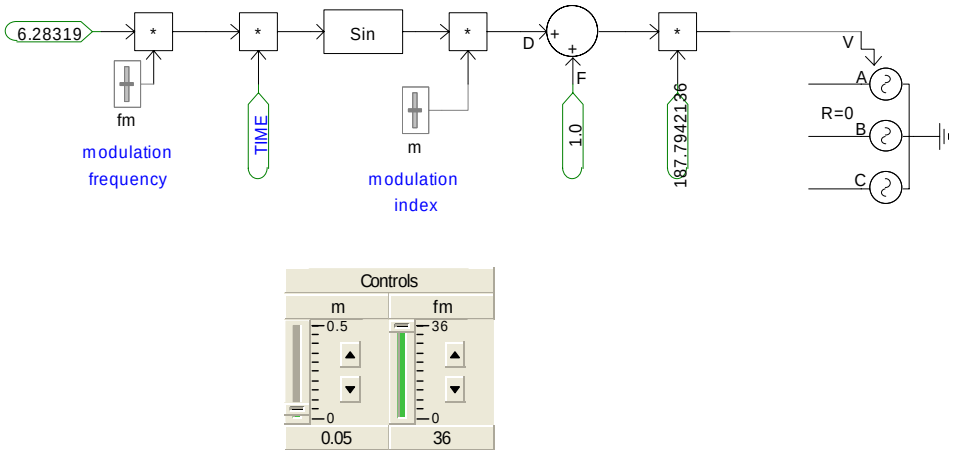

Figure 3.2: Control blocks used for amplitude modulation of upstream voltage in PSCAD/EMTDC

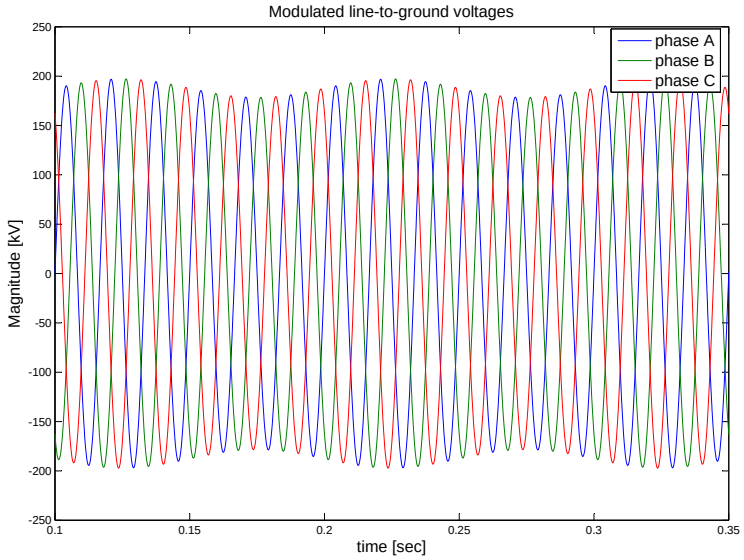

Figure 3.3: Upstream voltage fluctuations generated by amplitude modulating the three phase source voltage

- Dependency of flicker transfer on modulation frequency.
- Dependency of flicker transfer on magnitude of the upstream voltage fluctuation.
- Dependency of flicker transfer on downstream induction motor loads with different mechanical load types (pump load, constant torque loads)

Although only the results of the preliminary investigations are presented in this chapter, critical review of these results will be given in Chapters 4 and 5.

Measurement of Flicker:

One or more of the following methods were used for the measurement of flicker and evaluation of flicker transfer coefficient between upstream (A) and downstream (B).

(a) PSCAD/EMTDC based flickermeter: The first four blocks of the IEC flickermeter [5] were modelled in PSCAD/EMTDC where the instantaneous flicker sensation (P_{it}) is employed, noting that for regular voltage fluctuations $P_{st}^2 \propto P_{it}$. Hence the flicker transfer coefficient ($T_{Pst_{AB}}$) can be written as:

$$T_{Pst_{AB}} = \frac{P_{st_B}}{P_{st_A}} = \sqrt{\frac{P_{itB}}{P_{itA}}} \tag{3.2}$$

(b) MATLAB based flickermeter: A complete implementation of the IEC flickeremeter [5, 8] using MATLAB [26] was used to establish the flicker transfer coefficient employing short term flicker severity indices.

(c) RMS voltage fluctuations ($\frac{\Delta v}{v}$): Fluctuation in the rms voltage was determined using rms meters available in PSCAD/EMTDC. For regular voltage fluctuations, flicker severity can be assumed to be linearly proportional to the relative voltage and hence flicker transfer coefficient can be established as:

$$T_{PstAB} = \frac{\Delta v_B / v_B}{\Delta v_A / v_A} \tag{3.3}$$

where subscripts A and B in (3.3) denote the measurements corresponding to upstream (A) and downstream (B).

3.2.2 Dependency of Flicker Attenuation on Different Downstream Load Compositions

(a) Different Proportions of Induction Motors with Constant Loading Level of the Transformer

Upstream flicker was generated at fixed modulating frequency (f_m) and fixed modulation depth (m). The number of induction motors at full load was varied while maintaining the total MVA load at downstream constant by adjusting the passive load. Flicker levels were established using (a) PSCAD/EMTDC flickermeter and (c) rms voltage fluctuations employing (3.2) and (3.3) respectively.

Figure 3.4 shows the variation of flicker transfer coefficient, as the number of induction motors as a percentage of a total of 40 induction motors is varied, at a fixed modulation frequency (f_m) of 8Hz and modulation depth (m) of 0.005. It is evident that a large population of induction motors will help attenuate the flicker to a better extent compared to an equivalent passive load.

(b) Constant Proportion of Induction Motor Load with Varying Transformer Loading Level

In order to demonstrate the influence of the loading level of the transformer on flicker attenuation simulations were carried out as described:

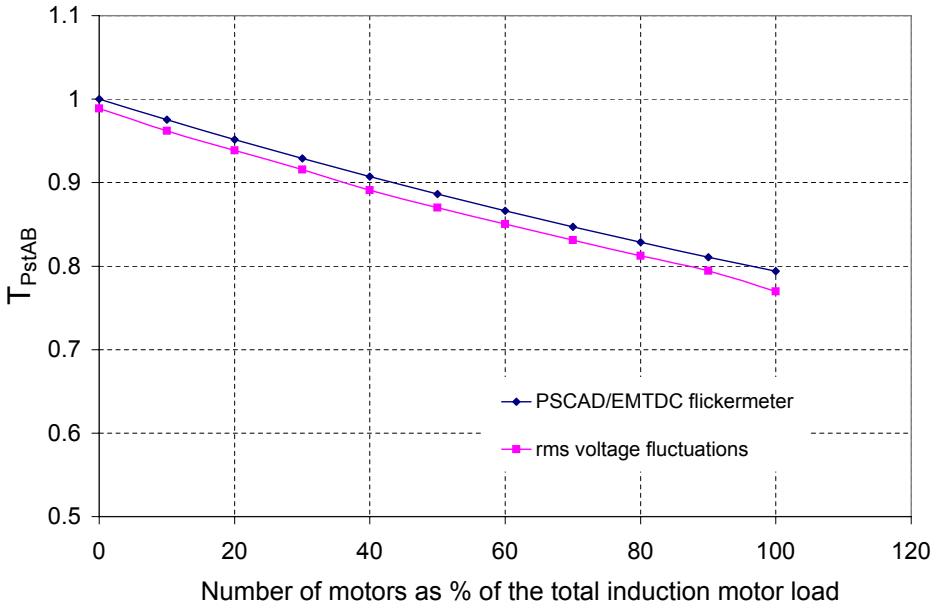

Figure 3.4: Variation of $T_{Pst_{AB}}$ with induction motor percentage

1. Vary the loading level of the 230kV/2.3kV transformer by varying the total MVA of the downstream load.

2. For each transformer loading level, the proportion of induction motors in relation to the total downstream load was varied as in Case (a) above.

Figure 3.5 illustrates the variation of $T_{Pst_{AB}}$ with both transformer loading level and the induction motor load percentage measured using the PSCAD/EMTDC flickermeter. It is seen that for a selected proportion of induction motors and passive load, as the loading level of the transformer increases, upstream to downstream flicker transfer attenuation would increase. Transfer coefficient approaches more or less unity for small induction motor proportions and/or transformer no-load conditions.

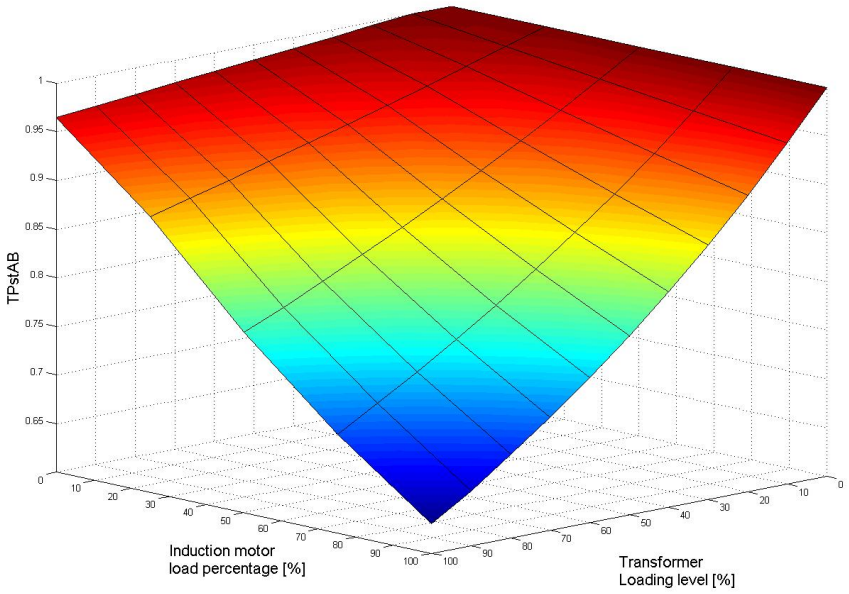

Figure 3.5: Variation of $T_{Pst_{AB}}$ with induction motor percentage and loading level

3.2.3 Dependency of Flicker Measurement on Modulation (Flicker) Frequency of Upstream Voltage

Flicker measurements were made at different modulation frequencies (f_m) for the cluster of 40 induction motors that operated at full load condition. The dependency of flicker transfer coefficient ($T_{Pst_{AB}}$) on modulation frequency (f_m) established using all three methods are illustrated in Figure 3.6 (f_m varied between 1Hz and 35Hz covering the perceptible flicker frequency range).

Figure 3.6 reveals that $T_{Pst_{AB}}$ established using all three methods are in reasonable agreement (except for errors arising as a result of manual reading of graphical outputs) while demonstrating its dependency on modulation frequency. Chapters 4 and 5 provide detailed treatment on the dynamics of the induction motors justifying this frequency dependent characteristics of flicker transfer.

Figure 3.7 illustrates the variation of $T_{Pst_{AB}}$ with both modulation frequency (f_m) and the proportion of the induction motor load. As explained in Section 3.2.1, pro-

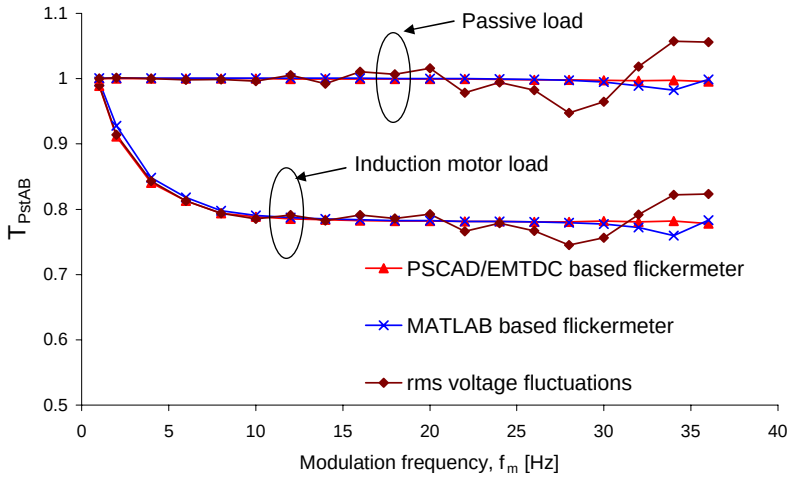

Figure 3.6: Variation of flicker transfer coefficient ($T_{Pst_{AB}}$) with modulation frequency (f_m)

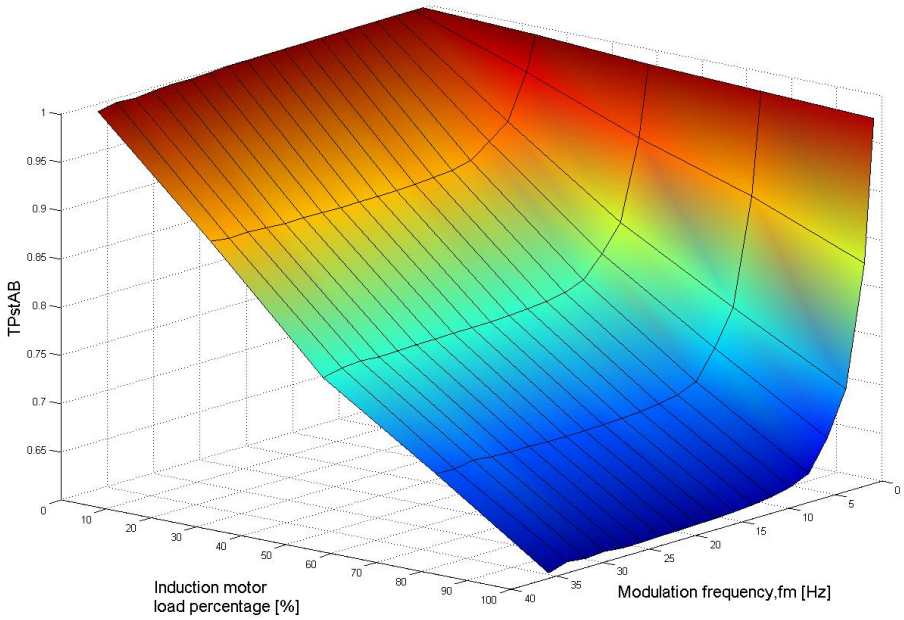

Figure 3.7: Variation of flicker transfer coefficient ($T_{Pst_{AB}}$) with modulation frequency (f_m) and the proportion of the induction motors downstream

portion of induction motor load is increased while decreasing the proportion of passive load such that the total MVA load at downstream is constant. It is evident from Figure 3.7 that dependency of flicker attenuation on modulation frequency is insignificant when the proportion of the passive load is high compared to the proportion of induction motors. Maximum flicker attenuation is obtained when the downstream consists entirely induction motors and the modulation frequency is greater than about 10Hz.

3.2.4 Dependency of Flicker Attenuation on the Magnitude of the Upstream Voltage Fluctuation

Simulation work was extended to determine the dependency of flicker transfer on the magnitude of upstream voltage fluctuation (Δv), which is achieved by varying the modulation depth (m). As there is reasonable agreement between the three different flicker measurement methods which were outlined in Section 3.2.1, for this case measurements were made using only the PSCAD/EMTDC based flickermeter.

Variation of the flicker transfer coefficient ($T_{Pst_{AB}}$) with modulation depth (m) is depicted in Figure 3.8, where m is varied between 0.02 to 0.2. The upper limit of this range of $m(=0.2)$ would give rise to voltage fluctuation (Δv) of 0.4 pu which is significantly larger then the typical values of magnitudes of Δv caused by fluctuating loads at upstream busbars. According to Figure 3.8, it is seen that the flicker transfer coefficient ($T_{Pst_{AB}}$) is more or less independent of the magnitude of the voltage fluctuation at upstream.

3.2.5 Dependency of Flicker Transfer on Mechanical Load type

Flicker measurements were made with downstream induction motor load at full load condition but with different load types; (a) pump load (b) constant torque load. Upstream modulating frequency was varied over 1Hz-36Hz while keeping the modulation

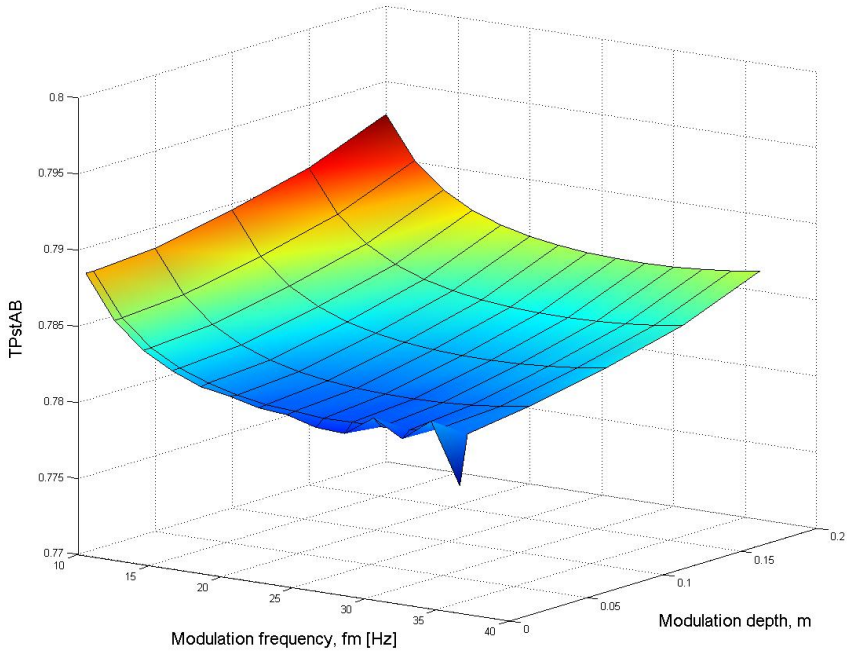

Figure 3.8: Variation of $T_{Pst_{AB}}$ with modulation depth (m)

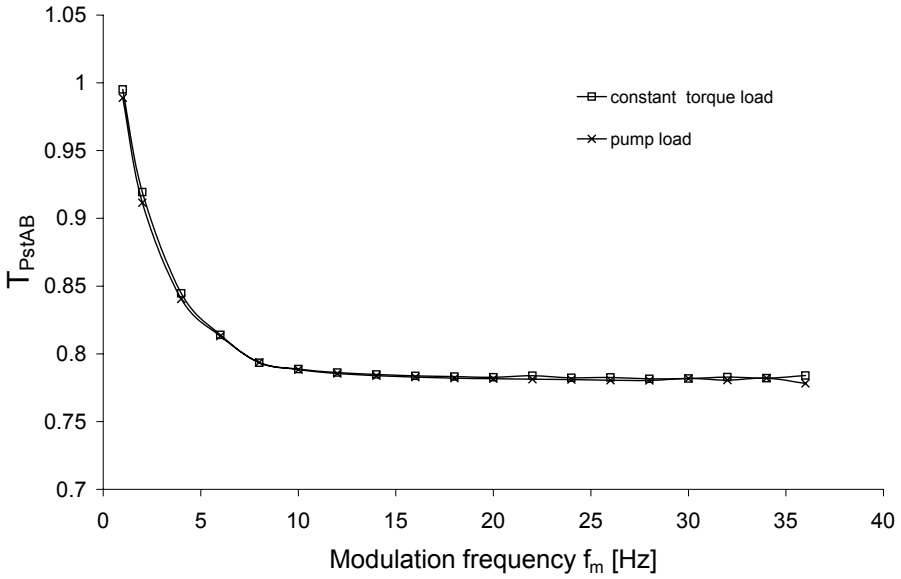

Figure 3.9: Variation of $T_{Pst_{AB}}$ with modulation frequency for two different load types

depth constant at 0.005.

Figure 3.9 depicts the variation of $T_{Pst_{AB}}$ with modulation frequency for the two types of the mechanical loads. It is seen form this figure that the shaft load type has no significant impact on the attenuation of flicker at the downstream.

3.3 Simulation of Flicker Propagation in a Real System

3.3.1 Network Configuration and Data Capturing System

The aim of this section is to examine the manner in which the voltage fluctuations propagate from an upstream voltage level to a downstream voltage level in a sub-transmission network using voltage waveforms captured in relation to the network shown in Figure 3.10. This network consists of a 70MVA electric arc furnace at site C supplied through a dedicated feeder connected to the upstream 132kV busbar (site A).

Measurement of three phase line-to-neutral voltage waveforms were carried out at the 22kV side of the transformer (132kV/22kV) at the arc furnace (site C) at a sampling rate of 10kHz. Data capturing was carried out over a period of 7 hours which was long enough to incorporate a few typical cycles of the furnace operation. Data recorded was read to a PC using appropriate tools for further processing.

The network of Figure 3.10 was simulated in PSCAD/EMTDC using waveform data captured at site C. The objective was to generate voltage fluctuations at the upstream 132kV busbar (site A) and subsequently examine the propagation of voltage fluctuations towards downstream locations (sites E and F).

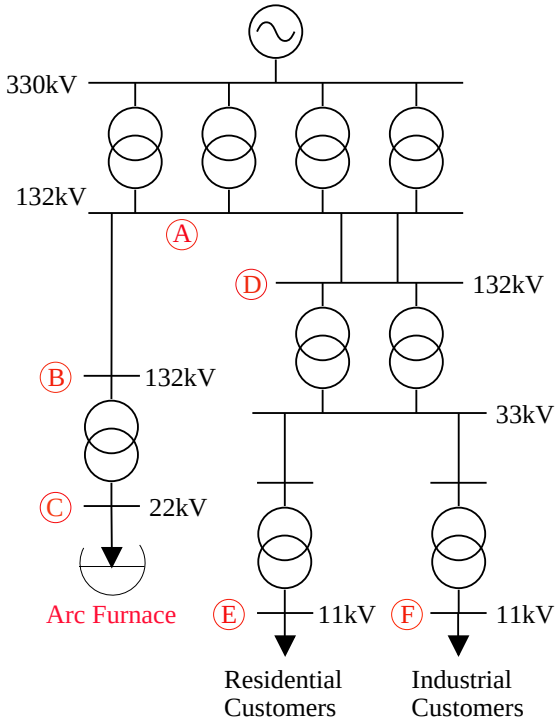

Figure 3.10: Single line diagram of the sub-transmission network used for the simulation

3.3.2 Reconstruction of Voltage Envelope at 132kV Upstream Busbar (Site A) and Simulations on Reduced Network Model

Voltage fluctuations generated by the furnace at site C can be expected to transfer to upstream 132kV (site A) with a reduction factor determined by the short circuit levels at the two sites as described by (3.4).

$$T_{Pst_{CA}} = \left| \frac{Z_s}{Z_s + Z_{line} + Z_{TF}} \right| \tag{3.4}$$

where,

$T_{Pst_{CA}}$ - Flicker transfer coefficient from site C to site A

Z_s - source impedance at 132kV busbar (site A)

Z_{line} - line impedance between sites A and B

Z_{TF} - impedance of the 132kV/22kV installation transformer at site C

The waveform data captured at site C can be used to extract the modulating frequency components of the three phase line-to-neutral voltages. The extracted modulating signals at site C can be scaled down using the reduction factor given by (3.4) in order to reconstruct the modulating signals and three phase line-to-neutral voltages at the upstream 132kV busbar (site A). The upstream source of the reduced network illustrated in Figure 3.11 can now be used to generate these reconstructed waveforms to examine the flicker propagation from site A to sites E and F.

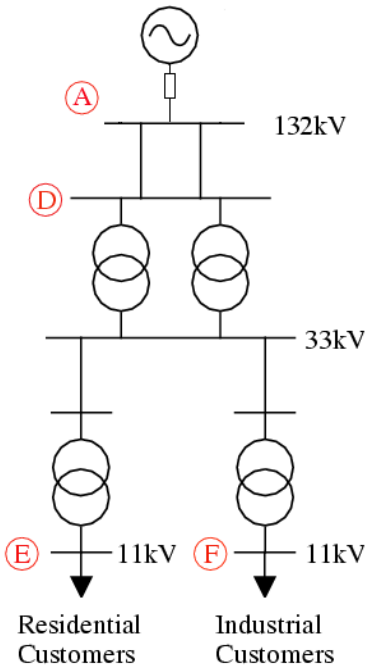

Figure 3.11: Reduced network model used in simulation

The following procedure was implemented in PSCAD/EMTDC to reconstruct the envelopes (modulating signals) of three phases line-to-neutral voltages at site A, where mathematical expressions are given in relation to phase A only.

1. Read the instantaneous voltage waveform data for site C into PSCAD/EMTDC.

2. For phase A, line-to-neutral voltage ($v_a(t)$) can be defined as:

$$v_a(t) = V_{pk-C}(1 + m_a(t)) \sin(2\pi f_b t + \phi) \tag{3.5}$$

where, V_{pk-C} is the nominal value of the amplitude of phase A line-to-neutral voltage, $m_a(t)$ is the modulating signal of $v_a(t)$ and ϕ is the phase angle of unmodulated $v_a(t)$. Extract the modulating signal of $v_a(t)$ using an appropriate demodulating technique. In the present work, square demodulation was used. This includes, squaring the waveforms followed by two high order filters used to remove the dc component and higher frequency components resulting from the squaring process.

3. Scale the modulating signal using the ratio given by (3.4) in order to deduce the per unit voltage fluctuation at the 132kV busbar of site A ($m'_a(t)$).

The above described process is illustrated by the block diagram of Figure 3.12. In a similar manner modulating signals of phases B and C ($m'_b(t), m'_c(t)$) can also be established.

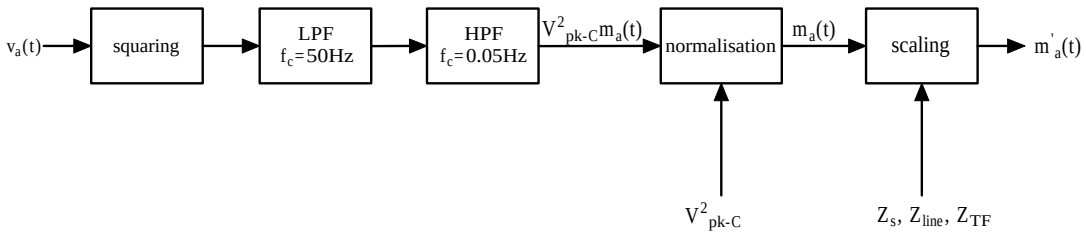

Figure 3.12: Process of reconstructing the voltage envelope (modulating signal) of the 132kV busbar at site A ($m'_a(t)$) using the waveform data captured at 22kV busbar at site C

As only the load classification of busbars E and F were available, assumptions had to be made in relation to the modelling of the respective loads.

Site E: Supplies mainly residential loads. Hence, the load was modelled as a lumped passive R-L load with a total rating of 22MVA at 0.99 power factor (lagging)

Site F: Supplies mainly industrial loads. It was assumed that the load consists of a combination of both passive and mains connected induction motor loads. The total induction motor load is equivalent to 28MVA at 0.998 power factor(lagging) while the rating of the passive load is 9MVA at 0.998 power factor (lagging).

3.3.3 Envelope Detection at Downstream

The solution time step (T_s) of the PSCAD/EMTDC model was selected, to be a value which is an integer multiple of the sampling time (=0.1μs) of the waveform data captured. Thus, T_s was chosen to be 0.1μs and the simulation run time was restricted to about 100-120 seconds, although measurements were performed over a period much longer than the total simulation time. With reference to the simplified radial network shown in Figure 3.11, the per unit variation in envelope of the line-to-neutral voltage at sites E and F are to be compared with the corresponding variations at site A.

Recovery of the modulating signals (voltage envelope) at sites E and F was carried out using a simple method. The rms voltmeters available in PSCAD/EMTDC followed by a gain constant were employed to extract variation in the amplitude, which can be considered as the modulating signal of the line-to-neutral voltage. The calculation method of rms voltage is based on a moving data window where the rms value of a buffered set of data is calculated at each time step. A sampling rate of 5000 data points per cycle, which is sufficient produce an output of the meter that does not contain fluctuations was used. Analysis of the frequency content of the voltage envelopes at upstream (site A) and downstream (sites E and F) will reveal the degree to which the upstream flicker is attenuated at downstream busbars. This process is

described in the following sections.

3.3.4 Propagation of Flicker from Site A to Sites E and F

The objective of this section is to examine the flicker propagation in the radial network of Figure 3.11, with the upstream 132kV busbar producing balanced voltage fluctuations. This is accomplished by modulating the three phase line-to-neutral voltages at site A using the modulating signal reconstructed as described in Section 3.3.2, with the necessary time shift applied to synthesise balanced operation.

Frequency spectra of the voltage envelope of the upstream (site A) and downstream (sites E and F) were established using Fast Fourier Transform (FFT) algorithm. Voltage waveforms over a window size of 50s were used for the spectral analysis. In order to ensure that the downstream loads and the filters used in envelope detection process reach steady state, simulation was first carried out over 120s before running over a continuous period of 50s for data capturing. A Hamming window of which time window characteristics are shown in Figure 3.13 was used to minimise the effects due to frequency leakages.

Figure 3.14 shows the variation of instantaneous flicker sensation (P_{it}) at upstream (site A) and downstream (sites E and F) established by the flickermeter used in Section 3.2. Reduction in P_{it} at site F is seen to be relatively significant compared to that of site E.

Figure 3.15 depicts the envelope of phase A line-to-neutral voltage and its frequency spectrum at site A where the maximum frequency value of the spectrum to be established is restricted to 35Hz, the upper limit of perceptible flicker frequency.

The following are evident from Figure 3.15:

- The content of the modulation frequency components in the envelope vary dramatically with time. The window length selected may significantly influence

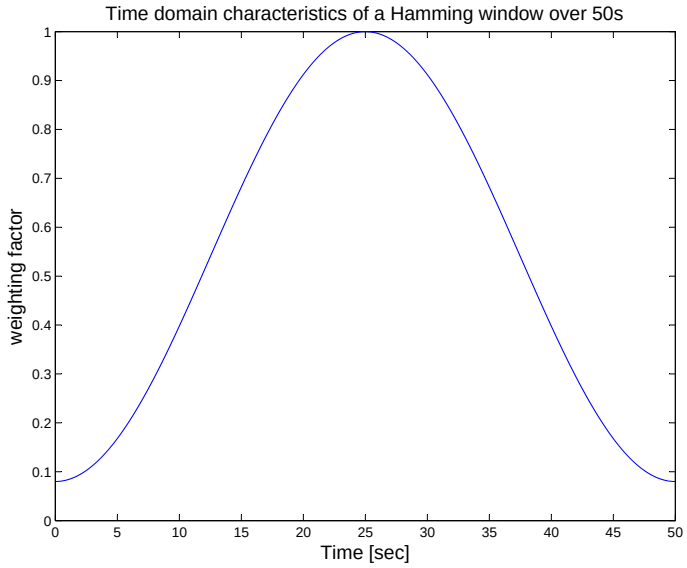

Figure 3.13: Time domain characteristics of a Hamming window

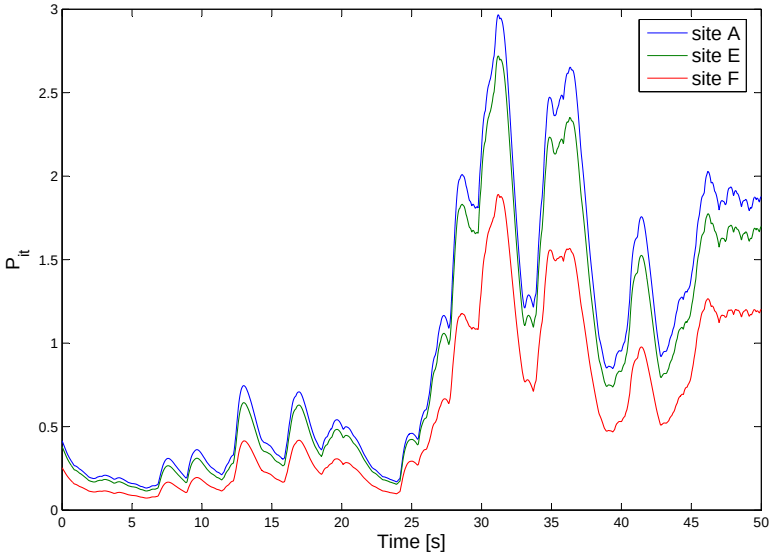

Figure 3.14: Variation of the instantaneous flicker sensation (P_{it})

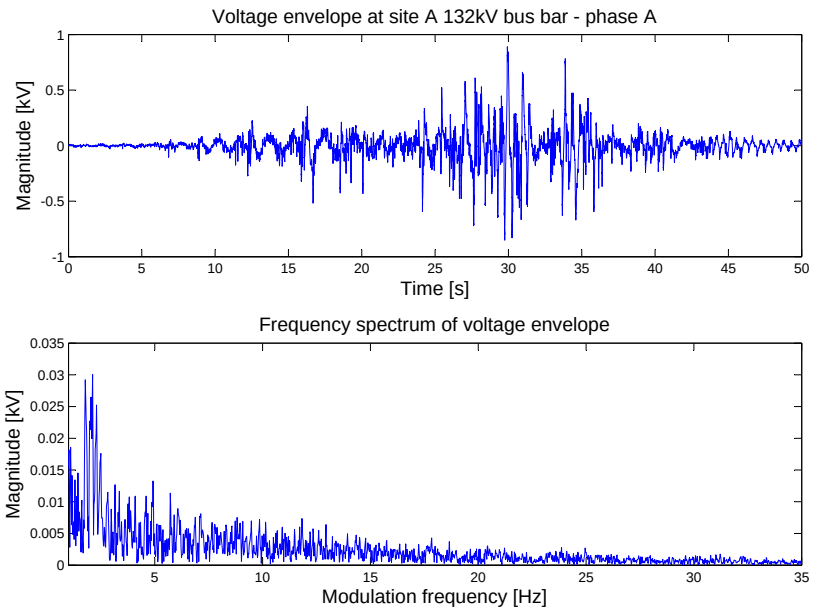

Figure 3.15: Voltage envelope and its frequency spectrum at site A

this.

- In relation to the perceptible flicker frequency range (0.05Hz-35Hz), magnitudes of the low modulation frequency components are significant compared to the magnitudes of relatively high modulation frequencies .

Figure 3.16 illustrates the spectra of the modulating envelopes of phase A line-to-neutral voltages at downstream sites E and F over a relatively narrow frequency range (between 8Hz and 12Hz). It is evident from Figure 3.16 that magnitude of each modulation frequency component at site F which is classified as industrial is slightly less than that of site E which is classified as residential. The discrepancy between the two spectra is not sufficient to distinguish the relative difference between level of attenuation of flicker at sites E and F with respect to site A. Hence, a hypothetical voltage transfer coefficient ($T_{\Delta v}$) is defined relating the magnitudes of the frequency content of the modulating signal (voltage envelope) at a downstream site (e.g. site E)

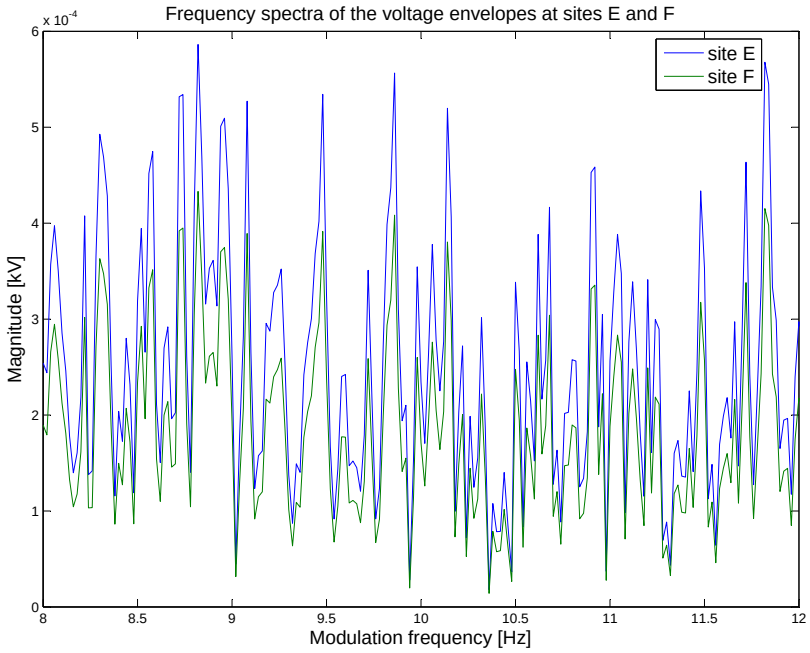

Figure 3.16: Frequency spectra of voltage envelopes at sites E and F

with the magnitudes of the frequency content of modulating signal at upstream (site A) for a fixed window length. For example, in relation to sites A and E, the ratio of the magnitudes of the spectral components in the modulating signal at sites E and A defines the hypothetical transfer coefficient ($T_{\Delta v}$) for the voltage fluctuations at site E with respect to site A. In a similar manner, sites A and F can be related to define $T_{\Delta v}$ which expresses the relative magnitude of voltage fluctuations at site F with respect to site A.

Figure 3.17 depicts the $T_{\Delta v}$ established at different modulation frequencies for sites E and F using a window length of 50s. The following conclusions can be drawn using the hypothetical voltage transfer coefficient ($T_{\Delta v}$) illustrated in Figure 3.17.

- A relatively constant value of $T_{\Delta v}$, which is approximately equal to unity, can be found at site E whereas some frequency dependency can be noticed in $T_{\Delta v}$ established for site F.

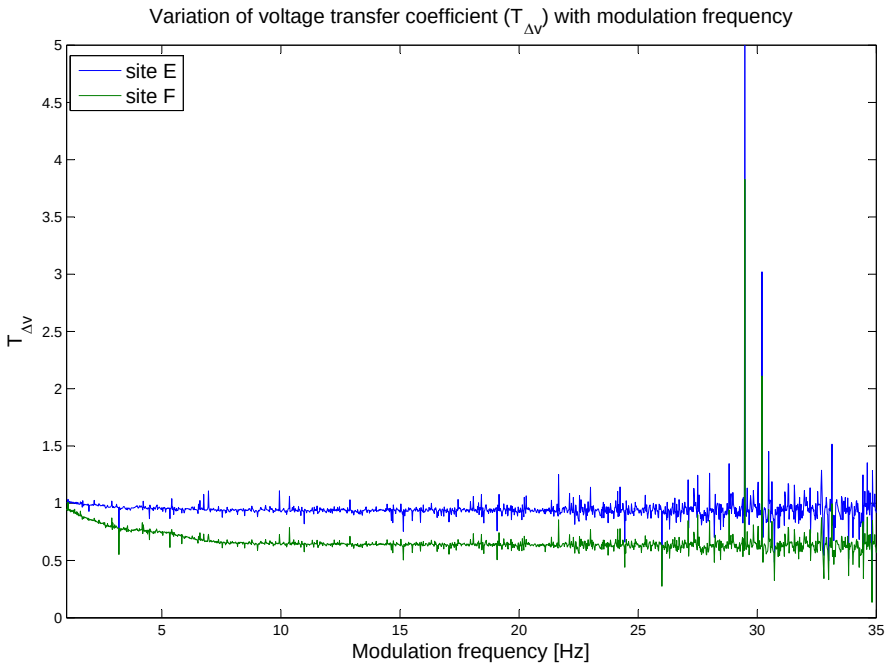

Figure 3.17: Variation of voltage transfer coefficient ($T_{\Delta v}$) with modulation frequencies that exist in voltage envelope

- The discrepancy between $T_{\Delta v}$ values established for the two sites suggests that site F, where the downstream consists of industrial loads, has some influence in attenuating voltage fluctuations compared to site E, where the loads are mainly passive residential.

- Abnormally high values of $T_{\Delta v}$ can be noticed as irregular variations. Such anomalies may have been caused by numerical problems due to extremely small magnitudes of modulation frequency components at upstream site A.

3.4 Summary

As the foundation to the main research objective, flicker propagation in radial networks was examined using time domain simulations under two scenarios.

Simulations were carried out in PSCAD/EMTDC by implementing a simple radial

network. Propagation of sinusoidal voltage fluctuations towards downstream was investigated under various downstream loading conditions.

It was clearly evident that motor loads assist in reducing the voltage fluctuations at downstream locations. The effects of the loading level and the proportion of the induction motor load have been examined. Flicker would be attenuated to a greater extent at higher loading levels and with large proportions of induction motor loads.

In simulations related to a simple radial system, a composite motor load was used where 40 identical individual machines are operating in parallel. However, in practice motor loads of various sizes, loading levels and load types are connected to the PCC hence comprehensive approaches are required to represent the aggregated motor loads at downstream. Furthermore, the characteristics of flicker transfer that have been observed in this chapter need theoretical explanations, especially the dependency of T_{Pst} on modulation frequency. Therefore, the results of this chapter will be referred to in latter chapters in deriving theoretical relationships between dynamics of the motor loads and flicker attenuation.

Propagation of flicker in a real system was examined by simulating the actual network using voltage waveforms captured. Simulation results suggest that upstream to downstream flicker propagation is influenced by the the downstream load classification. A hypothetical voltage transfer coefficient defined to distinguish the influence of different types downstream loads on flicker attenuation indicates that the industrial loads contribute to the process of reduction of voltage fluctuation at downstream.

Chapter 4

Response of Three Phase Induction Motors to Regular Voltage Fluctuations

4.1 Introduction

The rudimentary theory behind flicker propagation, the importance of flicker transfer coefficient and supporting measurement results were discussed in Chapter 2. Preliminary investigations on flicker in relation to radial networks covered in Chapter 3 suggest that attenuation of flicker is dependent on factors including the composition of loads at the various busbars. It is strongly evident that mains connected induction motors tend to help attenuate flicker better compared to passive loads.

One of the main objectives of the work covered in this thesis is to develop a sound theoretical knowledge on the stand-alone behaviour of three phase induction motors subject to regular fluctuations in the supply voltage. Some theory in relation to the three phase induction motor behaviour where they are tested by superimposing a low frequency component can be found in [27, 28], yet a detailed understanding on

the manner in which stator current responds in relation to the operating situation, an aspect which has a strong tie with the flicker attenuation provided by induction motors, is not the subject.

The work covered in this chapter is focused on investigating the dynamic response of induction motors that operate under fluctuating supply conditions. The mechanical and electrical responses of an induction motor is examined using small signal and large signal analysis. Small signal models are developed using state space analysis in order to establish theoretical arguments in relation to the response of the motors to regular fluctuations in the supply voltage. A conventional d-q domain large signal model is used to compare the accuracy of the small signal models. Several induction motors with different ratings are examined under two types of regular fluctuating conditions; (a) voltage fluctuations arising from superimposed positive or negative sequence frequency component, a flicker condition caused by frequency beating and (b) sinusoidal amplitude modulation of the fundamental frequency, a classical case considered in flicker studies. Major consequences of multiple rotating air gap mmf components are evaluated for the purpose of assessing the impact of frequency of voltage fluctuations on the stator current of induction motors.

4.2 Small Signal Modelling for Dynamic Performance Studies

4.2.1 Existing Applications

The dynamics of induction motors can be derived using fifth order motor models that are well established. Reduced order models which approximate the machine behaviour are widely used in dynamic performance studies such as transient and long term stability analysis [29, 30].

Small signal analysis of induction motors is commonly used in investigating power systems dynamics as well as in transient analysis of variable speed drives. Small signal models which relate active and reactive power changes arising from excursions in the system voltage are also used in stability studies [31]. Dynamic response of the electromagnetic torque and the rotor speed to low-frequency voltage perturbations have been investigated by Thiringer [32] for both motor and generator operation of an induction motor using low order transfer functions. In [33], stability and dynamic analysis of an open loop frequency controlled induction motor has been investigated by employing the root-locus criterion and transfer functions of the motor for multiple operating points. The basis of the work presented in this chapter is derived using the body of the work that already exists. However, novel formulations are required to be established to address the problem in hand.

4.2.2 Small Signal Modelling for Flicker Studies

Flicker caused by regular or irregular voltage fluctuations can be considered as transient state phenomenon. This suggests that dynamic behaviour of an induction motor that operates under fluctuating supply conditions can also be investigated by implementing appropriate modelling techniques that are based on small signal analysis. Hence small signal analysis of induction motors is used as the back bone of the work presented in this thesis. Most of the theoretical principles and arguments developed in regard to the operational characteristics of the motors and related issues such as attenuation of flicker are predominantly based on the small signal models.

The process involved in examination of the response of motors to voltage perturbations is accomplished by development of various transfer functions which relate the electrical and mechanical outputs to small voltage changes in the supply. State space analysis of induction motors is used to develop the transfer functions. Since the work

is focused on two types of voltage fluctuations as described in Section 4.1, the two methodologies involved are explained separately.

4.3 State Space Analysis of Induction Motors

4.3.1 Linearised Machine Equations

Development of small signal models has been carried out using state space analysis without neglecting the stator flux dynamics. Hence the proposed motor models are in the form of fifth order transfer functions. Compared to a conventional linearisation state space model, where the load torque is considered as an input to the system, the linearised motor model presented in this chapter combines the load torque dynamics with the electromechanical torque hence the input vector would be independent of load torque. The process of linearisation of voltage-flux and torque equations is described below.

For balanced operation of a three phase induction motor the voltage equations in the synchronously rotating reference frame are given by (4.1) [34] where the flux linkages per second are considered to be the state variables.

$$\begin{bmatrix} v_{qs} \\ v_{ds} \\ v'_{qr} \\ v'_{dr} \end{bmatrix} = \begin{bmatrix} \frac{r_s X'_{rr}}{D} + \frac{p}{\omega_b} & \frac{\omega_e}{\omega_b} & -\frac{r_s X_M}{D} & 0 \\ -\frac{\omega_e}{\omega_b} & \frac{r_s X'_{rr}}{D} + \frac{p}{\omega_b} & 0 & -\frac{r_s X_M}{D} \\ -\frac{r'_r X_M}{D} & 0 & \frac{r'_r X_{ss}}{D} + \frac{p}{\omega_b} & \frac{\omega_e - \omega_r}{\omega_b} \\ 0 & -\frac{r'_r X_M}{D} & -\frac{\omega_e - \omega_r}{\omega_b} & \frac{r'_r X_{ss}}{D} + \frac{p}{\omega_b} \end{bmatrix} \begin{bmatrix} \psi_{qs} \\ \psi_{ds} \\ \psi'_{qr} \\ \psi'_{dr} \end{bmatrix} \tag{4.1}$$

where,

$$X_{ss} = X_{ls} + X_M \tag{4.2}$$

$$X'_{rr} = X'_{lr} + X_M \tag{4.3}$$

$$D = X_{ss}X'_{rr} - X_M^2 \tag{4.4}$$

The machine variables in (4.1) are expressed as per unit quantities using the following base values.

V_{base} = Line to neutral peak voltage (V_p)
I_{base} = Peak line current (I_p)

The electromagnetic torque (T_e) and its relationship with the rotor angular speed (ω_r) are given by (4.5) and (4.6):

$$T_e = \frac{X_M}{D}(\psi'_{dr}\psi_{qs} - \psi'_{qr}\psi_{ds}) \tag{4.5}$$

$$T_e = 2Hp\frac{\omega_r}{\omega_b} + T_L \tag{4.6}$$

Equations (4.1), (4.5) and (4.6) can be linearised about an operating point to examine the small signal behaviour of the motor by applying Taylor series, following which the linearised voltage equations obtained are given by (4.7):

$$\begin{bmatrix} \Delta v_{qs} \\ \Delta v_{ds} \\ \Delta v'_{qr} \\ \Delta v'_{dr} \end{bmatrix} = \begin{bmatrix} \frac{r_s X'_{rr}}{D} + \frac{p}{\omega_b} & \frac{\omega_e}{\omega_b} & -\frac{r_s X_M}{D} & 0 & 0 \\ -\frac{\omega_e}{\omega_b} & \frac{r_s X'_{rr}}{D} + \frac{p}{\omega_b} & 0 & -\frac{r_s X_M}{D} & 0 \\ -\frac{r'_r X_M}{D} & 0 & \frac{r'_r X_{ss}}{D} + \frac{p}{\omega_b} & \frac{\omega_e - \omega_{ro}}{\omega_b} & \psi'_{dro} \\ 0 & -\frac{r'_r X_M}{D} & -\frac{\omega_e - \omega_{ro}}{\omega_b} & \frac{r'_r X_{ss}}{D} + \frac{p}{\omega_b} & \psi'_{dro} \end{bmatrix} \begin{bmatrix} \Delta\psi_{qs} \\ \Delta\psi_{ds} \\ \Delta\psi'_{qr} \\ \Delta\psi'_{dr} \\ \frac{\Delta\omega_r}{\omega_b} \end{bmatrix} \tag{4.7}$$

where,

$$\omega_e = \omega_b \tag{4.8}$$

$$s_o = \frac{\omega_e - \omega_{ro}}{\omega_e} \tag{4.9}$$

4.3.2 Incorporation of Load Dynamics

Using (4.5) and (4.6) the electromagnetic torque is obtained as follows:

$$T_L = \frac{X_M}{D}(\psi'_{dr}\psi_{qs} - \psi'_{qr}\psi_{ds}) - 2Hp\frac{\omega_r}{\omega_b} \tag{4.10}$$

Linearising (4.10),

$$\begin{aligned} \Delta T_L &= \frac{X_M}{D}(\psi'_{dro}\Delta\psi_{qs} - \psi'_{qro}\Delta\psi_{ds} - \psi_{dso}\Delta\psi'_{qr} + \\ &\quad \psi_{qso}\Delta\psi'_{dr}) - 2Hp\frac{\Delta\omega_r}{\omega_b} \end{aligned} \tag{4.11}$$

If the load torque-speed characteristics are known, (4.11) can be further modified. Here, a pump load with characteristics given by (4.12) is assumed.

$$(T_L)_{pu} = k\left(\frac{\omega_r}{\omega_b}\right)^2 \tag{4.12}$$

Linearising (4.12),

$$\Delta T_L = (\frac{2k\omega_{ro}}{\omega_b})\frac{\Delta\omega_r}{\omega_b} \tag{4.13}$$

Using (4.11) and (4.13), the dynamics of the motor and the pump load can be combined as:

$$\begin{aligned} &\frac{X_M}{D}(\psi'_{dro}\Delta\psi_{qs} - \psi'_{qro}\Delta\psi_{ds} - \psi_{dso}\Delta\psi'_{qr} + \psi_{qso}\Delta\psi'_{dr}) \\ &-(2Hp\frac{\Delta\omega_r}{\omega_b} + \frac{2k\omega_{ro}}{\omega_b}\frac{\Delta\omega_r}{\omega_b}) = 0 \end{aligned} \tag{4.14}$$

4.3.3 Combining the Machine Equations for State Space Representation

Linearised voltage equations and the torque-speed dynamic relationship given by (4.7) and (4.14) respectively can be expressed in state space form as given by (4.15).

$$px = Ax + Bu \tag{4.15}$$

where, the state vector,

$$x = \begin{bmatrix} \Delta\psi_{qs} & \Delta\psi_{ds} & \Delta\psi'_{qr} & \Delta\psi'_{dr} & \frac{\Delta\omega_r}{\omega_b} \end{bmatrix}^T \tag{4.16}$$

and control vector,

$$u = \begin{bmatrix} \Delta v_{qs} & \Delta v_{ds} & \Delta v'_{qr} & \Delta v'_{dr} \end{bmatrix}^T \tag{4.17}$$

in which $\Delta v'_{qr}$ and $\Delta v'_{dr}$ are both equal to zero (assuming a squirrel cage motor) and the system matrix $[A]$ and input matrix $[B]$ can be established as:

$$A = \begin{bmatrix} -\frac{r_s X'_{rr}}{D} & -1 & \frac{r_s X_M}{D} & 0 & 0 \\ 1 & -\frac{r_s X'_{rr}}{D} & 0 & \frac{r_s X_M}{D} & 0 \\ \frac{r'_r X_M}{D} & 0 & -\frac{r_r X_{ss}}{D} & -s_o & \psi'_{dro} \\ 0 & \frac{r'_r X_M}{D} & s_o & -\frac{r'_r X_{ss}}{D} & -\psi'_{qro} \\ \frac{X_M \psi'_{dro}}{2HD\omega_b} & -\frac{X_M \psi'_{qro}}{2HD\omega_b} & -\frac{X_M \psi_{dso}}{2HD\omega_b} & \frac{X_M \psi_{qso}}{2HD\omega_b} & -\frac{k\omega_{ro}}{2H\omega_b^2} \end{bmatrix} \tag{4.18}$$

$$B = \omega_b \begin{bmatrix} 1 & 0 & 0 & 0 \\ 0 & 1 & 0 & 0 \\ 0 & 0 & 1 & 0 \\ 0 & 0 & 0 & 1 \\ 0 & 0 & 0 & 0 \end{bmatrix} \tag{4.19}$$

.

Equation (4.15) along with the appropriate output vectors can be used to formulate various transfer functions that describe the dynamic response of the motor to small fluctuations in the supply voltage.

4.4 Supplementary Material used in Present Work

In order to compare the accuracy of the outputs of small signal models, a conventional d-q domain large signal induction motor model is implemented in MATLAB/Simulink environment [35, 36, 37]. Figure 4.1 illustrates the Simulink induction motor model. The major building blocks and the steps involved in formulating the model are given in Appendix A. As in the case of small signal models, the saturation and deep bar effect have not been taken into consideration in developing this large signal model.

In order to gain a broader understanding, four different induction machines with ratings ranging from 3hp to 2250hp with parameters as given in Table 4.1 [34], are considered in the theoretical work. Amongst these machines, the 2250hp machine has already been used in Chapter 3 in carrying out preliminary investigations.

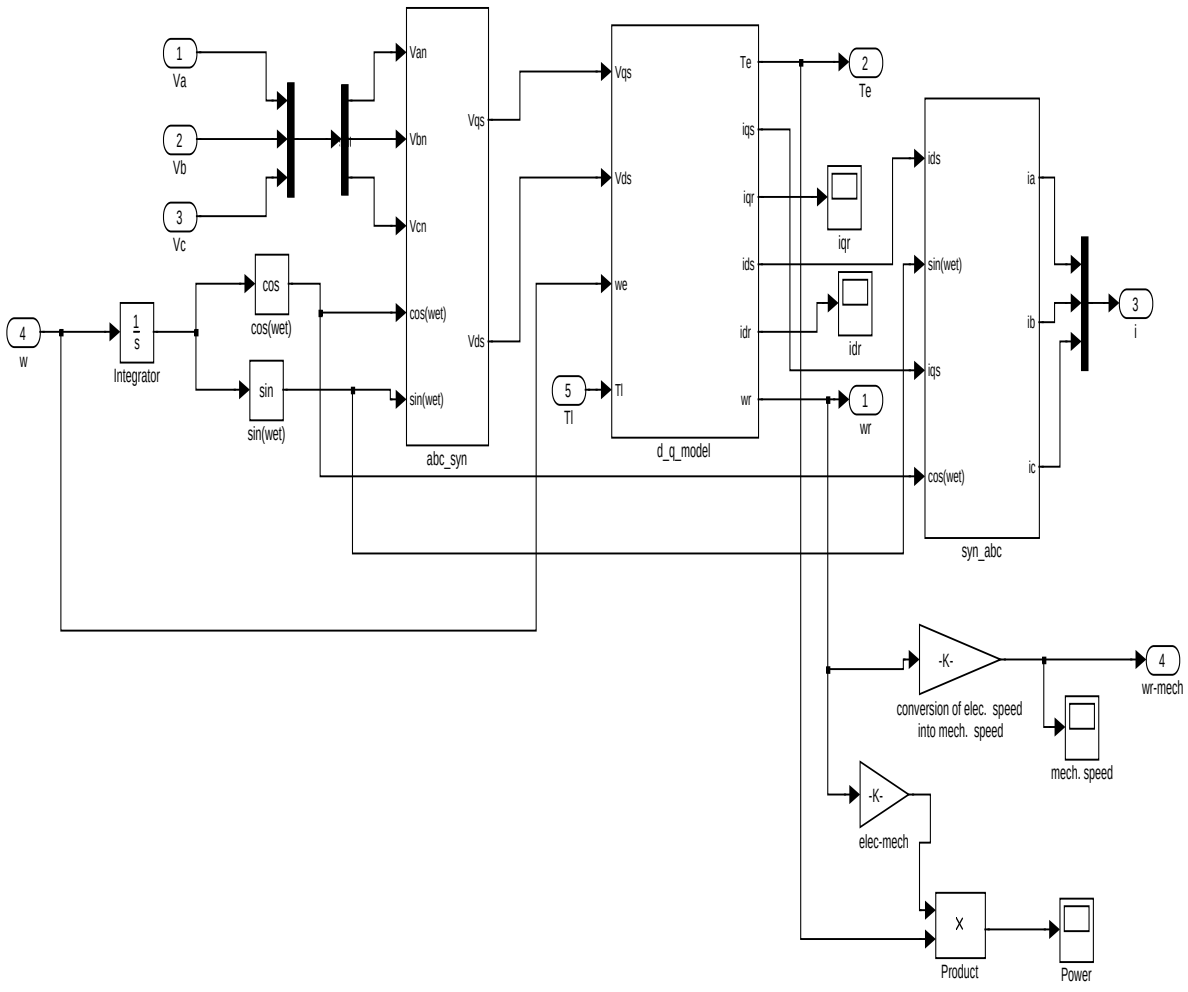

Figure 4.1: Simulink induction motor model

Table 4.1: 60Hz induction motor parameters

HP	Voltage (V)	rpm	$r_s(\Omega)$	$X_{ls}(\Omega)$	$X_M(\Omega)$	$X'_{lr}(\Omega)$	$r'_r(\Omega)$	$J(kgm^2)$
3	220	1,710	0.435	0.754	26.13	0.754	0.816	0.089
50	460	1,705	0.087	0.302	13.08	0.302	0.228	1.662
500	2,300	1,773	0.262	1.206	54.02	1.206	0.187	11.06
2,250	2,300	1,786	0.029	0.226	13.04	0.226	0.022	63.87

4.5 Type I Voltage Fluctuations: Superimposed Positive Sequence Frequency Component on the Mains Voltage Waveform

4.5.1 Identification of Voltage Perturbations

The motor response to voltage fluctuations arising due to the presence of two frequency components, mains frequency and the frequency of superimposed voltage perturbation, is investigated. Frequency f_i of the superimposed positive sequence voltage perturbation can be greater (super-synchronous) or smaller (sub-synchronous) than the mains frequency f_b (f_b =60Hz). It is necessary to establish a means of identifying the various voltage and current components, as the resultant stator current is influenced by the interference between various frequency components as discussed in latter stages of this chapter. In the present context the frequency components of currents that appear has a strong resemblance to sinusoidal amplitude modulation where the mains frequency voltage waveform is amplitude modulated at f_m, which leads to two side band frequency components $f_b - f_m$ and $f_b + f_m$. Thus, any single frequency component f_i superimposed that has a frequency

- less than f_b will be called lower side band with a voltage Δv_{LSB} satisfying the relationship $f_i = f_b - f_m$ where 40Hz $\leq f_m \leq$ 0.01Hz leading to 20Hz $\leq f_i \leq$ 59.99Hz.

- greater than f_b will be called upper side band with a voltage Δv_{USB} satisfying the relationship $f_i = f_b + f_m$ where 0.01Hz $\leq f_m \leq$ 40Hz leading to 60.01Hz $\leq f_i \leq$ 100Hz.

Further, relating to the case of sinusoidal amplitude modulation, each of the side bands will have a peak value $V_m/2$, where V_m is the peak value of the modulating wave.

Assuming the peak value of the mains voltage to be V_p, the three line-to-neutral voltages for a superimposed positive sequence frequency are given by:

$$v_{a,b,c} = V_p \sin(\omega_b t - (n-1)\frac{2\pi}{3}) + \frac{V_m}{2}\sin(\omega_i t - (n-1)\frac{2\pi}{3}) \qquad (4.20)$$

where $\omega_b = 2\pi f_b$, $\omega_i = 2\pi f_i$ and $n = 1, 2, 3$.

4.5.2 Small Signal Modelling of Rotor Speed Fluctuations

Due to the presence of two airgap magnetic fields, one due to the mains voltage and the other due to the superimposed voltage, both of the same phase sequence, the electromagnetic torque of the motor will pulsate at a difference frequency $|f_b - f_i|$ leading to a pulsation in the mechanical speed at the same difference frequency. This behaviour is commonly discussed in relation to inverter driven induction motors, an aspect which will have a significant influence on the machine behaviour in the present context. The relationship between the speed fluctuations and the voltage perturbations is modelled using a transfer function approach as explained below.

For a supply voltage consisting of a superimposed positive sequence sinusoidal frequency component, the three phase voltages given by (7.23) can be transformed to d-q frame to obtain Δv_{qs} and Δv_{ds}. These small signal excursions expressed as per

unit quantities are given by:

$$\Delta v_{qs} = \frac{V_m}{2V_p} \cos \omega_m t \tag{4.21}$$

$$\Delta v_{ds} = -\frac{V_m}{2V_p} \sin \omega_m t \tag{4.22}$$

Using (4.15) the state vector that contains rotor speed fluctuation can be established as:

$$x = (sI - A)^{-1} u \tag{4.23}$$

Using the matrix A and vector u, the steady state fluctuation in the speed as a normalised quantity can be shown to take the form as given by (4.24):

$$\frac{\Delta \omega_r}{\omega_b} = m_1 \cos \omega_m t + m_2 \sin \omega_m t \tag{4.24}$$

where m_1 and m_2 are constants which depend on the electrical and mechanical parameters of the motors. Equation (4.24), indicates that the frequency of speed fluctuations is ω_m.

4.5.3 Speed Fluctuations derived from Small and Large Signal Models

For the range of superimposed frequencies, that is 20Hz< f_i <100Hz, the magnitude of the rotor speed oscillations can be determined using (4.24). A large signal model is also used to examine the speed fluctuations and to maintain consistency. For the large signal simulations undertaken the amplitude of the superimposed voltage was maintained constant such that $V_m/2$ =0.025 V_p.

Figure 4.2 shows the variation of the peak value of the speed fluctuation ($\Delta \omega_r$) as a percentage of the steady state speed for the 2250hp motor with the nominal value of inertia given in [34] where very good agreement is seen between results from small

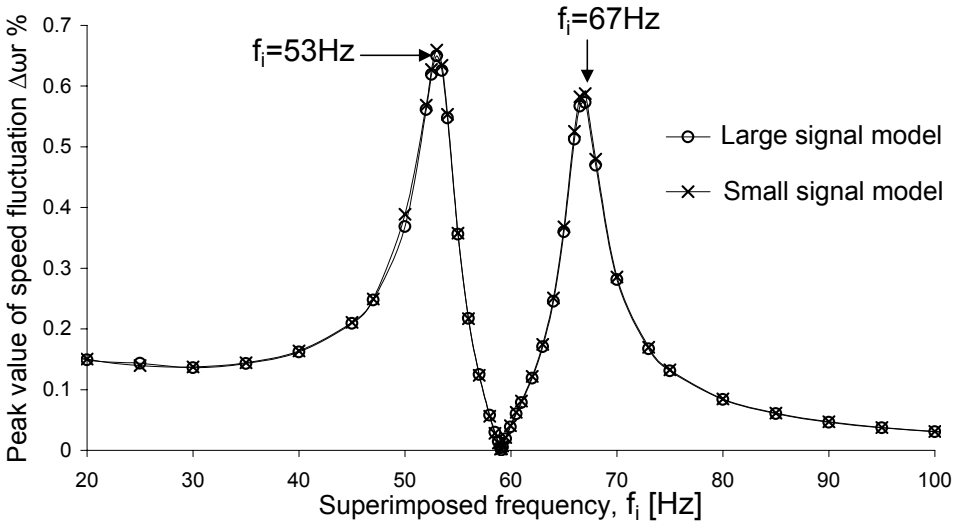

Figure 4.2: Rotor speed fluctuation of the 2250hp motor with superimposed frequency established using small and large signal analyses

signal and large signal approaches. Figure 4.3 shows the results from large signal analysis illustrating how the speed fluctuations are affected by the inertia, where a consistent increase in the magnitude of the speed fluctuation can be noted for smaller inertia values. Figure 4.4 illustrates the results from large signal analysis comparing the speed fluctuation exhibited by the four different motors, where a significant dependency of speed fluctuations on the size of the motor can be noted.

4.5.4 Generation of Additional emf Components on Stator

a. Interaction between the Speed Oscillations and the Stator Current

Although the amplitude of speed fluctuation is relatively small, it has a strong influence on the stator current over the frequency range of interest in relation to flicker. The manner in which the resulting stator current interacts with the rotor thus affecting the level of speed oscillation can be explained in terms of negative and positive damping as in the case of sub-synchronous resonance in power systems. Appendix B gives a qualitative discussion on this self perpetuating behaviour, employing the results that are presented in this section.

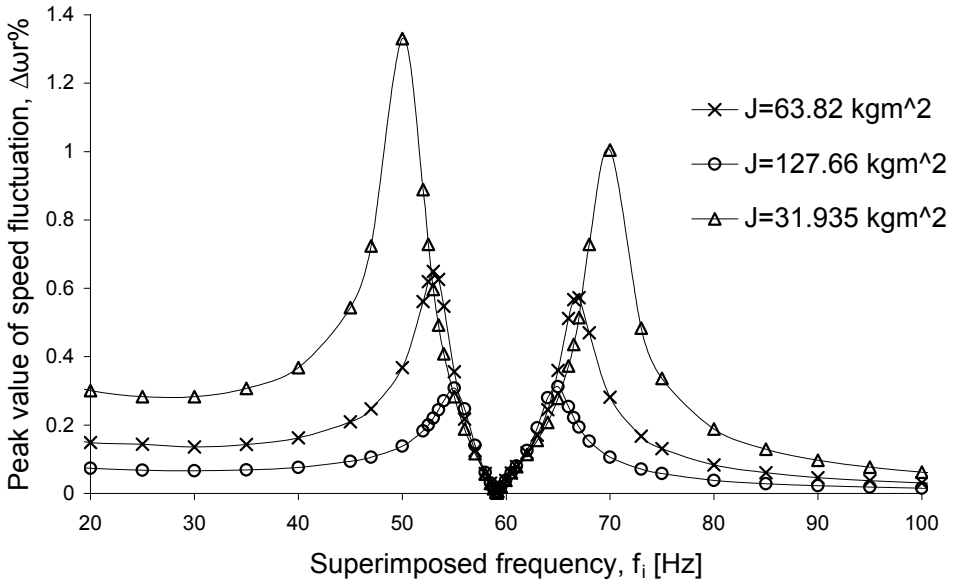

Figure 4.3: Variation of rotor speed fluctuations of the 2250hp motor with superimposed frequency for three different values of inertia

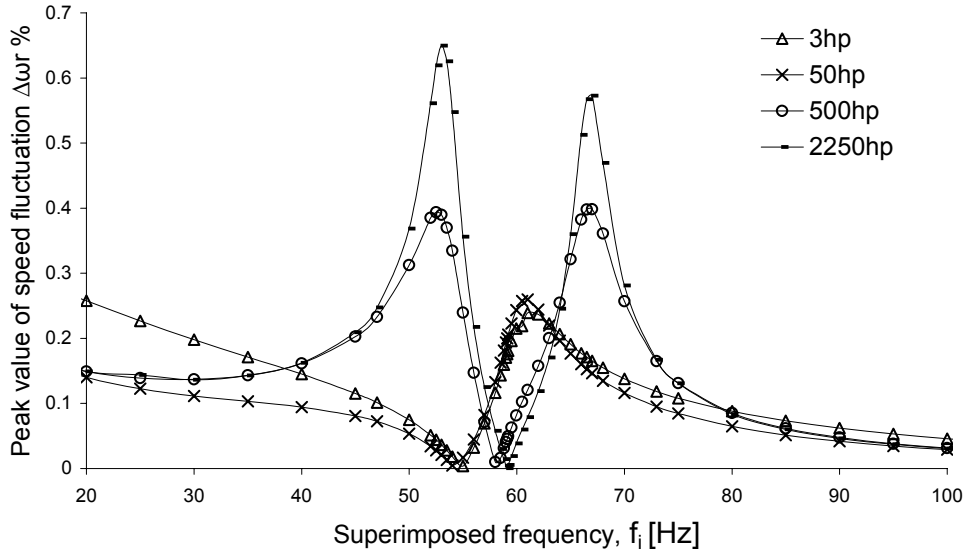

Figure 4.4: Variation of rotor speed fluctuation with superimposed frequency for four different motors with superimposed frequency

A primary consequence of speed fluctuations is generation of extra emf components in the rotor as well as in the stator. It has been noted that, the speed fluctuation caused by a superimposed positive sequence voltage perturbation on the stator tends to produce extra emf components in the rotor at frequencies that are different to the superimposed frequency, which in turn reflect back onto the stator (multiple armature reaction).

The theory of rotating electromagnetic fields due to stator frequency components and their interaction with the rotor, which is now oscillating at a difference frequency of $|f_b - f_i| = f_m$, can be used to establish the frequencies that are induced back in the stator. Appendix C describes the derivation of major frequency components that can be found in the stator in addition to the mains and superimposed frequency for a superimposed upper side band frequency.

It can be shown that if the superimposed frequency component is a lower side band (i.e. $f_i = f_b - f_m$), extra frequency components will be induced in the stator at $f_b + f_m$ and $f_b \pm 2jf_m$, where j is an integer (1, 2, 3, etc.). However, through the time domain simulations carried out it has been noted that amongst the corresponding extra side band currents, $f_b + f_m$ is the most significant component while $f_b \pm 2jf_m$ components have relatively negligible magnitudes for all superimposed frequencies and hence are ignored in further work. Similar analysis can be carried out when the superimposed frequency is an upper side band (i.e. $f_i = f_b + f_m$), where the extra frequency components will be induced at $f_b - f_m$ of most significant magnitude, and $f_b \pm 2jf_m$ with negligible magnitudes allowing them to be ignored. Hence, the only extra side bands considered for a superimposed lower and upper side band of this work are those at $f_b + f_m$ and $f_b - f_m$ respectively.

Table 4.2 gives the frequencies of the dominant emf components arising as a result of the multiple armature reaction process.

Table 4.2: Frequency components of emf components in rotor and stator caused by rotor speed oscillation at angular speed of $\omega_m = 2\pi f_m$ and a superimposed positive sequence frequency component $(2\omega_b + \omega_m)$; * extra side band frequencies

Stator applied frequency	Rotor frequency	Stator frequency
f_b (mains frequency)	$(f_b - f_m) - f_r$	$f_b - f_m$ *
	$f_b - f_i$	f_b
	$(f_b + f_m) - f_r$	$f_b + f_m$ *
$f_b + f_m$ (upper side band)	$f_b - f_r$	f_b
	$(f_b + f_m) - f_r$	$f_b + f_m$ *
	$(f_b + 2f_m) - f_r$	$f_b + 2f_m$
$f_b - f_m$ (lower side band)	$f_b - f_r$	f_b
	$(f_b - f_m) - f_r$	$f_b - f_m$ *
	$(f_b - 2f_m) - f_r$	$f_b - 2f_m$

b. Superimposition of Lower Side Band

Figure 4.5 shows the variation of the magnitudes of the two side band components (Δi_{LSB} and Δi_{USB}) of stator current for the 2250hp machine for lower side band injection. In addition to the lower side band current component at $f_i = f_b - f_m$, an extra upper side band component of stator current at a frequency of $(f_b + f_m)$ can be noted here. The magnitudes of the side band currents, to varying levels, are influenced by both (a) level of speed fluctuation which governs the corresponding induced voltage and (b) frequency of the side band current which influences the effective impedance for current flow. With reference to Figure 4.2, at a superimposed frequency of 53Hz the speed fluctuation exhibits a local maximum. The corresponding upper side band frequency is therefore 67Hz which lines up with the peak value of the upper side band current in Figure 4.5. As the injected frequency is further decreased below 53Hz the magnitude of speed fluctuations decrease and the frequency of the upper side band frequency increases and hence the extra side band current is seen to reduce. The current caused by the superimposed frequency f_i is seen to generally increase as its frequency is decreased, which suggest that this variation is relatively significantly affected by the frequency rather than the speed fluctuation that is now relatively low.

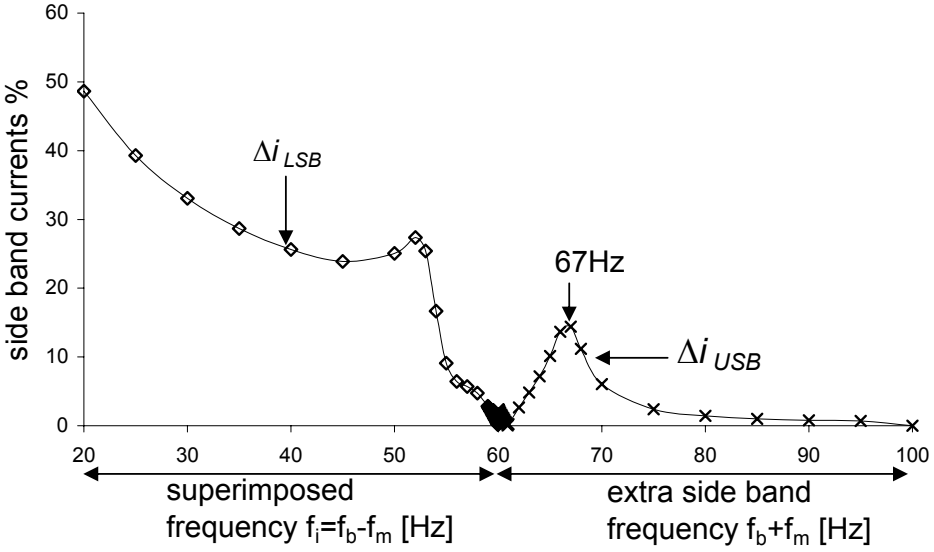

Figure 4.5: Variation of stator current side bands for a superimposed lower side band for 2250hp motor: $f_i = f_b - f_m$

c. Superimposition of Upper Side Band

Figure 4.6 shows the variation of the magnitudes of the two side band components (Δi_{LSB} and Δi_{USB}) of stator current for the 2250hp machine for a superimposed upper side band voltage perturbation ($f_i = f_b + f_m$). The extra side band can be seen at $f_b - f_m$. Referring to Figure 4.2 the speed fluctuation exhibits a local maxima at 67Hz which corresponds to an extra lower side band at 53Hz exhibiting a local maximum as seen in Figure 4.6. As the superimposed frequency is further increased the speed fluctuations decrease and hence the resulting lower side band current is seen to decrease. The current caused by the superimposed frequency is seen to exhibit a significant local maximum at 67Hz. It appears that this component of current is affected significantly by the speed fluctuation as well as frequency. Beyond 67Hz the current becomes increasingly governed by the increasing frequency of the superimposed voltage. Simulations quite clearly illustrate that the superposition principle

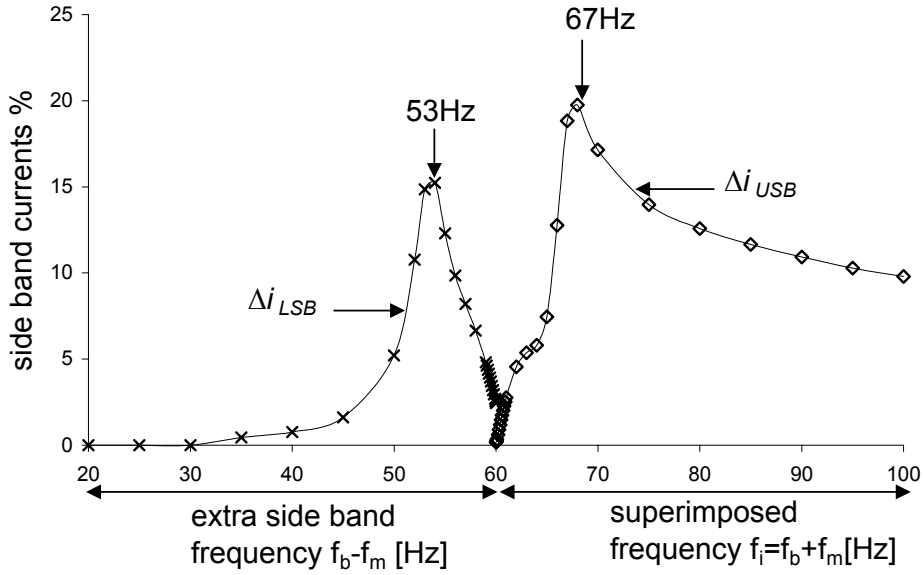

Figure 4.6: Variation of stator current side bands for upper side band injection, 2250hp motor: $f_i = f_b + f_m$

commonly used for the analysis of induction motors subjected to mains frequencies carrying superimposed frequencies becomes increasingly valid only at higher superimposed frequencies.

Comparing Figures 4.5 and 4.6, it can be noted that the total fluctuating current component (combination of the currents due to superimposed frequency and the extra side band) is seen to be relatively large when the superimposed frequency is low (i.e. 20Hz) when compared with that at high frequency end (i.e. 100Hz). Based on the above, as a preliminary observation, it can be stated that the rms voltage fluctuations arising as a result of the motor behaviour are very much dependent on the frequency of the voltage fluctuations.

d. Variation of Side Band Currents for Motors of Difference Ratings

Figures 4.7 and 4.8 illustrate the variation of side band currents for superimposed lower and upper side band frequencies respectively for the four different machines. It is clear that the two large machines behave differently to the two small machines.

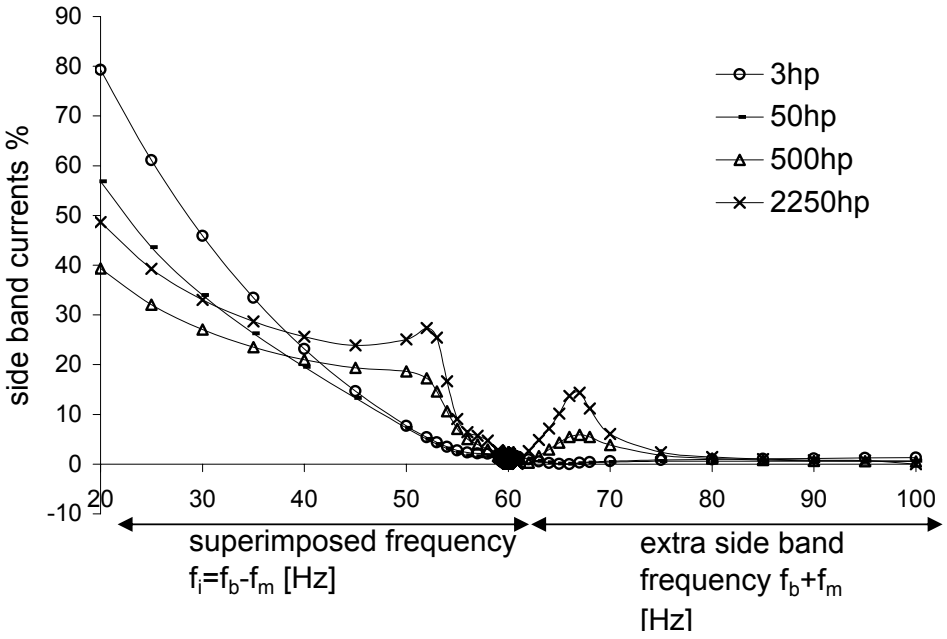

Figure 4.7: Comparison of stator current side bands of different motors for lower side band injection

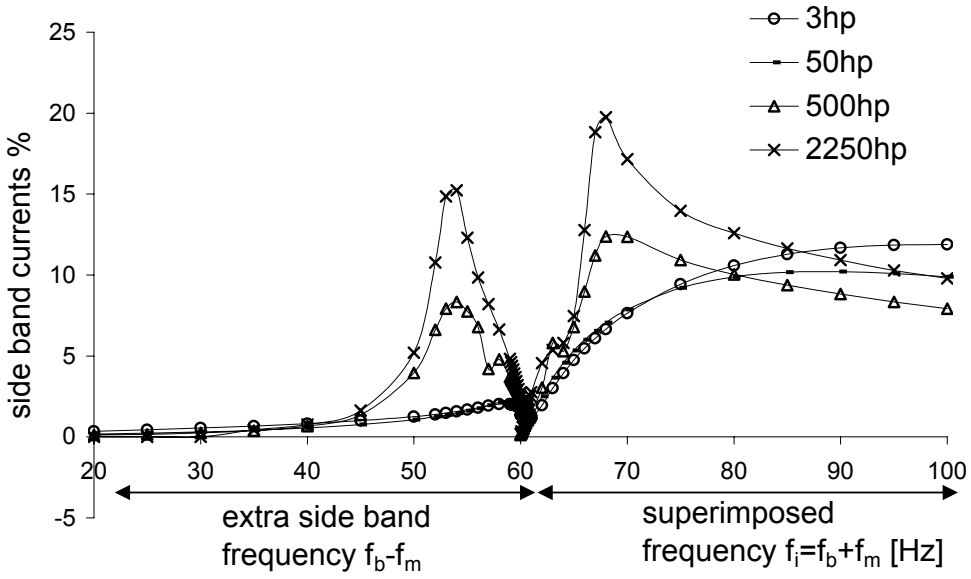

Figure 4.8: Comparison of stator current side bands of different motors for upper side band injection

For lower side band injection the large machines exhibit significant lower and upper side band currents over a wide frequency range, while the two small machines exhibit significant lower side band currents and not upper side band currents. For upper side band injection the two large machines exhibit significant upper and lower side band currents while the two small machines exhibit significant upper side band currents while the lower side band currents are seen to be relatively small.

e. Stator Current Response to Voltage Fluctuations caused by a Superimposed Negative Sequence Component

With negative sequence injection rotor speed fluctuation will take place at $f_b + f_i$. Simulations reveal that the corresponding level of speed fluctuation is relatively insignificant compared to that corresponding to positive sequence injection. The resulting additional components of current induced in the stator are at higher frequencies that are outside the normal flicker frequency range of interest. Also, these high frequency current components are of negligible magnitude and hence would be of little relevance in relation to voltage fluctuations and flicker.

4.6 Type II Voltage Fluctuations: Sinusoidal Amplitude Modulation of Mains Voltage

4.6.1 Rotor Speed Oscillations: Large Signal Behaviour

Assuming balanced sinusoidal amplitude modulation, the line-to-neutral voltages applied to a three phase motor can be defined as

$$v_{a,b,c} = V_p[1 + m\sin(2\pi f_m t)]\cos(2\pi f_b t - (n-1)\frac{2\pi}{3}) \tag{4.25}$$

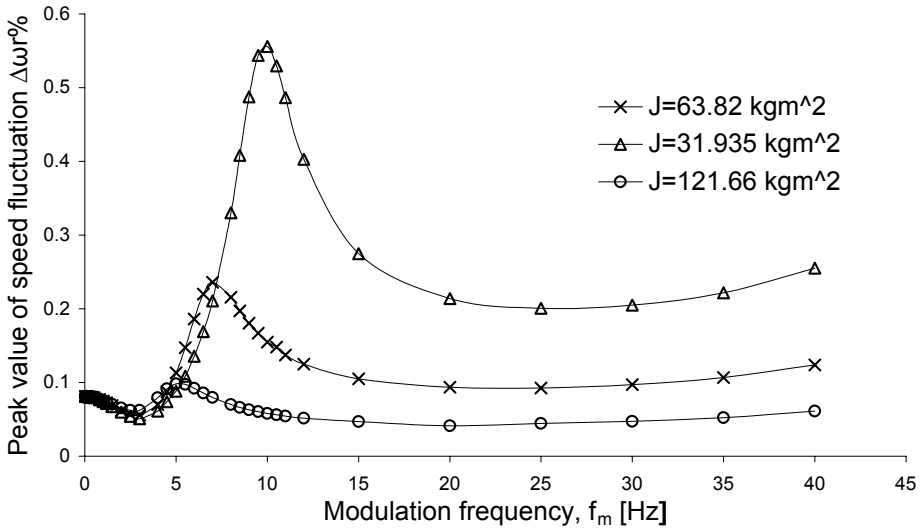

Figure 4.9: Rotor speed fluctuation of the 2250hp motor for amplitude modulation

where n =1, 2, 3 and $m = \frac{V_m}{V_p}$ - modulation depth

In the simulations carried out the modulating waveform was selected such that $V_m = 0.05\ V_p$ and hence the magnitude of each of the resultant side band voltages is equal to the magnitude of the superimposed voltage in single frequency analysis discussed in Section 4.5. Similar to the operation of the machines under a supply with a superimposed positive sequence single frequency component, the machines exhibited speed fluctuations at f_m. For the 2250hp machine these speed fluctuations are illustrated in Figure 4.9 demonstrating their dependency on inertia as well.

As expected stator current exhibits component currents at $f_b - f_m$ and $f_b + f_m$ although of different magnitudes as illustrated by Figure 4.10. Relatively negligible side band currents at frequencies of $f_b \pm 2jf_m$ where j is an integer (1, 2, 3, etc.) were noticed which will be neglected in further analytical work. Figure 4.10 also shows the magnitudes of the current corresponding to a superimposed single frequency component as discussed in Sections 4.5.4(b) and 4.5.4(c) and shown in Figures 4.5 and 4.6. The differences in the current levels clearly indicate that in the case of amplitude modulation the resultant side band current is due to the net effect of

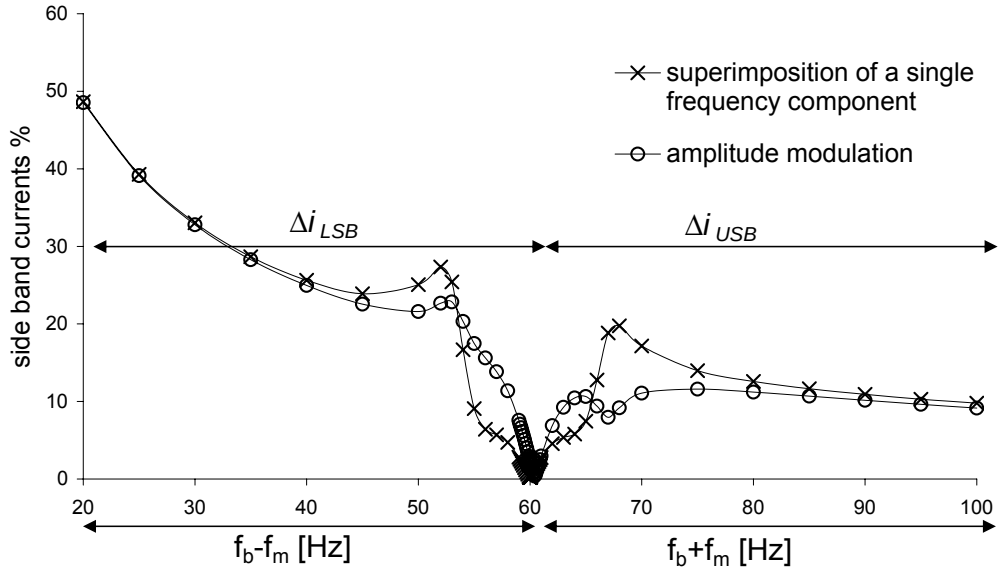

Figure 4.10: Variation of stator side band current components (as a percentage of the fundamental) with side band frequency ($f_b - f_m$ or $f_b + f_m$) established for amplitude modulation and superimposition of a single frequency component

multiple armature reaction and they cannot be obtained by simply considering the side band current which arises due to the single frequency injection. For example, the side band current magnitude corresponding to a frequency of 40Hz (which is caused by a modulating frequency of f_m=20Hz) is caused by the armature reaction due to a current side band at a frequency of 80Hz as well.

4.6.2 Modelling the Response of the Stator Current using Small Signal Analysis

In contrast to single frequency analysis where an additional voltage component is superimposed on the mains voltage, in sinusoidal amplitude modulation it is the amplitude of the mains voltage which fluctuates sinusoidally. Thus, a transfer function of the form

$$G(s) = \frac{\Delta i_s}{\Delta v_s} \tag{4.26}$$

where,

Δv_s - small signal change in the amplitude of the supply voltage

Δi_s - resultant change in the stator current

can be developed to examine how the induction motors respond to voltage perturbations caused by amplitude modulation. The major steps involved in establishing the transfer function are explained as below.

For a balanced set of sinusoidal supply voltages the d-q axes voltages are of the form

$$\begin{bmatrix} v_{qs} \\ v_{ds} \end{bmatrix} = \begin{bmatrix} V_p \\ 0 \end{bmatrix} \tag{4.27}$$

Thus, for a small perturbation (Δv_s) in the supply voltage magnitude,

$$\begin{bmatrix} \Delta v_{qs} \\ \Delta v_{ds} \end{bmatrix} = \begin{bmatrix} \Delta v_s \\ 0 \end{bmatrix} \tag{4.28}$$

Using (4.17) and (4.28):

$$u = G\Delta v_s \tag{4.29}$$

where,

$$G = \begin{bmatrix} 1 & 0 & 0 & 0 \end{bmatrix}^T \tag{4.30}$$

Δv_s is defined as a sinusoidal signal as per (4.31) in order to represent a typical modulating signal at a frequency f_m.

$$\Delta v_s = \frac{V_m}{V_p} \sin \omega_m t \tag{4.31}$$

The small signal stator currents (output vector -y) are related to the state vector as

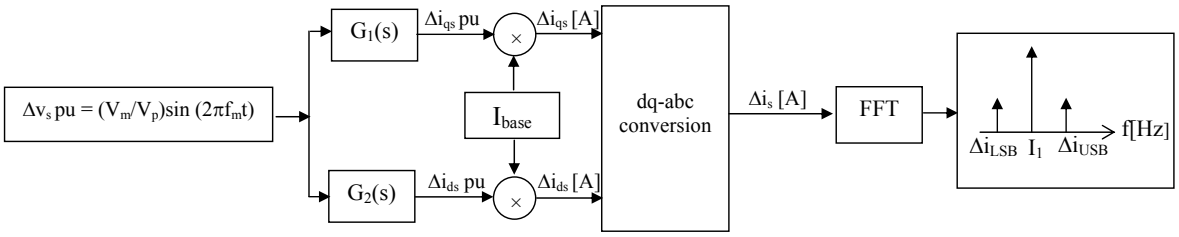

Figure 4.11: Recovery of stator current perturbation (Δi_s)

per (4.32)

$$y = Cx \tag{4.32}$$

where,

$$y = \begin{bmatrix} \Delta i_{qs} & \Delta i_{ds} \end{bmatrix}^T \tag{4.33}$$

$$C = \frac{1}{D} \begin{bmatrix} X'_{rr} & 0 & -X_M & 0 & 0 \\ 0 & X'_{rr} & 0 & -X_M & 0 \end{bmatrix} \tag{4.34}$$

Modifying the control vector (4.17) to incorporate stator voltage perturbations given by (4.28) and solving the state space equations (4.15) and (4.32), two fifth order transfer functions ($G_1(s)$ and $G_2(s)$) can be established as

$$\begin{bmatrix} \frac{\Delta i_{qs}}{\Delta v_s} \\ \frac{\Delta i_{ds}}{\Delta v_s} \end{bmatrix} = \begin{bmatrix} G_1(s) \\ G_2(s) \end{bmatrix} \tag{4.35}$$

Δi_{qs} and Δi_{ds} need to be transformed to the phase domain to establish the stator current variations as functions of the perturbation in the supply voltage. These perturbations will yield the side bands of the stator current Δi_{LSB} and Δi_{USB} when Fourier analysed. The above process is illustrated by the block diagram of Figure 4.11.

Appendix D gives the derivation of $G_1(s)$ and $G_2(s)$ for the 2250hp machine. Comparison of side band current magnitudes obtained by employing small signal analysis and those obtained from large signal analysis, illustrated in Figure 4.12 clearly demonstrate the suitability of the small signal models for the prediction of the perturbations

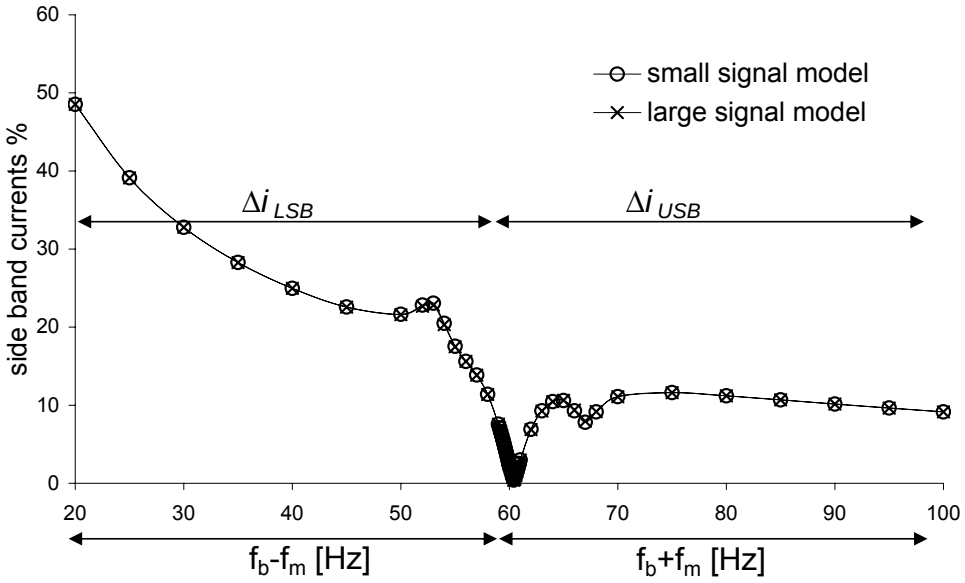

Figure 4.12: Variation of stator side band current components (as a percentage of the fundamental) established using small and large signal analyses for amplitude modulation

in the stator current.

Figure 4.13 shows the stator stator current responses of the four different machines considered. As in the case of single frequency injection, the four machines can be categorised into two groups based on the stator response, as large machines (2250hp and 500hp) and small machines (50hp and 3hp) which exhibit distinctly different behaviours. This suggests that depending on machine sizes and their parameters, different induction machines can lead to different flicker attenuation characteristics.

4.7 Summary

The main objective of this chapter was to examine the stand alone behaviour of induction motors subject to regular fluctuations in the supply.

Linearised motor equations were first used to model the oscillations in the rotor speed arising from a superimposed positive sequence voltage. Large signal behaviour is used to verify the speed oscillations established using small signal analysis and

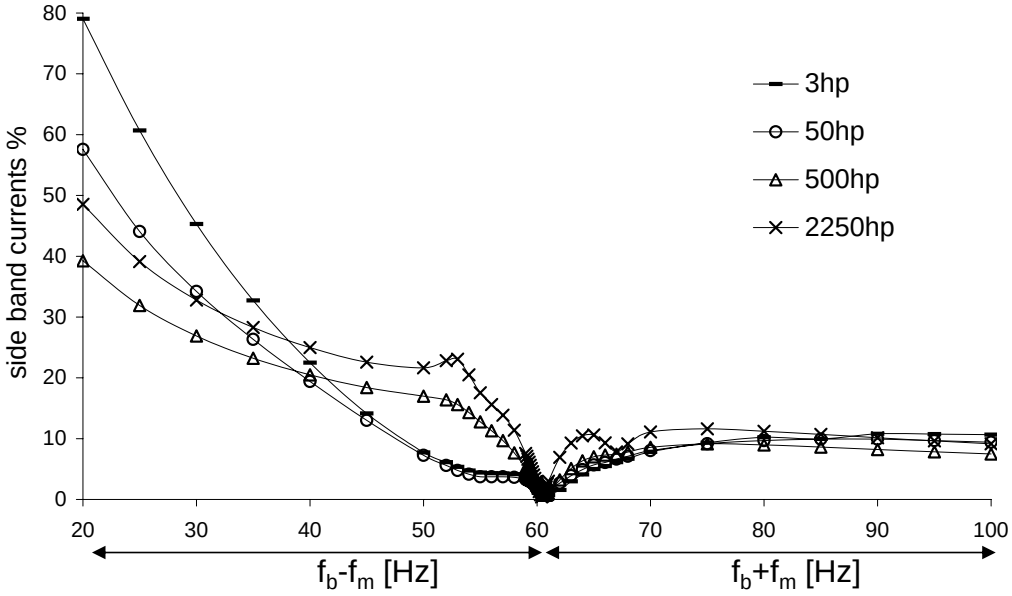

Figure 4.13: Comparison of the side band currents caused by amplitude modulation for motors of different sizes

to establish the stator current response which would again be used to compare with small signal models . Analysis of models reveal that the interaction between the speed oscillations and the stator current response gives rise to generation of additional air gap mmf components. This multiple armature reaction produces emf components of frequencies that are different to the superimposed frequency in the rotor, which would reflect back on to the stator. Additional frequency components that appear as the major side bands in the stator current can make a significant impact on the net rms current drawn by the motor at certain superimposed frequencies. Results suggest that the response of a three phase induction machine cannot be accurately predicted using the commonly accepted superposition principle, especially when the superimposed frequency is close to the mains frequency or when it takes a subharmonic value.

The response of the stator current to voltage fluctuations caused by sinusoidal amplitude modulation has been modelled using a transfer function approach. The major side bands in the current are related to the mains frequency and the sinu-

soidal modulating frequency. Again, the main components of significance have been identified.

For the two types of fluctuating supply conditions that are considered, the resultant side band currents have been noted to be dependent on the superimposed frequency or the modulating frequency. This suggests that the influence of the motor in relation to attenuation of flicker would be governed by the stator current response, which is now found to be appreciably frequency dependent. A significant dependency of the stator current magnitude on size (rating) of the motor has also been identified. The models developed will be extended in Chapter 5 to examine the flicker attenuation in radial networks.

Chapter 5

Analysis of Flicker Transfer in Radial Systems

5.1 Introduction

Response of induction motors of different ratings to two types of regular fluctuations in the supply voltage was investigated in Chapter 4. Small signal and large signal models were used to establish the mechanical and the electrical responses of motor loads to voltage fluctuations arising from superimposed voltage perturbations of small magnitudes.

The work presented in this chapter is an extension of the modelling of induction motors in relation to flicker. The main objective is to develop a rational theoretical basis which can be implemented in order to investigate the contribution made by mains connected induction motor loads to attenuate flicker which propagates from an upstream location of a radial network to a downstream location where induction motors are installed.

The initial small signal induction motor model which relates a small change in the supply voltage to the resultant change in the stator current is extended to include

a radial network where the network represents the impedance between the upstream fluctuating source and the downstream load. This approach allows development of a systematic method to analyse the magnitude and phase relationships between the voltage fluctuations at the source and load ends in the radial network. The method developed is used to investigate the propagation of voltage fluctuations of distinct frequencies from upstream to downstream where an induction motor load is connected. Propagation of individual side bands is utilised to establish the net reduction in the modulating envelope of the supply. Influence of the other contributing factors to flicker attenuation such as system impedance and rating of the induction motor load are also investigated. The suitability of small signal modelling for flicker transfer studies is evaluated by examining the error involved in determining the flicker transfer coefficient using small signal approach. Error involved in the small signal model approach is evaluated by comparing the results of small and large signal models.

5.2 Small Signal Modelling of a Radial Network for Flicker Transfer Analysis

5.2.1 Description of the Network Model

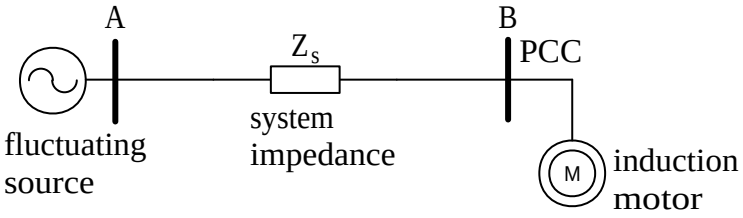

Figure 5.1: Radial system

In the analytical work covered in this chapter, a radial network that consists of two voltage levels as illustrated in Figure. 5.1 is used. Upstream (A) can be considered as

the PCC of a typical system. Flicker that exists in the upstream (A) is represented by a fluctuating voltage source. The downstream (B) consists of a composite load of an induction motor load and a passive load. Z_s represents the system impedance that connects the upstream and the downstream such as transformer impedance. A methodology is proposed to quantify the contribution of the downstream induction motors to the transfer of flicker from A to B.

Although in Chapter 4, the response of induction motors to two types of regular voltage fluctuations has been investigated, in the work presented in this chapter, emphasis is given only to flicker arising from sinusoidal amplitude modulation of mains frequency as it allows examination of the characteristics of flicker attenuation, such as its dependency on flicker frequency, in a more tangible manner.

5.2.2 Modification to the Small Signal Model of an Induction Motor to accommodate the Radial Network

In Chapter 4 the stator current response of an induction motor to sinusoidal voltage variations in the supply was modelled using two fifth order transfer functions ($G_1(s)$ and $G_2(s)$) which can be represented as per (5.1) and (5.2), where Δv_s is a small variation in the amplitude of the supply voltage, and Δi_{qs} and Δi_{ds} are the resultant variations in d-q axes stator currents. The process of transformation of the outputs of (5.1) and (5.2) from d-q domain to a-b-c (phase) domain in order to reconstruct the resultant change in phase domain stator current (Δi_s) is illustrated by Figure 5.2.

$$G_1(s) = \frac{\Delta i_{qs}}{\Delta v_s} \tag{5.1}$$

$$G_2(s) = \frac{\Delta i_{ds}}{\Delta v_s} \tag{5.2}$$

In Chapter 4, although the inputs to $G_1(s)$ and $G_2(s)$ were considered to be

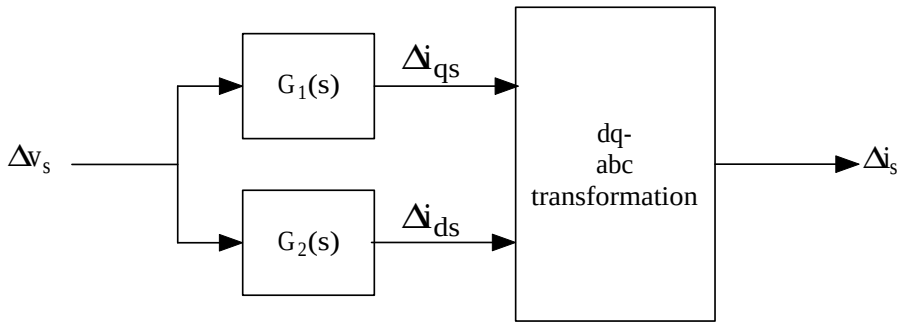

Figure 5.2: Block diagram of the small signal model which represents the process of recovering the stator current perturbation

sinusoidal signals, they can be of any regular or random signal implying that the model is capable of accommodating any type of flicker condition.

The above approach can be extended to a radial system shown in Figure 5.1 by incorporating the system impedance, Z_s ($Z_s = R_s + jX_s$) into the stator resistance (r_s, now known as r_{s-new}) and stator leakage reactance (X_{ls}, now known as X_{ls-new}) of the induction motor as per (5.3).

$$r_{s-new} + jX_{ls-new} = [r_s + R_s] + j[X_{ls} + X_s] \tag{5.3}$$

With this modification, outputs of $G_1(s)$ and $G_2(s)$ of Figure 5.2 are the changes in the d-q axes stator currents caused by a small change in the amplitude of the upstream (A) voltage when the induction motor is connected to the downstream (B). The established stator current response can be used to determine the instantaneous change in the voltage at B as:

$$\Delta v_B(t) = \Delta v_A(t) - L_s \frac{d}{dt}\Delta i_s(t) - R_s \Delta i_s(t) \tag{5.4}$$

where $\Delta v_A(t)$ and $\Delta v_B(t)$ are the instantaneous voltage changes at A and B respectively, $L_s = \frac{X_s}{2\pi f_b}$, and f_b being the mains or base frequency.

Similar to the investigations in Chapter 4, a sinusoidal signal is used as Δv_s in order to represent a typical sinusoidal amplitude modulating signal of frequency f_m. The frequency of Δv_s is varied between 0.01Hz and 40Hz, covering the perceptible flicker frequency range. The magnitude of Δv_s was maintained at 0.05pu which corresponds to a constant magnitude in voltage fluctuation (Δv) of 0.1pu ($\Delta v = 2 \times \Delta v_s$). Δv_s will give rise to two voltage side bands (perturbations) at two distinct frequencies at A ($\Delta v_A(t)$) and B ($\Delta v_B(t)$) as:

$$\Delta v_A(t) = \Delta v_{ALSB}(t) + \Delta v_{AUSB}(t) \tag{5.5}$$

$$\Delta v_B(t) = \Delta v_{BLSB}(t) + \Delta v_{BUSB}(t) \tag{5.6}$$

where $\Delta v_{ALSB}(t)$ and $\Delta v_{BLSB}(t)$ are the lower side bands at frequency $f_b - f_m$, and $\Delta v_{AUSB}(t)$ and $\Delta v_{BUSB}(t)$ are the upper side bands at frequency $f_b + f_m$. Accordingly, two transfer coefficients can be defined for the two voltage side bands as:

$$T_{LSB} = \frac{\frac{|\Delta v_{BLSB}|}{|v_B|}}{\frac{|\Delta v_{ALSB}|}{|v_A|}} \tag{5.7}$$

$$T_{USB} = \frac{\frac{|\Delta v_{BUSB}|}{|v_B|}}{\frac{|\Delta v_{AUSB}|}{|v_A|}} \tag{5.8}$$

where v_A and v_B are the steady state voltages at A and B respectively, as obtained from a load flow study.

5.3 Implementation of the Small Signal Model

5.3.1 Transfer Coefficients for a Network having a 2250hp Induction Motor at Downstream

For a radial network having a purely inductive system impedance ($Z_s = jX_s$) of 3% (of Z_{FL}, the base impedance of the motor at full load slip), the side band transfer coefficients (T_{LSB} and T_{USB}) are established. Figure 5.3 illustrates the variation of T_{LSB} and T_{USB} with the modulation frequency (f_m) established using both small signal and large signal models over the range of modulation frequencies stated earlier, where good agreement can be noted.

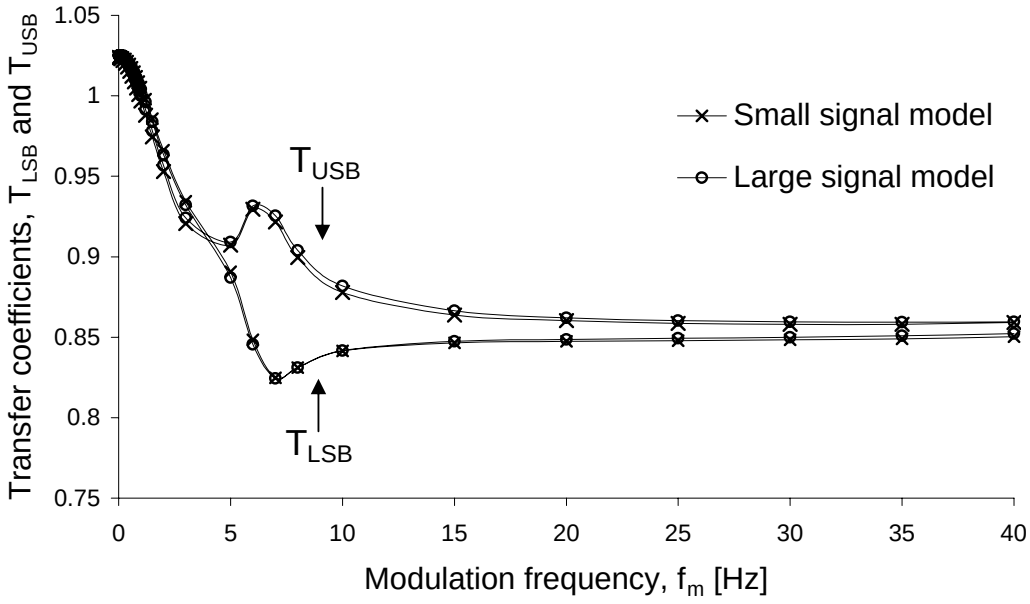

Figure 5.3: Variation of transfer coefficients of voltage side bands (T_{LSB} and T_{USB}) with modulation frequency (f_m) for the 2250hp motor

Over a wide range of modulation frequencies, the lower and upper side bands exhibit different attenuation levels where lower side band is seen to attenuate to a better extent compared to the upper side band for modulation frequencies above 5Hz. A close examination of Figure 5.3 at low f_m ($\leq$1Hz) values reveals that the side bands

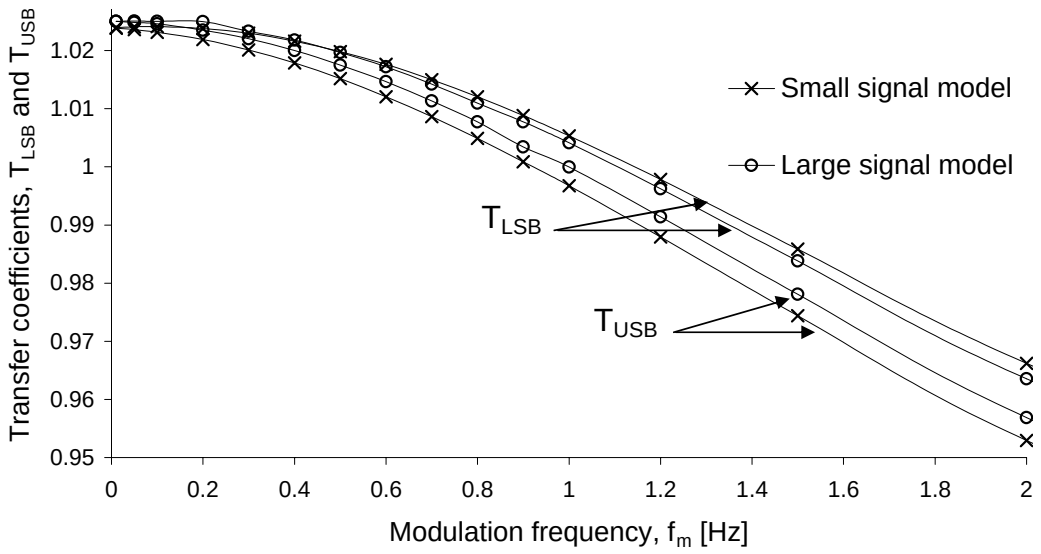

Figure 5.4: Variation of transfer coefficients of voltage side bands (T_{LSB} and T_{USB}) at low modulation frequencies for the 2250hp motor

do not attenuate but instead are magnified as illustrated by Figure 5.4.

Noting that the two side bands are caused by a single modulation frequency (f_m), the transfer coefficient of each voltage side band can be plotted against the frequency of the side band ($f_b \pm f_m$) as illustrated in Figure 5.5. As the maximum value of f_m used is 40Hz, transfer coefficients can be established for side band frequencies in the range 20Hz (=60Hz-40Hz) and 100Hz (=60Hz+40Hz).

5.3.2 Determination of Effective Sub-Synchronous and Super-Synchronous Impedances, Active and Reactive Power Variations

In order to derive qualitative explanations on the attenuation levels exhibited by the side bands as depicted in Figure 5.5 this section establishes the variation of the effective impedances and the corresponding real and reactive power flows with the side band frequency.

Considering the network of Figure 5.1 the transfer coefficient T in relation to

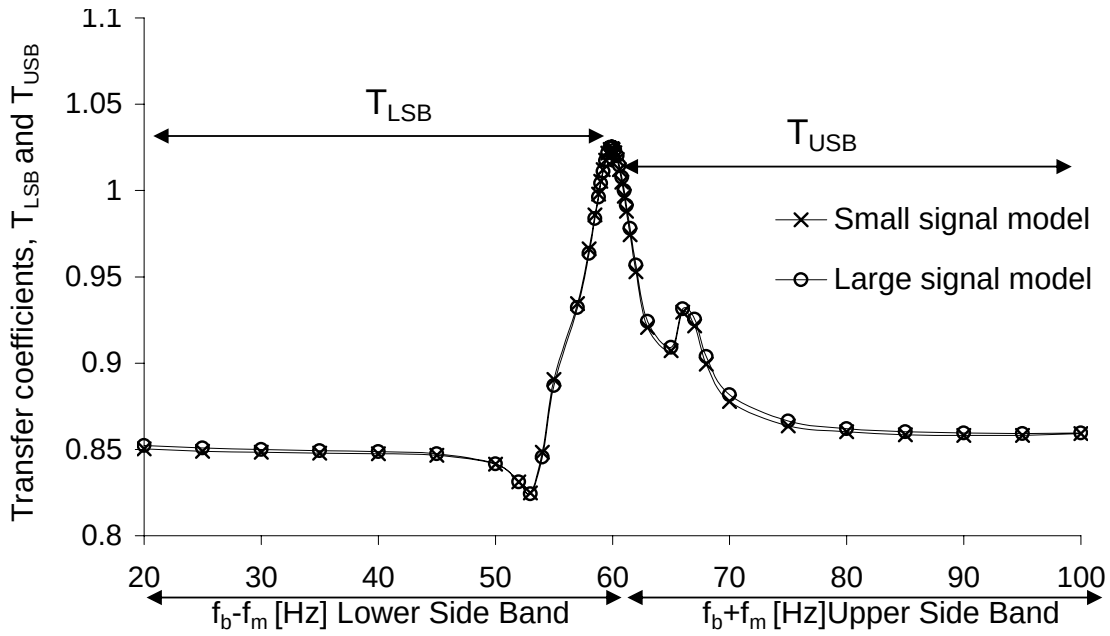

Figure 5.5: Variation of transfer coefficients of voltage side bands (T_{LSB} and T_{USB}) with side band frequency ($f_b \pm f_m$) for the 2250hp motor

voltage fluctuations can be expressed as:

$$T = \frac{\frac{|\Delta v_B|}{|v_B|}}{\frac{|\Delta v_A|}{|v_A|}} = \frac{|1 + \frac{Z_s}{Z_{motor}}|}{|1 + \frac{Z_s}{Z'_{motor}}|} \tag{5.9}$$

where $\Delta v_A, \Delta v_B$ are the voltage perturbations at A and B respectively, Z_{motor} is the steady state impedance of the motor and Z'_{motor} is the effective impedance offered by the motor to the voltage perturbation. In (5.9), for the case of sinusoidal amplitude modulation, Z'_{motor} could be considered as an effective sub-synchronous impedance for the lower side band and an effective super-synchronous impedance for the upper side band. Further, the magnitude and the angle (ψ) of the effective impedance of the motor are key factors that determine the extent to which each side band is attenuated at B compared to that present at A, as Z_s represents a static component.

Based on (5.9) it can be noted that if Z'_{motor} is inductive ($0^\circ < \psi < 90^\circ$ or $90^\circ < \psi < 180^\circ$), the smaller the magnitude of Z'_{motor} the better would be the

attenuation of the corresponding voltage side band at B. However, if Z'_{motor} becomes capacitive ($-90^\circ < \psi < 0^\circ$ or $-180^\circ < \psi < -90^\circ$), regardless of the magnitude of Z'_{motor}, the voltage side band will be magnified at B. Hence the nature of variation of Z'_{motor} which can be determined using the small signal analysis has to be examined.

The stator current response of the 2250hp motor operating with an amplitude modulated supply is used to determine its effective impedance (Z'_{motor}) for each side band as:

$$Z'_{motor} = \frac{|\Delta v_B|}{|\Delta i|}\angle\alpha_1 - \alpha_2 = |Z'_{motor}|\angle\psi \tag{5.10}$$

where Δi is the stator current perturbation (Δi_{LSB} or Δi_{USB}), and α_1 and α_2 are the phase angles of Δv_B and Δi respectively. Figures 5.6(a) and 5.6(b) illustrate the variation of $|Z'_{motor}|$ and ψ as a function of the frequency of voltage side bands ($f_b \pm f_m$). For the purpose of comparison it can be noted that over the frequency range of interest the magnitude of the impedance and its phase angle of a passive load that is equivalent to the 2250hp induction motor (of which the locked rotor impedance is 0.15pu) will be nearly constant in comparison to the variations exhibited by the induction motor.

At the side band frequencies the corresponding active and reactive power drawn by the motor can be established using conventional method as described by in the $\Delta P - \Delta Q$ plane of Figure 5.7.

$$\Delta P + j\Delta Q = \Delta v_B \times \Delta i^* \tag{5.11}$$

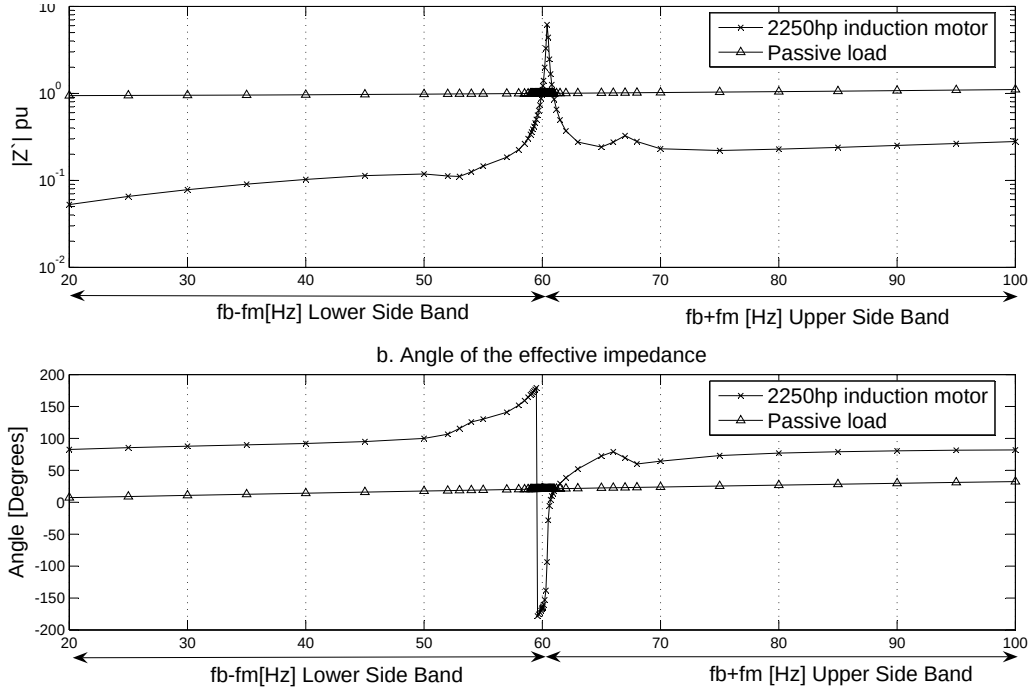

Figure 5.6: Variation of (a) the magnitude and (b) angle of the effective impedance of the 2250hp motor and an equivalent passive load with frequency of the voltage side band ($f_b \pm f_m$)

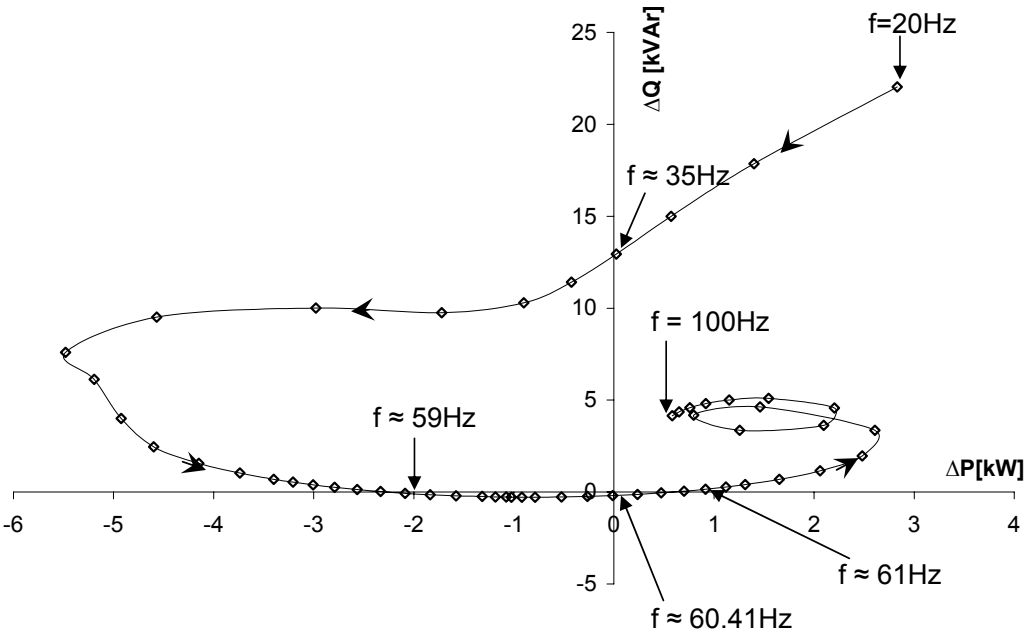

Figure 5.7: Active (ΔP) and reactive (ΔQ) power consumed by the 2250hp motor for voltage side bands at f, where $f = f_b \pm f_m$

5.3.3 Discussion on the Attenuation Levels exhibited by the 2250hp Motor

Lower Side Band (LSB); 20Hz $\leq f <$ 60Hz

Based on Figure 5.6, for voltage side bands at frequencies between 20Hz and 59Hz, the magnitude of the effective impedance of the motor is smaller than 1pu. The angle ψ varies between 83° and 90° for 20Hz $\leq f \leq$ 35Hz. It varies between 90° and 180° for 35Hz $\leq f \leq$ 59Hz and implies a negative resistance and an inductive reactance. This behaviour is further supported by the ΔP and ΔQ variations illustrated by Figure 5.7.

Over the side band frequency range 20Hz $\leq f \leq$ 59Hz, although the motor exhibits both positive and negative damping, it offers an inductive reactance as a part of the effective impedance that is less than unity in magnitude and hence the side bands will

attenuate at B. This behaviour is illustrated by the T_{LSB} curves in Figure 5.3 where the modulation frequency f_m is greater than approximately 1Hz and in Figure 5.5 where frequency of the voltage perturbation f is between 20Hz and 59Hz.

For voltage side bands at frequencies just below the fundamental frequency (i.e. 59Hz $\leq f <$ 60Hz), $|Z'_{motor}|$ is less than $<$ 1pu, yet the angle of Z'_{motor} is negative ($-180\,^\circ < \phi < -90\,^\circ$) exhibiting a negative resistance and a capacitive reactance, a behaviour that is supported by Figure 5.7 where both ΔP and ΔQ are negative. Regardless of the relatively small magnitude of Z'_{motor}, the capacitive reactance or the over excited nature of the motor would lead to magnification of the corresponding frequency components at downstream (B) for 59Hz $\leq f <$ 60Hz. This behaviour is illustrated by T_{LSB} curves in Figure 5.4.

Upper Side Band (USB); 60Hz $< f \leq$100Hz

For voltage side bands at frequencies just above the fundamental frequency (60Hz $< f \leq$ 61Hz), $|Z'_{motor}|$ is relatively large compared to the steady state impedance and its angle ψ varies between $-90\,^\circ$ and $0\,^\circ$. This is further evident from Figure 5.7 where ΔP is positive and and ΔQ is negative. Relatively large magnitude of $|Z'_{motor}|$ and the over excited behaviour causes the magnification of the corresponding frequency components at B.

As evident from Figure 5.6 in the frequency range 61Hz $\leq f \leq$ 100Hz, $|Z'_{motor}|$ varies between 0.2pu and 0.3pu and ψ varies between $0\,^\circ$ and $82\,^\circ$ indicating its inductive behaviour. This is further supported by positive ΔP and positive ΔQ in Figure 5.7. The positive damping provided by the motor leads to attenuation of the corresponding frequency components as illustrated by T_{USB} curves in Figure 5.3.

Difference between T_{USB} and T_{LSB} over the modulation frequency (f_m) range 5 - 10Hz

According to Figure 5.3, T_{LSB} and T_{USB} exhibit values less than unity for most of the modulation frequencies resulting from the relatively small magnitudes of Z'_{motor} as illustrated in Figure 5.6. However, a local minimum and maximum can be seen in Z'_{motor} over the two frequency ranges 50Hz-55Hz and 65Hz-70Hz respectively, leading to a local minimum and maximum in the voltage transfer coefficient. This effect is reflected on the transfer coefficients T_{LSB} and T_{USB} where a significant difference over the modulation frequency range 5-10Hz is seen.

5.3.4 Dependency of Transfer Coefficient on the Induction Motor Rating

Transfer coefficients of the voltage side bands evaluated for 3hp and 500hp motors [34] are illustrated in Figure 5.8 along with those of the 2250hp motor. As in the study in relation to the 2250hp motor, a totally inductive system impedance (Z_s) of 3% (of Z_{FL}, the base impedance of the motor at full load slip) is used. It is seen that 500hp and 2250hp motors exhibit similar attenuation characteristics. However, the 2250hp motor attenuates both side bands to a better extent compared to the 500hp motor. The 3hp motor is seen to demonstrate somewhat different variations in the side band attenuation levels.

5.3.5 Dependency of Transfer Coefficient on System Impedance

The system impedance Z_s was so far assumed to be purely inductive and its magnitude was assumed to be 3% of the motor at full load slip. In this section the influence of the magnitude of system impedance and its angle on side band attenuation is

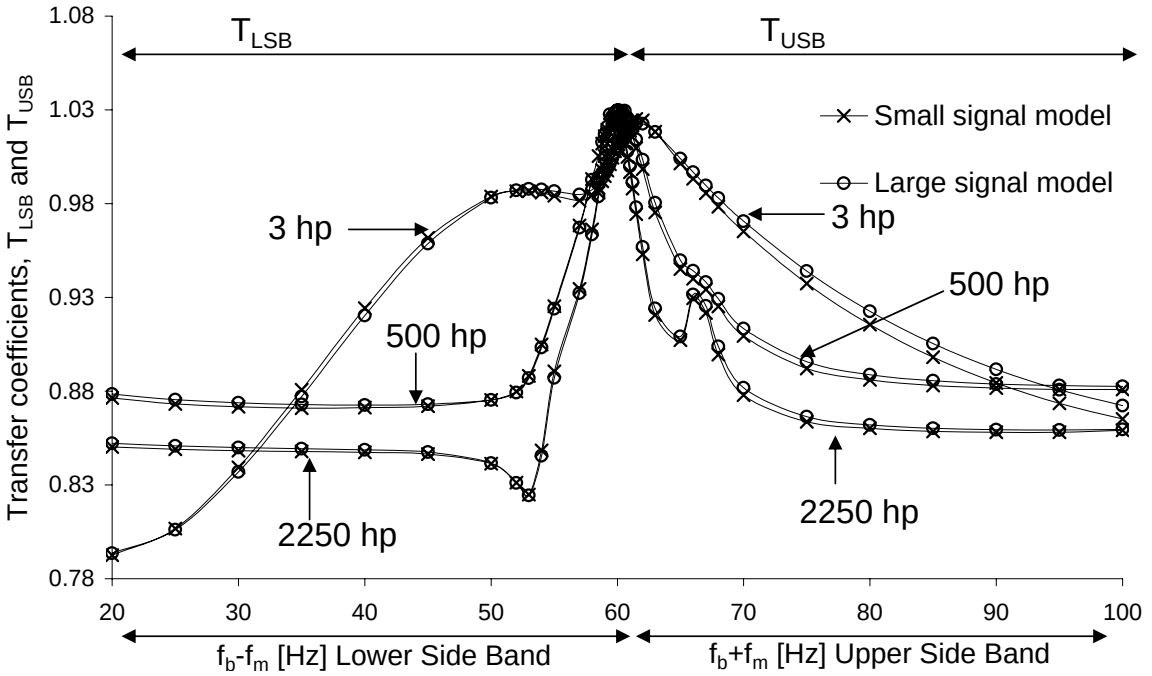

Figure 5.8: Variation of transfer coefficients of voltage side bands (T_{LSB} and T_{USB}) with side band frequency ($f_b \pm f_m$) for the three motors

investigated.

Dependency of Transfer Coefficients of Side Bands on the Magnitude of the Inductive System Impedance ($|Z_s|$)

Figure 5.9 shows the variation of the transfer coefficients of the voltage side bands with frequency of the side bands for the 2250hp motor for 3 different values of system impedance. As the magnitude of the system impedance is increased, attenuation levels can be seen to increase over a wide range of the side band frequencies. This behaviour can be justified using (5.9). Figure 5.10 illustrates the variation of T_{LSB} and T_{USB} for modulation frequencies in the vicinity of the fundamental frequency. As previously discussed, side bands tend to magnify at these low frequencies but the level of magnification is seen to decrease for smaller system impedance magnitudes as expected.

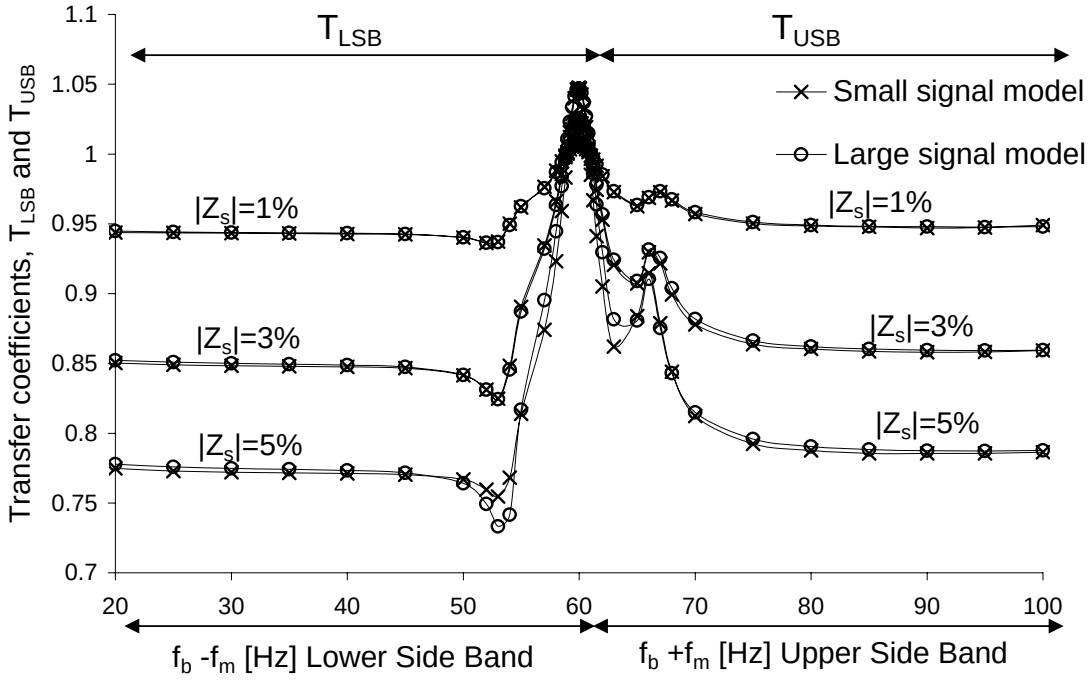

Figure 5.9: Variation of transfer coefficients of voltage side bands (T_{LSB} and T_{USB}) with side band frequency ($f_b \pm f_m$) for three system impedance ($Z_s = jX_s$) magnitudes - 2250hp motor

Dependency of the Transfer Coefficient of the Side Bands on System Impedance Angle (ψ_s)

In the previous results presented the system impedance was assumed to be purely inductive. The influence of the system impedance angle on flicker attenuation is critical to supply systems with high X/R ratios. In the results presented in this section system impedance is assumed to be of form $R + jX$.

Figure 5.11 illustrates the variation of the transfer coefficients of the side bands for the 2250hp motor for $\psi_s = 90°$ and $\psi_s = 60°$ while maintaining the magnitude of Z_s constant. It seems reasonable to assume that the attenuation levels depend on the impedance angle where increasingly inductive system impedances favour better attenuation.

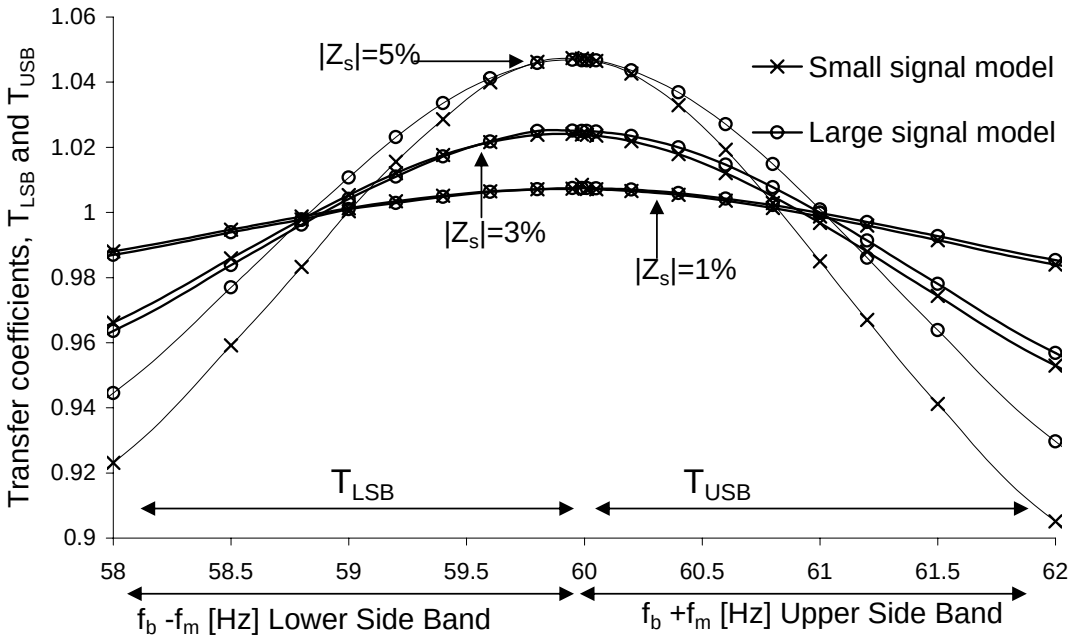

Figure 5.10: Variation of transfer coefficients of voltage side bands (T_{LSB} and T_{USB}) with side band frequency ($f_b \pm f_m$) for three line ($Z_s = jX_s$) impedance magnitudes at for low modulation frequencies values - 2250hp motor

5.4 Correlation between the Attenuation of Side Bands and Flicker Attenuation

5.4.1 Determination of flicker transfer coefficient using the small signal model

The manner in which the voltage side bands of a sinusoidally modulated voltage propagating from upstream to the downstream was presented in the previous sections. However, these studies cannot be expected to provide a complete insight into flicker transfer as the latter is characterised on the fluctuations in voltage envelope rather than on individual voltage side bands. This section compares side band attenuation levels with the actual flicker present at A and B in the network of Figure 5.1. For

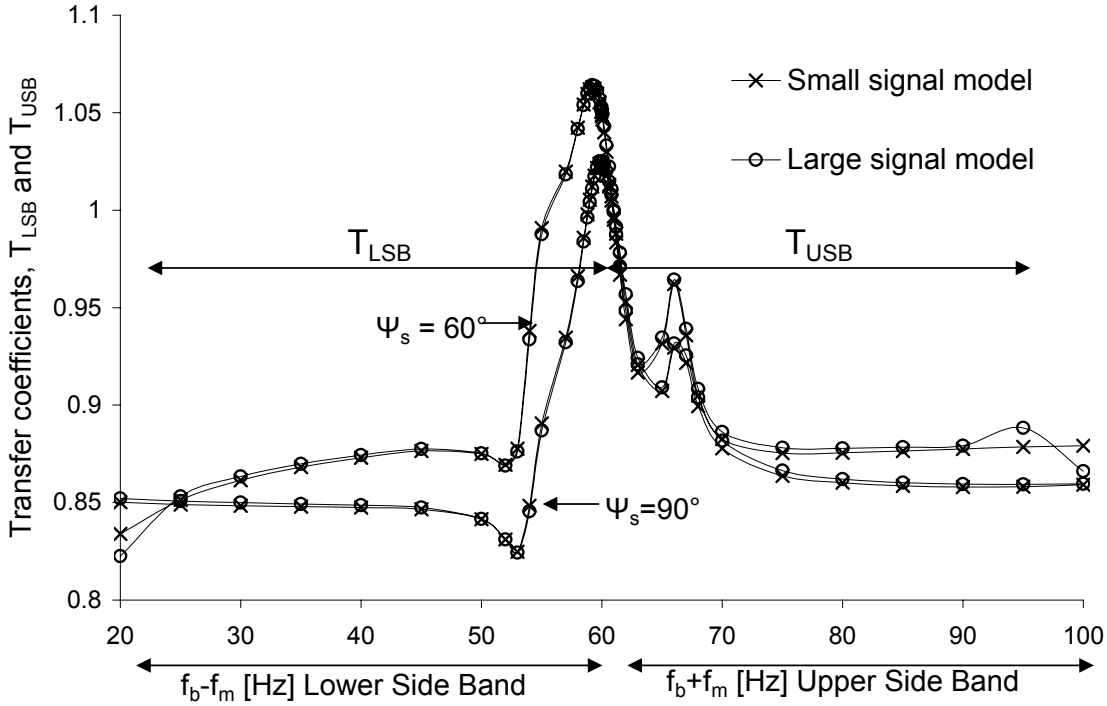

Figure 5.11: Variation of transfer coefficients of voltage side bands (T_{LSB} and T_{USB}) with side band frequency ($f_b \pm f_m$) for $\psi_s = 90°$ and $\psi_s = 60°$ for the 2250hp motor

this purpose the flicker transfer coefficient from A to B is defined (T_{PstAB}) as:

$$T_{PstAB} = \frac{P_{stB}}{P_{stA}} \tag{5.12}$$

where P_{st} is the short term flicker severity and subscripts at A and B denote the corresponding values at A and B respectively. Noting that for regular voltage fluctuations $P_{st}^2 \propto P_{it}$, where P_{it} is the instantaneous flicker sensation, (5.12) can be re-written as;

$$T_{PstAB} = \sqrt{\frac{P_{itB}}{P_{itA}}} \tag{5.13}$$

Determination of P_{itA} and P_{itB} requires voltage waveforms at A and B which can be established using the outputs of the small signal model and the steady state voltages at A and B. Figure 5.12 illustrates the variation of the flicker transfer coefficient

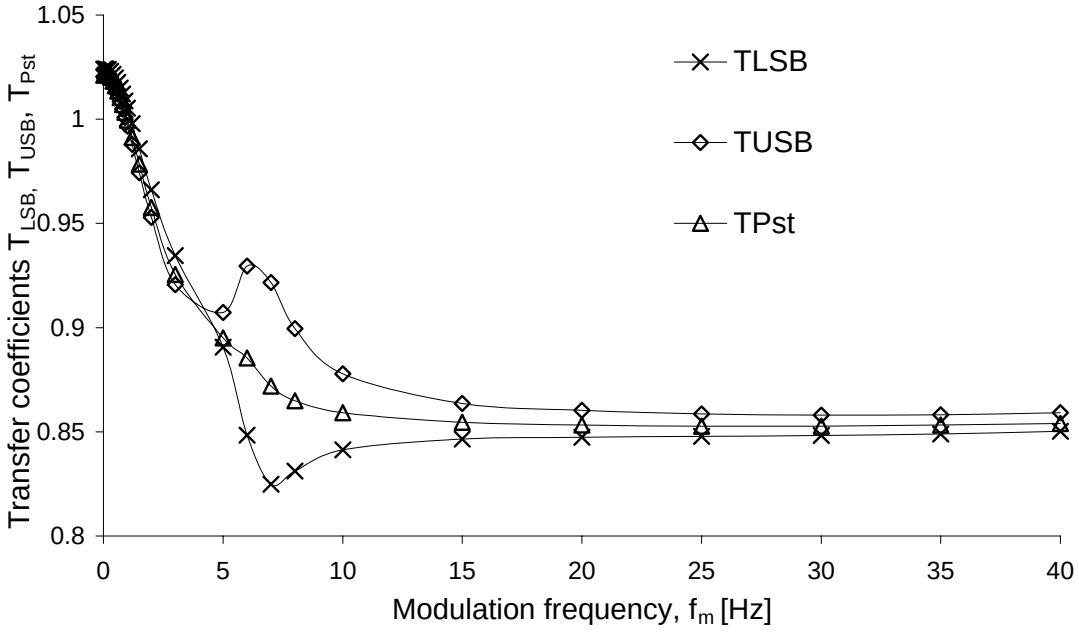

Figure 5.12: Comparison of the transfer coefficients of the side bands (T_{LSB} and T_{USB}) and flicker transfer coefficient, T_{Pst}

(T_{PstAB}) and the transfer coefficients of the side bands of the 2250hp motor with modulation frequency f_m. It indicates that the flicker transfer coefficient is less than unity for most of the modulation frequencies. As f_m increases T_{PstAB} decreases, a behaviour that was noted in relation to the side band attenuation as well. Moreover, it is seen that for a given modulation frequency f_m, the magnitude of the flicker transfer coefficient lies between the two transfer coefficients of the lower and upper side bands respectively. Contrary to the peak and trough exhibited by the two side bands in relation to attenuation between $f_m = 5$Hz and $f_m =$10Hz, the flicker transfer coefficient does not exhibit a significant shift from its gradual reduction with f_m. Figure 5.12 also illustrates the flicker magnification at low modulation frequencies similar to what was exhibited by the individual side bands.

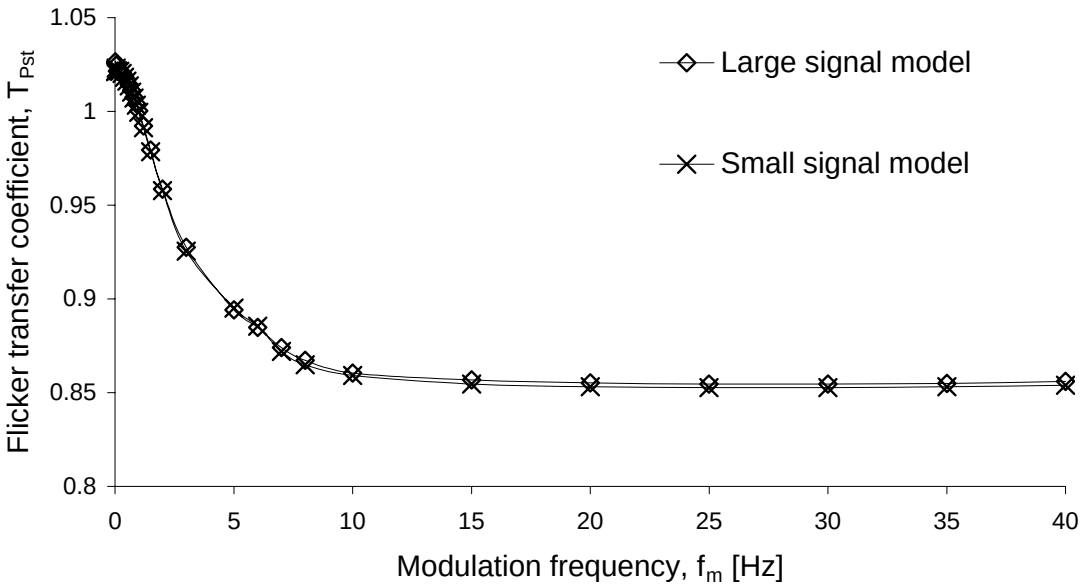

Figure 5.13: Comparison of flicker transfer coefficients (T_{PstAB}) established using small and large signal models

5.4.2 Accuracy of Small Signal Modelling

In the radial system of Figure 5.1, when the upstream supply voltage is sinusoidally amplitude modulated, the downstream voltage would contain additional frequency components at $f_b \pm jf_m$ ($j \neq 1$) caused by multiple armature reaction of the motor as discussed previously in Chapter 4 and hence the flicker transfer behaviour may not only be governed by the two side bands of the sinusoidally amplitude modulated voltage waveform. In the small signal model of the system presented in Section 5.2 the additional frequency components $f_b \pm jf_m$ are not accounted for as a part of the linearisation process. Hence, it is required to investigate the accuracy of the use of the small signal model in establishing the flicker transfer coefficient.

The flicker transfer coefficients established for the 2250hp motor using the small and large signal models are compared for the radial system (with a system impedance of 3%) in Figure 5.13. The absolute error involved in the evaluation of the flicker transfer coefficient using the small signal model is shown in Figure 5.14, where it

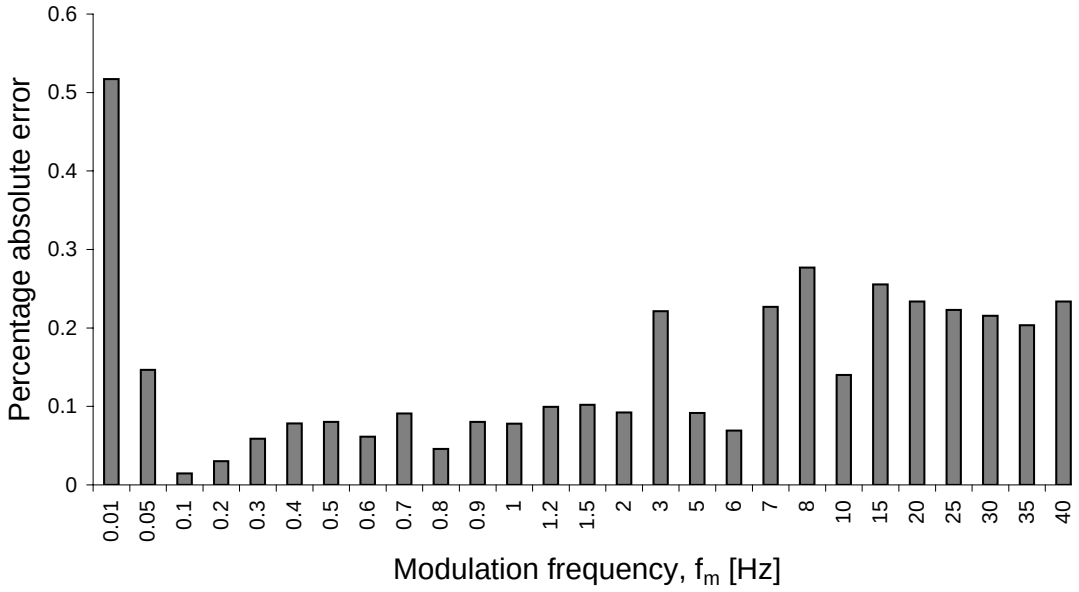

Figure 5.14: Percentage error involved in determining flicker transfer coefficient using the small signal model

can be noted that the maximum error is around 0.5%, which occurs at a very low modulation frequency $f_m = 0.01$Hz. This verifies that the additional frequency components ($f_b \pm n f_m$) that have been neglected in the small signal modelling do not have a significant impact on evaluation of the flicker transfer coefficient using small signal approach. Hence it can be concluded that the small signal model is accurate enough to investigate the response of the induction motors in relation to flicker transfer and attenuation.

5.5 Summary

Investigations were carried out to examine the contribution of induction motor loads to flicker attenuation in radial power systems using a small signal modelling technique. The model is used for establishment of transfer coefficients of the voltage perturbations that exist as side bands arising from sinusoidal amplitude modulation of the supply voltage.

The magnitude of the effective sub-synchronous or super-synchronous impedance (Z'_{motor}) of the 2250hp induction motor is found to be relatively small compared to its steady state value for most of the voltage side band frequencies under consideration (20Hz$<$ f $<$100Hz). The angle of Z'_{motor} varies over a wide range exhibiting inductive or capacitive behaviour, affecting voltage side band attenuation or magnification. The variation of the effective impedance can be attributed to the way the motor responds to each side band frequency. Consequently, the attenuation of voltage side bands and that of flicker will be dependent on the the frequency of voltage side band ($f_b \pm f_m$), and hence on the modulation frequency (f_m). As the modulation frequency increases, the attenuation of side bands and hence that of flicker is seen to increase, except at very low modulation frequencies.

Voltage side bands of which the frequency is close to the mains frequency (f_b), gets magnified at the downstream, causing a net magnification of the envelope, giving rise to a flicker transfer coefficient slightly above unity.

The transfer coefficient of a voltage side band (T_{LSB} or T_{USB}) depends on the rating of the induction motor. Amongst the three motors examined, larger motors have shown similar flicker attenuation characteristics compared to the smaller motor.

Attenuation of side bands depends on the magnitude and the angle of the system impedance (Z_s). Large inductive system impedances would result in smaller transfer coefficient for the side bands.

The small signal modelling was found to be a useful tool for flicker transfer analysis studies as it allows prediction of flicker transfer coefficient (T_{Pst}) accurately. Furthermore, the small signal models permit evaluation of frequency dependency of T_{Pst} in a more rigorous manner.

Chapter 6

Experimental Validation of Flicker Attenuation due to Induction Motor Loads

6.1 Introduction

Detailed theoretical investigations in relation to the stand alone behaviour of induction motors subjected to sinusoidal fluctuations in the supply voltage were presented in Chapter 4. This work was continued in Chapter 5 describing small signal analysis of induction motors, which can be used to examine the contribution of motor loads to the attenuation of flicker in radial radial power systems. The accuracy of small signal models was verified through large signal models developed in time domain, where good agreement was noted.

There exists no details on controlled experiments carried out to examine the influence of induction motors in relation to flicker attenuation. The work presented in in this chapter aims to fulfill that requirement, although covers a highly scaled down system typifying what exists in practice.

This chapter presents the methodology, measurements and results of laboratory experiments carried out in relation to propagation of flicker in the scaled down three-phase radial power system comprising a 3hp induction motor load at downstream. This chapter begins with a description on the experimental setup, outlining the practical matters that need to be accounted for. Propagation of regular voltage fluctuations that arise due to sinusoidal amplitude modulation of the upstream voltage is examined using on-line and off-line flickermeters and real time voltage waveforms. As per the small signal analysis in Chapter 5, effective impedance of the induction motor at sub-synchronous and super-synchronous frequencies is evaluated to justify the characteristics of attenuation of voltage fluctuations and flicker.

6.2 Experimental Set-up and Practical Matters

6.2.1 Experimental Set-up

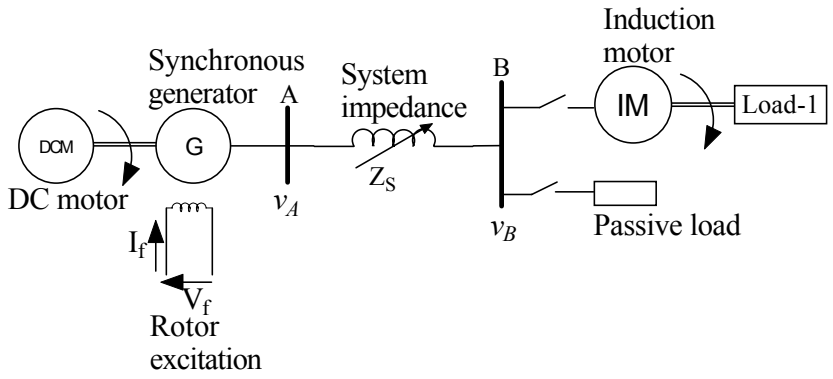

Figure 6.1: Experimental set-up of the scaled down radial network

The scaled down three-phase radial power system implemented is shown in Figure 6.1. A 5kVA, 415V, 50Hz 4-pole cylindrical rotor synchronous generator driven by a DC motor is used as the three phase voltage source and represents the upstream (A) voltage of the radial system. The DC motor is driven at 1500rpm using a DC

variable speed drive in order to obtain the required nominal voltage at 50Hz at the stator terminals of the synchronous generator.

At downstream (B) two types of loads, a 3hp three phase induction motor and a passive R-L load (with kVA and power factor equivalent to the corresponding full load values of the induction motor) are used. The two types of loads (induction motor and the passive load) can be independently switched in or out. The induction motor is coupled to a DC generator of which the generated power is dissipated in a resistor bank, all of which are represented by 'Load-1' in Figure 6.1. The impedance of the system which connects the upstream and the downstream (ie. A to B) was assumed to be purely inductive and is established using tapped reactors. Tap position was selected to obtain a system impedance (Z_S) of 10% of the full load impedance of the induction motor.

6.2.2 Generation of Voltage Fluctuations at Upstream (A)

Voltage fluctuation required to represent the upstream flicker was established by superimposing a low frequency sinusoidal current component on the DC excitation current (I_f) of the synchronous generator and hence the frequency of voltage fluctuations would be equal to that of the frequency of the superimposed ac sinusoidal current. This arrangement will give rise to sinusoidal amplitude modulated AC voltages at synchronous generator terminals, a modulation mode which is classical in flicker studies. The experimental set-up used to achieve this is shown in Figure 6.2.

The variable frequency ac voltage (V_{ac}) required to establish the superimposed sinusoidal current component in the DC excitation current was obtained using a Variable Voltage Variable Frequency (VVVF) source. However, as the ratio between the magnitude and the frequency of the output voltage of the VVVF source was constant, superimposed ac current component will be varying in its magnitude as

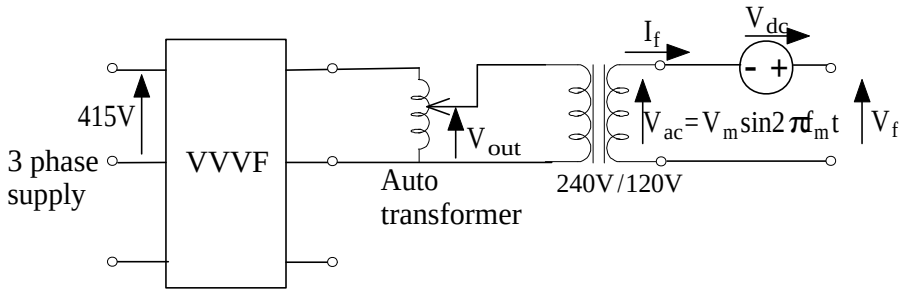

Figure 6.2: Modulating the rotor excitation current of the synchronous generator

the frequency is changed and hence in order to obtain voltage fluctuations of fixed magnitude (constant modulation depth), the output voltage of the VVVF source was regulated using an autotransformer followed by a 240V/120V transformer to provide isolation.

Assuming balanced sinusoidal amplitude modulation, with a modulation depth of m, at a modulation frequency of f_m, the line-to-neutral voltages generated at the stator terminals of the synchronous generator can be defined as:

$$v_{a,b,c} = V_p[1 + m\sin(2\pi f_m t + \phi_m)]\cos(2\pi f_b t + \phi_b - (n-1)\frac{2\pi}{3}) \qquad (6.1)$$

where,

V_p	amplitude of line-to-neutral voltage
f_b	fundamental (mains) frequency
ϕ_b	phase angle of the fundamental voltage
ϕ_m	phase angle of the modulating signal
$n = 1, 2, 3$	and
$m(=\frac{V_m}{V_p})$	modulation depth.

The two frequency components arising in the stator voltage due to amplitude modulation, one at sub-synchronous frequency $f_b - f_m$ and the other at super-synchronous frequency $f_b + f_m$ will have amplitudes of $m/2$. Similar to the identification of volt-

age perturbations described in Section 4.5.1 of Chapter 3, a voltage perturbation at frequency $f_b - f_m$ is called the lower side band (Δv_{LSB}) while the perturbation at frequency $f_b + f_m$ is called the upper side band (Δv_{USB}).

6.2.3 Practical Matters

Voltage fluctuations generated at the stator terminals of the synchronous generator using the experimental set up discussed in Section 6.2.1 is illustrated in Figure 6.3 for a modulating frequency (f_m) of 8Hz. Figure 6.4 depicts the frequency spectrum of the voltage waveform shown in Figure 6.3 where the two significant side band voltages can be seen, although they are not exactly equal in magnitudes. A possible reason for this could be the slight saliency which exists in the rotor of the synchronous generator. Also Figure 6.4 indicates that in addition to the two major side bands, sinusoidal fluctuations in excitation current has led to unwanted extra side band components of relatively small magnitudes in the stator voltage, which will be ignored in further discussions. Due to the slight speed variations of the DC motor (prime mover of the synchronous generator), fundamental frequency (f_b) was found to be fluctuating around nominal 50Hz. These practical matters have been taken into consideration while taking measurements and in the subsequent analysis of data in order to minimize possible errors.

6.3 Measurements and Results

6.3.1 Propagation and Attenuation of Voltage Side Bands with Induction Motor Load

Voltage fluctuations at upstream (A) are caused by the voltage side bands (Δv_{LSB} and Δv_{USB}) which can propagate to downstream (B) depending on the system and

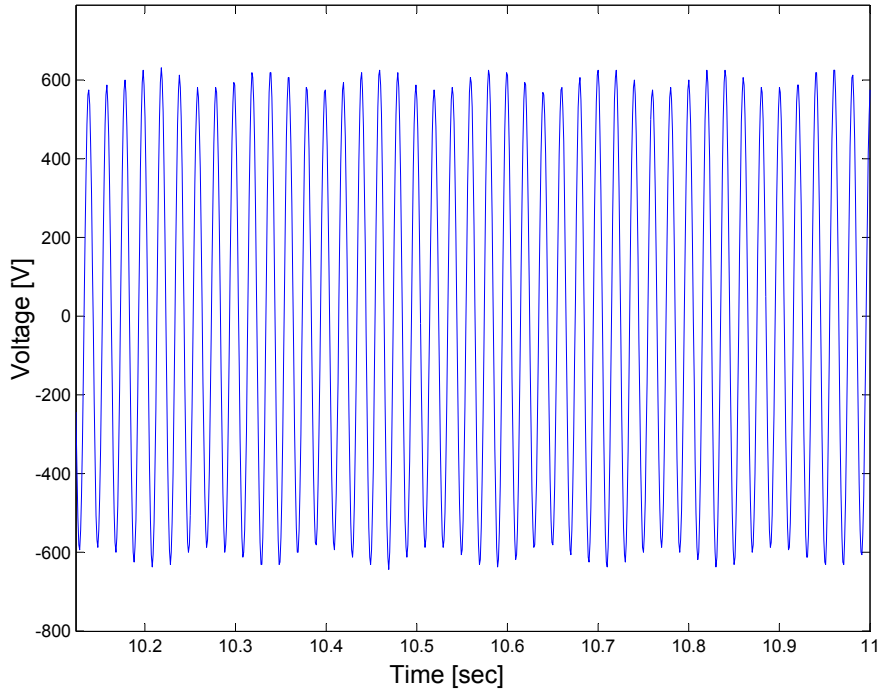

Figure 6.3: Amplitude modulated terminal voltage (line-to-line) of the synchronous generator

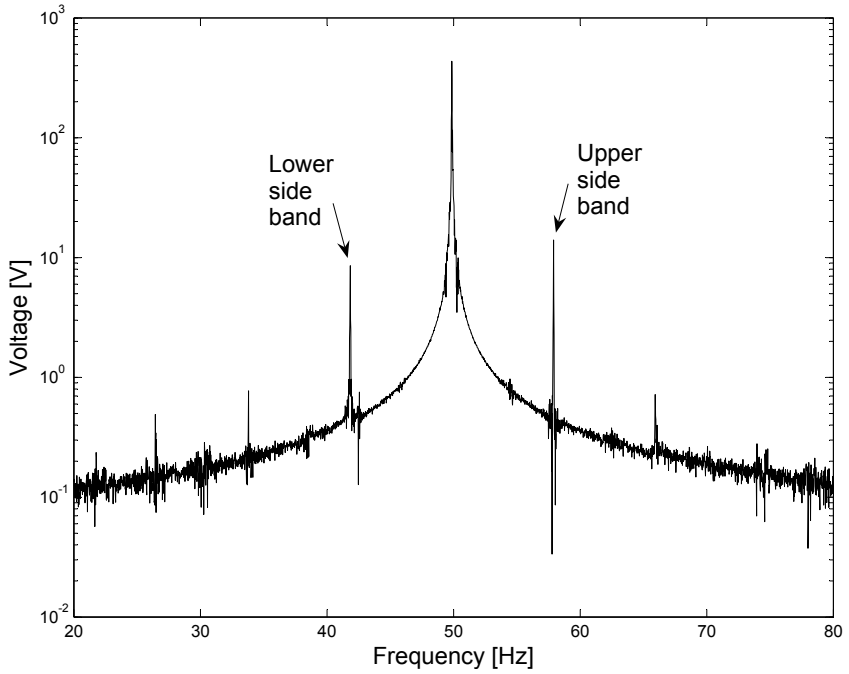

Figure 6.4: Frequency spectrum of the voltage waveform in Figure 6.3

load impedances. In order to investigate the influence of the induction motor load on propagation of voltage side bands, motor load was initially connected to B and driven nearly at its full load while the upstream voltage is fluctuated with a constant modulation depth of 5% (m =0.05) and a varying modulation frequency (f_m). Real time voltage waveforms at A and B were captured at various modulation frequencies (f_m) ranging from 1.2Hz to 36Hz covering a significant section of the nominal flicker frequency range. By Fourier analysing the captured voltage waveforms, the magnitude and angle of the voltage side bands were determined in order to establish the voltage transfer coefficient for lower and upper side bands using (5.7) and (5.8) described in Chapter 5.

Modulation frequencies (f_m) below 1.2Hz have not been used in the study as the separation of the two voltage side bands was extremely difficult unless a very high frequency resolution is used by capturing waveforms over a long window. In the present work, a window size of 50 seconds was used which would provide a frequency resolution of 0.02Hz, yet frequency leakages are unavoidable. This is due to the slight variations in the placement of frequency components on the spectrum caused by subtle deviations of the fundamental frequency from 50Hz.

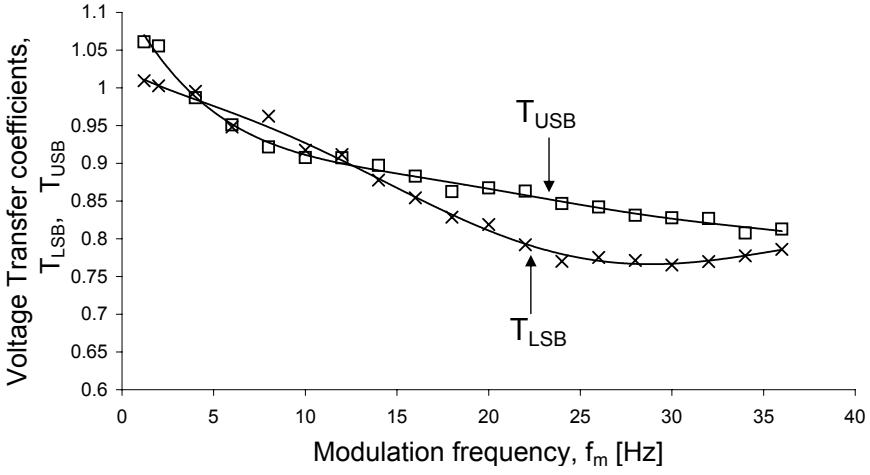

Figure 6.5: Variation of the transfer coefficients of the voltage side bands

Figure 6.5 illustrates the variation of the voltage transfer coefficients for lower and upper side bands (T_{LSB}, T_{USB}) with the modulation frequency (f_m).

Following are evident from the results of Figure 6.5.

1. As predicted from the small and large signal models described in Chapter 5, both lower and upper voltage side bands ($\Delta v_{LSB}, \Delta v_{USB}$) attenuate at the downstream for most of the modulation frequencies. The level of attenuation increases with increasing modulation frequency.

2. At relatively high modulation frequencies, the lower side band (Δv_{LSB}) attenuates to a better extent than the upper side band (Δv_{USB}).

3. At relatively low modulation frequencies where the frequencies of the two side bands are closer to the fundamental frequency, corresponding voltage transfer coefficients (T_{LSB} and T_{USB}) exhibit values slightly greater than unity, a behaviour which has also been perceived through the theoretical models presented in Chapter 5.

A qualitative justification on variable levels of attenuation of the voltage side bands depicted in Figure 6.5 is given in Section 6.3.2.

6.3.2 Determination of Effective Sub-Synchronous and Super-Synchronous Impedances of 3hp Induction Motor

The transfer coefficients defined for voltage side bands (T_{LSB} and T_{USB}) can be determined using (5.9) in Section 5.3.2 of Chapter 5 where Z'_{motor}, the effective impedance of the motor at frequency f is given by (5.10). Depending on the frequency of the voltage side band Z'_{motor} could be considered as a sub-synchronous or super-synchronous impedance.

As per the findings of Chapter 5, magnitude of Z'_{motor} may vary between 10% and 40% of the steady state impedance for the 2250hp induction motor [34] except for frequencies near the fundamental frequency. It is envisaged that, depending on the dynamic characteristics and the rating of the motor, the magnitude of the effective impedance may exhibit a different behaviour.

Effective impedance of the 3hp motor used in the experimental set-up of Figure 6.1 was calculated at various sub-synchronous and super-synchronous frequencies introduced by voltage side bands (Δv_{LSB} and Δv_{USB}) using (5.10). In this regard, the stator current side band corresponding to Δv_{LSB} and Δv_{USB} are resolved by capturing the stator current waveforms and Fourier analysing them with a window size equal to the window used for the analysis of voltage waveforms.

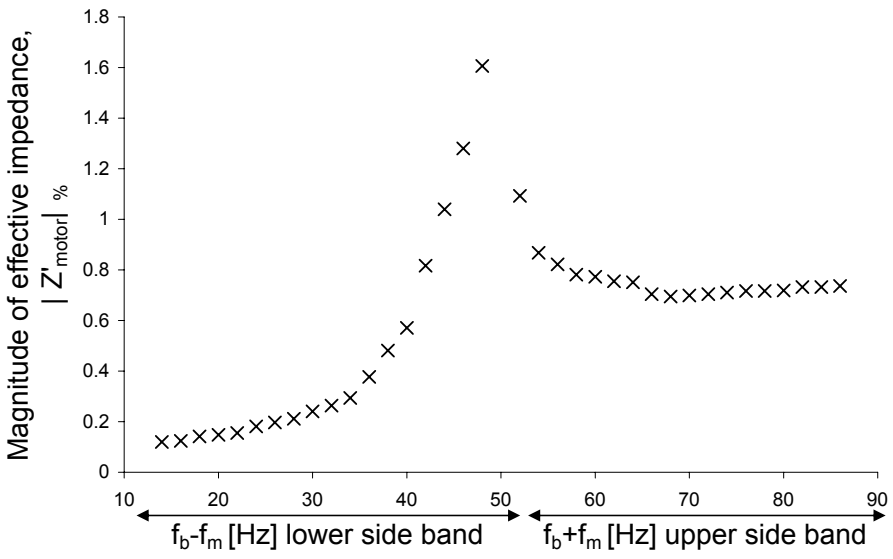

Figure 6.6: Variation of the magnitude of the effective impedance of the motor with frequency of the voltage side band

Figure 6.6 illustrates the variation of the magnitude of the effective impedance ($|Z'_{motor}|$) (normalised using the steady state impedance) with the frequency of the voltage side band. As the maximum modulation frequency used is 36Hz the effective impedance can be determined for frequencies between 14Hz (50Hz−36Hz) and 86Hz

(50Hz+36Hz). Due to the minimum modulation frequency of 1.2Hz used, $|Z'_{motor}|$ for side band frequencies between 48.8Hz and 51.2Hz have not been determined. Figure 6.6 indicates that the magnitude of effective impedance depends on the frequency of the voltage side band. It is seen that $|Z'_{motor}|$ varies between 15% to 75% of the steady state impedance for the range of frequencies considered. Relatively smaller $|Z'_{motor}|$ implies that the corresponding voltage perturbations should get attenuated at the downstream as per (5.9). Thus, in order to relate the attenuation of the voltage side bands with the effective impedance of the motor, the side band transfer coefficients (T_{LSB} and T_{USB}) illustrated in Figure 6.5 are plotted against the frequency of the voltage side band ($f = f_b \pm f_m$) as shown in Figure 6.7.

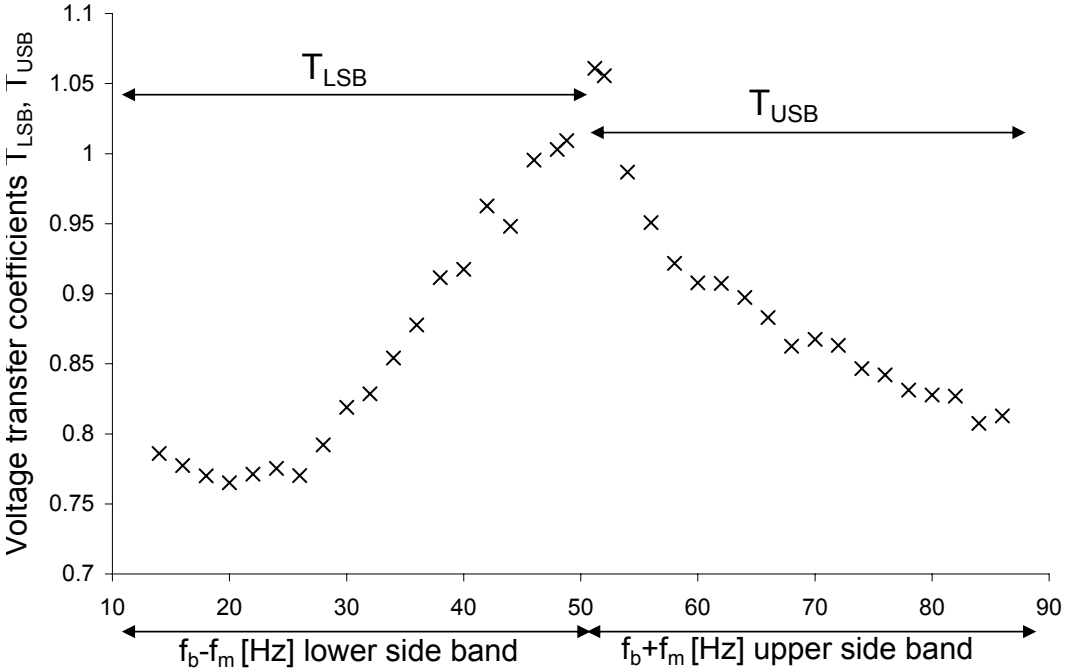

Figure 6.7: Variation of the voltage transfer coefficients of the side bands with frequency of the voltage side band

Comparison of the results of Figures 6.6 and 6.7 indicates following:

1. Relatively small effective impedance offered by the motor leads to attenuation of corresponding frequency components at downstream validating the theoretical

predictions of Chapter 5.

2. Magnitude of Z'_{motor} varies between 10% and 100% for frequencies between 14Hz and 45Hz and between 100% and 80% for frequencies between 55Hz and 86Hz. Hence, on the average $|Z'_{motor}|$ varies between 10% and 80% over the range 14Hz-86Hz except near the frequencies close to fundamental frequency (50Hz).

3. Above variation in $|Z'_{motor}|$ gives rise to smaller transfer coefficient for the lower side band compared to the transfer coefficient corresponding to the upper side band (i.e. $T_{LSB} < T_{USB}$).

4. At low modulation frequencies, that is for frequencies near the fundamental frequency, $|Z'_{motor}|$ becomes greater than the steady state impedance ($|Z'_{motor}| > 100\%$) restricting any attenuation of corresponding voltage side bands.

6.3.3 Flicker Transfer Coefficient at a Fixed Modulation Depth and Variable Modulation Frequency

In addition to real time waveform analysis described above, synchronous flicker measurements and further waveform processing were undertaken while maintaining the conditions as discussed in Section 6.3.1. This work includes

1. On-line measurement of short term flicker severity (P_{st}) levels using two flickermeters connected at A and B.

2. Off-line measurement of instantaneous flicker sensation (P_{it}) using the real time voltage waveforms at A and B which were captured in Section 6.3.1 and a PC based flickermeter developed in PSCAD/EMTDC.

Measurements 1 and 2 were repeated in relation to the equivalent passive load as well. Upstream to downstream flicker transfer coefficient (T_{PstAB}) was established

using (3.3) and (3.2) in Chapter 3 re-written as (6.2) and (6.3) for the measurements 1 and 2.

$$T_{PstAB} = \frac{P_{stB}}{P_{stA}} \tag{6.2}$$

$$T_{PstAB} = \sqrt{\frac{P_{itB}}{P_{itA}}} \tag{6.3}$$

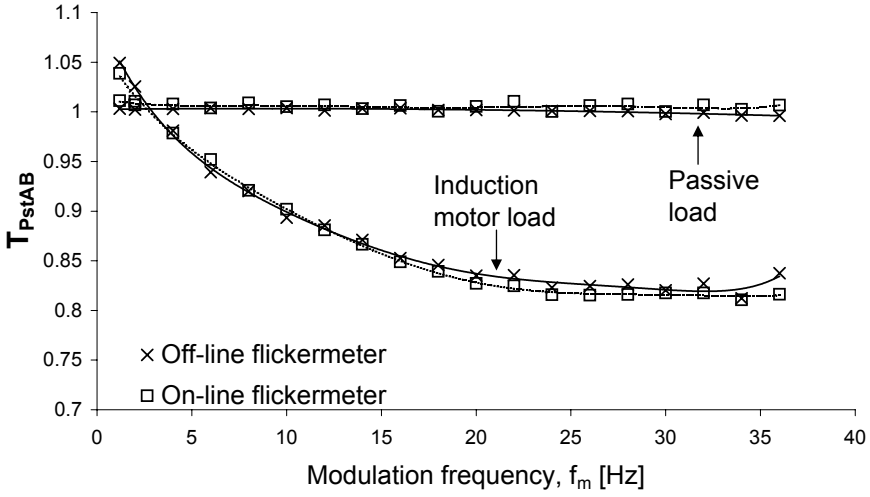

Figure 6.8: Variation of flicker transfer coefficients established using measurements 1 and 2 for downstream induction motor and passive loads

Variation of flicker transfer coefficient (T_{PstAB}) with modulation frequency (f_m) for the downstream induction motor load and the passive load established using the two measurement methods are illustrated in Figure 6.8. In relation to the downstream induction motor and/or the passive load of the test system, Figure 6.8 can be used to put forward the following points on transfer and attenuation of flicker.

1. The two flicker measurement methods have led to similar behaviour of T_{PstAB} for both types of loads.

2. The characteristics of flicker attenuation exhibited by the induction motor and

passive load are seen to be qualitatively similar to the outcomes of preliminary investigations of Chapter 3 and the theoretical predictions of Chapter 5.

3. For a given modulation frequency, the induction motor load offers a transfer coefficient less than unity for most of the f_m values whereas the passive load exhibits more or less a unity transfer coefficient for any modulation frequency.

4. The flicker transfer coefficient > 1 observed at modulation frequencies less than about 2.5Hz agrees well with the observations made in Chapter 5, Sections 5.3 and 5.4.

6.3.4 Influence of Modulation Depth on Flicker Transfer Coefficient

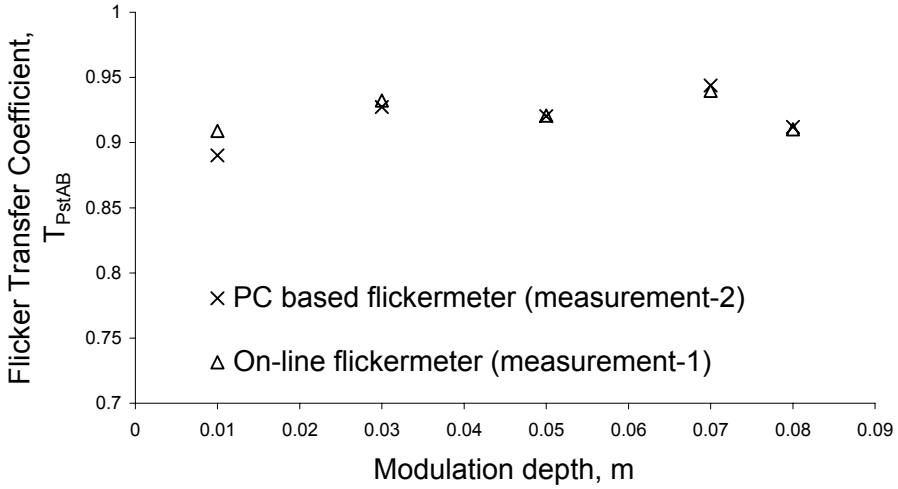

Figure 6.9: Variation of flicker transfer coefficient T_{PstAB} with modulation depth (m)

Measurements were extended to investigate the dependency of flicker attenuation by the motor on the modulation depth at upstream. Modulation depth (m) was varied from 0.01 to 0.08 while the modulation frequency was held constant. As evident from Figure 6.9, no noticeable dependency of T_{PstAB} on modulation depth can be seen.

6.4 Summary

The the work presented in this chapter mainly focused on the methodologies and analysis of results obtained using laboratory experiments carried out with the aim of investigating the validity of the principles of flicker propagation developed using theoretical work in Chapter 5.

A scaled down radial power system was implemented as the test rig using a synchronous generator representing the upstream voltage source and individually switchable 3hp induction motor and a passive load connected to the downstream through an inductive line. On-line flicker measurements have been made and off-line flicker calculations have been carried out along with waveform analysis of the upstream and downstream voltages.

The results of the experiments and data analysis can be used to establish the following major conclusions.

- The 3hp induction motor connected at the downstream assists significantly in attenuating flicker compared to equivalent passive loads connected at the same location for most of the flicker frequencies of interest.

- The degree of attenuation of flicker depends on the modulation frequency. Higher the modulation frequency better is the attenuation.

- Transfer coefficients of the individual voltage perturbations that appear as side band voltages (Δv_{LSB} or Δv_{USB}) decrease with an increase in modulation frequency causing a decrease in the flicker transfer coefficient. Various attenuation levels of voltage side bands can be justified using the effective impedance of the motor.

- At relatively low modulation frequencies induction motors do not seem to provide flicker attenuation, rather can lead to magnification of flicker.

- Flicker transfer coefficient does not exhibit a noticeable dependency on the modulation depth.

- In general the results of the experiments support the major findings of the theoretical work presented in Chapter 5.

Chapter 7

Analysis of Flicker Propagation in Interconnected Systems

7.1 Introduction

Due to the interacting behaviour of various busbars and connected loads, analysis of flicker transfer in interconnected networks is relatively more complex compared to that of radial systems. As stated in Section 2.5.3 of Chapter 2, in establishing the planning and emission limits for interconnected networks, flicker contributions from neighbouring busbars are determined using influence coefficients (K_{B-A}, K_{C-A} etc.) which in turn can be considered as transfer coefficients for voltage fluctuations from one busbar to another. The methods that can be used to establish the influence coefficients; impedance matrix method [19], load flow based method [19] and short circuit based method [22] were described in Section 2.4.4. However, these methods are primarily based on rms voltage variations and hence do not account for frequency of voltage fluctuations.

The main objective of this chapter is to examine the suitability of existing methods and extend the work in order to address their limitations. Arising from new

work, a frequency domain approach which can be used to analyse flicker transfer in interconnected networks is presented in this chapter. The proposed method can be considered as an extension to the impedance matrix method presented in [19].

The work begins with an overview of the impedance matrix method outlining the process involved in implementing it for a given network. The methodology involved in the development of the proposed frequency domain method is then described. In the proposed method, modelling of industrial loads is carried out in a more realistic approach compared to the load representation used in the impedance matrix method. Frequency domain method is then tested on three different interconnected networks to examine its applicability in estimating transfer coefficients. In order to demonstrate the influence of the load models on flicker transfer, simple networks with a few nodes are first examined. The IEEE 14 bus system [38, 39] is then used to examine the suitability of the new method to more complex example networks. The relative advantages and disadvantages of the proposed frequency domain analysis are discussed.

7.2 Impedance Matrix Method - Overview

The impedance matrix method, one of the flicker transfer analysis methods presented by Renner and Sakulin in [19], is based on the principle of fault analysis and superposition. Similar to the approaches used for calculation of short circuit levels using admittance matrix (Y), the network is analysed for small voltage variations arising at various nodes due to a sudden change in the load current (Δi_j) at a selected node. In deriving the Y matrix, synchronous generators are replaced by their subtransient reactances while their source voltage is shorted to ground. Large induction motor loads are represented by their corresponding dynamic impedances instead of equivalent steady state impedance. All other loads are represented as passive elements

except the fluctuating load connected to j^{th} node, which is represented by its changes in nodal current (Δi_j) and voltage (Δv_j) as given by (7.1).

$$\begin{bmatrix} 0 \\ . \\ 0 \\ \Delta i_j \\ 0 \\ . \\ 0 \end{bmatrix} = \begin{bmatrix} Y_{1,1} & . & . & Y_{1,j} & . & . & Y_{1,n} \\ . & . & . & . & . & . & . \\ Y_{j,1} & . & . & Y_{j,j} & . & . & Y_{j,n} \\ . & . & . & . & . & . & . \\ Y_{n,1} & . & . & Y_{n,j} & . & . & Y_{n,n} \end{bmatrix} \begin{bmatrix} \Delta v_1 \\ . \\ . \\ \Delta v_j \\ . \\ . \\ \Delta v_n \end{bmatrix} \tag{7.1}$$

By employing the impedance matrix, which can be established using admittance matrix given in (7.1), it can be shown that voltage fluctuations arising at the i^{th} node due voltage fluctuations at the j^{th} node will take place according to the ratio:

$$\left|\frac{\Delta v_i}{\Delta v_j}\right| = T_{Pst_{ji}} = \left|\frac{Z_{ij}}{Z_{jj}}\right| \tag{7.2}$$

As the admittance matrix is defined at mains frequency, the transfer coefficient ($T_{Pst_{ji}}$) represents changes in the amplitude of the fundamental frequency component only. Hence, dependency of flicker propagation on modulation frequency (f_m) cannot be examined employing this method.

7.3 A Frequency Domain Method of Analysis of Flicker Transfer

7.3.1 Methodology

The objective of the work is the development of a suitable method of analysis that accounts for frequency dependent characteristics of flicker transfer and influence of dynamic loads on flicker attenuation. Small signal analysis of networks is again employed.

The methodology involves linearisation of the network around an operating point in the d-q domain in synchronously rotating reference frame. The system components are analysed as individual linear time invariant systems (LTI) systems and combined to form a frequency dependent system matrix that defines the entire network under consideration. In the present work it is assumed that only one fluctuating load exists in the network. The node at which the fluctuating load is connected is assumed to be the reference bus for the linearisation as the fluctuating load can be considered as the source of voltage disturbance for small signal analysis. Modelling of various system components and major steps involved in deriving the flicker transfer coefficients for a given interconnected network are discussed in the following sections.

7.3.2 Modelling the System Components

General Network Element:

Transformation of a network element having a series inductive reactance (X) and resistance (R) (as shown in Figure 7.1) from a-b-c to d-q domain is carried out as follows:

$$\Delta v = A\frac{d}{dt}\Delta i + B\Delta i \tag{7.3}$$

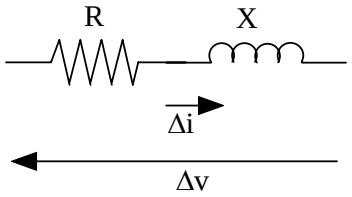

Figure 7.1: Series impedance

where,

$$A = \frac{1}{\omega_e} \begin{bmatrix} X & 0 \\ 0 & X \end{bmatrix} \tag{7.4}$$

$$\omega_e = 2\pi f_b \tag{7.5}$$

f_b is the fundamental (mains) frequency,

$$B = \begin{bmatrix} R & X \\ -X & R \end{bmatrix} \tag{7.6}$$

and, Δv and Δi are vectors representing small changes in voltage and current given by (7.7) and (7.8).

$$\Delta v = \begin{bmatrix} \Delta v_q & \Delta v_d \end{bmatrix}' \tag{7.7}$$

$$\Delta i = \begin{bmatrix} \Delta i_q & \Delta i_d \end{bmatrix}' \tag{7.8}$$

By replacing the $\frac{d}{dt}$ operator in (7.3) with Laplace operator s, d-q axes line currents (Δi) can be expressed in s-domain as:

$$\Delta i = M \Delta v \tag{7.9}$$

where

$$M = (sIA + B)^{-1} = \begin{bmatrix} a & b \\ c & d \end{bmatrix} \tag{7.10}$$

and a, b, c and d are second order transfer functions given by (7.11):

$$\begin{bmatrix} a & b \\ c & d \end{bmatrix} = \frac{1}{(X/\omega)^2 s^2 + (2RX/\omega)s + (R^2 + X^2)} \begin{bmatrix} R + (X/\omega)s & -X \\ X & R + (X/\omega)s \end{bmatrix} \tag{7.11}$$

Line Impedances:

Transmission lines are modelled as lumped series impedances as given by (7.12) neglecting the shunt capacitance.

$$Z_{line} = R_{line} + jX_{line} \tag{7.12}$$

where, R_{line} and X_{line} are resistance and reactance respectively. Hence, the changes in d-q axes current flow in a line from node i to j (Δi_{ij}) are given by (7.9). M and Δv can be defined as per (7.13) and (7.14) respectively.

$$M_{ij} = \begin{bmatrix} a_{ij} & b_{ij} \\ c_{ij} & d_{ij} \end{bmatrix} \tag{7.13}$$

$$\Delta v = \begin{bmatrix} \Delta v_{qi} - \Delta v_{qj} \\ \Delta v_{di} - \Delta v_{dj} \end{bmatrix} \tag{7.14}$$

Generators:

It is assumed that the generator control systems would not respond to the minute

variations in the bus voltage caused by fluctuating loads and hence a generator node can be considered as a fixed three phase voltage source behind a source impedance. In the present context where the analysis is carried out in relation to small signal variations, the subtransient reactance (X'_d) of the generator is assumed to be the source impedance and the generator node is represented by (X'_d) with a short circuited source voltage. Therefore the d-q domain representation of the generator node would be similar to the representation of line impedances where Δv in (7.9) would be the d-q axes voltage changes for the generator node.

Residential loads:

Residential loads are represented by series R-X type impedances. Hence transformation of such a passive load impedance from a-b-c would be similar to (7.9) where, Δi and Δv vectors represent the changes in d-q axes load current and node voltage respectively.

Industrial loads:

Industrial loads are represented by aggregated induction motors. Aggregation of the individual motors is carried out using a simple yet accurate method. The major steps involved in developing the aggregated motor are described in Appendix E. One or more aggregated motors may have to be used to best represent the total motor load as there could be a range of different sizes of induction motors.

Each aggregated motor is then represented as a small signal model using a matrix of transfer functions that relates the small variations in d-q axes voltages and

corresponding variations in current as:

$$\begin{bmatrix} \Delta i_q \\ \Delta i_d \end{bmatrix} = \begin{bmatrix} G_1(s) & G_2(s) \\ G_3(s) & G_4(s) \end{bmatrix} \begin{bmatrix} \Delta v_q \\ \Delta v_d \end{bmatrix} \tag{7.15}$$

where, $G_1(s)$ - $G_4(s)$ are fifth order transfer functions which describe the dynamic response of the aggregated motor. State space analysis described in Section 4.3 is utilised to develop the transfer functions $G_1(s)$ - $G_4(s)$ in (7.15). Furthermore, $G_1(s)$ - $G_4(s)$ relate the variations in d-q axes voltages and currents unlike the transfer functions developed in Section 4.6.2 of Chapter 5, which relate variations in the amplitude of the voltage and the corresponding changes in d-q axes current.

Note For generator and residential load nodes, matrix M will be of the form:

$$\begin{bmatrix} a_i & b_i \\ c_i & d_i \end{bmatrix} \tag{7.16}$$

where, i is the node number.

7.3.3 The Complete System

Conventional nodal approach is used to relate the node voltages and currents to combine the individual LTI systems in a network containing n number of nodes as:

$$[\Delta i_{sys}] = [Y(s)][\Delta v_{sys}] \tag{7.17}$$

where,

$$[\Delta i_{sys}] = [0\ 0\ \ldots\ \Delta i_{qm}\ \ldots 0\ 0\ 0\ .\ \Delta i_{dm}\ \ldots\ ]' \tag{7.18}$$

$$[\Delta v_{sys}] = [\Delta v_{q1}\ \Delta v_{q2}\ \ldots \Delta v_{qm}\ \ldots\ \Delta v_{qn}\ \Delta v_{d1}\ \Delta v_{d2}\ \ldots\ \Delta v_{dm}\ \ldots\ \Delta v_{dn}]' \tag{7.19}$$

$Y(s)$ can be defined as a system transfer matrix that has dimensions $2n \times 2n$, which includes all system components such as generators, loads and lines. The effect of the fluctuating load at m^{th} busbar is represented by Δi_{qm} and Δi_{dm}. The node voltages can be expressed as:

$$[\Delta v_{sys}] = [Z(s)][\Delta i_{sys}] \tag{7.20}$$

where,

$$[Z(s)] = [Y(s)]^{-1} \tag{7.21}$$

and,

$$Z(s) = \begin{bmatrix} Z_{1,1}(s) & \cdots & Z_{1,m}(s) & \cdots & Z_{1,n} & Z_{1,n+1}(s) & \cdots & Z_{1,n+m}(s) & \cdots & Z_{1,2n}(s) \\ \vdots & \cdots & \vdots & \cdots & \vdots & \vdots & \cdots & \vdots & \cdots & \vdots \\ \vdots & \cdots & \vdots & \cdots & \vdots & \vdots & \cdots & \vdots & \cdots & \vdots \\ Z_{m,1}(s) & \cdots & Z_{m,m}(s) & \cdots & Z_{m,n}(s) & Z_{m,n+1}(s) & \cdots & Z_{m,n+m}(s) & \cdots & Z_{m,2n}(s) \\ \vdots & \cdots & \vdots & \cdots & \vdots & \vdots & \cdots & \vdots & \cdots & \vdots \\ \vdots & \cdots & \vdots & \cdots & \vdots & \vdots & \cdots & \vdots & \cdots & \vdots \\ Z_{n,1}(s) & \cdots & Z_{n,m}(s) & \cdots & Z_{n,n}(s) & Z_{n,n+1}(s) & \cdots & Z_{1,n+m}(s) & \cdots & Z_{1,2n}(s) \\ Z_{n+1,1}(s) & \cdots & Z_{n+1,m}(s) & \cdots & Z_{n+1,n}(s) & Z_{n+1,n+1}(s) & \cdots & Z_{n+1,n+m}(s) & \cdots & Z_{n+1,2n}(s) \\ \vdots & \cdots & \vdots & \cdots & \vdots & \vdots & \cdots & \vdots & \cdots & \vdots \\ \vdots & \cdots & \vdots & \cdots & \vdots & \vdots & \cdots & \vdots & \cdots & \vdots \\ Z_{2m,1}(s) & \cdots & Z_{2m,m}(s) & \cdots & Z_{2m,n}(s) & Z_{2m,n+1}(s) & \cdots & Z_{2m,n+m}(s) & \cdots & Z_{2m,2n}(s) \\ \vdots & \cdots & \vdots & \cdots & \vdots & \vdots & \cdots & \vdots & \cdots & \vdots \\ \vdots & \cdots & \vdots & \cdots & \vdots & \vdots & \cdots & \vdots & \cdots & \vdots \\ Z_{2n,1}(s) & \cdots & Z_{2n,m}(s) & \cdots & Z_{2n,n}(s) & Z_{2n,n+1}(s) & \cdots & Z_{2n,n+m}(s) & \cdots & Z_{2n,2n}(s) \end{bmatrix} \tag{7.22}$$

The three-phase bus voltage at m^{th} node where the fluctuating load is connected can be defined as:

$$v_{a,b,c} = V_p(1 + \Delta v_m)\cos(\omega_b t - (n-1)\frac{2\pi}{3}) \tag{7.23}$$

where Δv_m is the voltage fluctuation, $\omega_b = 2\pi f_b$, and $n = 1, 2, 3,$

and the d-q axes voltage changes $\Delta v_{qm}, \Delta v_{dm}$ can be shown to be derived as:

$$\begin{bmatrix} \Delta v_{qm} \\ \Delta v_{dm} \end{bmatrix} = \begin{bmatrix} \Delta v_m \\ 0 \end{bmatrix} \tag{7.24}$$

7.3.4 Voltage Transfer Coefficients for d-q axes ($T_{q_{mi}}, T_{d_{mi}}$) and Flicker Transfer Coefficient ($T_{Pst_{mi}}$)

The voltage transfer coefficients ($T_{q_{mi}}, T_{d_{mi}}$) for d-q axes, the corresponding flicker transfer coefficient ($T_{Pst_{mi}}$) and their frequency dependency can be established noting the following:

1. Using (7.20) and (7.24) the expressions for q and d axes voltage transfer coefficients ($T_{q_{mi}}$ and $T_{d_{mi}}$) can be derived as:

$$T_{q_{mi}} = \left| \frac{\Delta v_{qi}}{\Delta v_{qm}} \right| = \left| \frac{Z_{i,m}(s) - Z_{i,n+m}(s)[\frac{Z_{n+m,m}(s)}{Z_{n+m,n+m}(s)}]}{Z_{m,m} - Z_{m,n+m}(s)[\frac{Z_{n+m,m}(s)}{Z_{n+m,n+m}(s)}]} \right| \tag{7.25}$$

$$T_{d_{mi}} = \left| \frac{\Delta v_{di}}{\Delta v_{qm}} \right| = \left| \frac{Z_{i+n,m}(s) - Z_{i+n,n+m}(s)[\frac{Z_{n+m,m}(s)}{Z_{n+m,n+m}(s)}]}{Z_{m,m}(s) - Z_{m,n+m}(s)[\frac{Z_{n+m,m}(s)}{Z_{n+m,n+m}(s)}]} \right| \tag{7.26}$$

   where, $i = 1, 2, ..n$ and $i \neq m$.

   $T_{q_{mi}}$ and $T_{d_{mi}}$ give the magnitudes of q and d axes voltage changes at i^{th} node with respect to 1 pu voltage change in q-axis voltage at m^{th} node noting that Δv_{dm} =0 as given by (7.24).

2. The voltage fluctuation at the m^{th} node (Δv_m) where the fluctuating load is connected, and hence corresponding q-axis voltage variation (Δv_{qm}) as a sinusoidal signal is described by (7.27).

$$\Delta v_m = \Delta v_{qm} = \Delta v_{m_{pk}} \sin(2\pi f_m t) \tag{7.27}$$

where f_m is the frequency of the voltage fluctuation and $\Delta v_{m_{pk}}$ is the amplitude of the voltage fluctuation.

3. With the definition of Δv_{qm} of (7.27) the frequency response of (7.22) represents variations in magnitude and angle of the system impedance matrix with modulation frequency (f_m).

4. The frequency response of elements of (7.22) along with (7.25) and (7.26) can be used to establish $T_{q_{mi}}$ and $T_{d_{mi}}$ for each node in the network for different modulation frequencies (f_m).

5. The d-q axes voltage variations at each node (Δv_{qi} and Δv_{di}, $i \neq m$) can be established using (7.25), (7.26) and (7.27) for a chosen Δv_{qm} (i.e. voltage fluctuation at m^{th} node).

6. The magnitude and angle of voltage fluctuation at each node (Δv_i, $i \neq m$) can be established by converting the d-q axes voltage variations into a-b-c domain using (7.28) and steady state voltage angles (δ_i) of each node.

$$\Delta v_i = \frac{\Delta v_{qi}}{\cos \delta_i} \tag{7.28}$$

A typical load flow study will provide δ_i of each node.

7. The flicker transfer coefficient from m^{th} node to any other node i ($i \neq m$) can be defined as:

$$T_{Pst_{mi}} = \frac{\Delta v_i}{\Delta v_m} \tag{7.29}$$

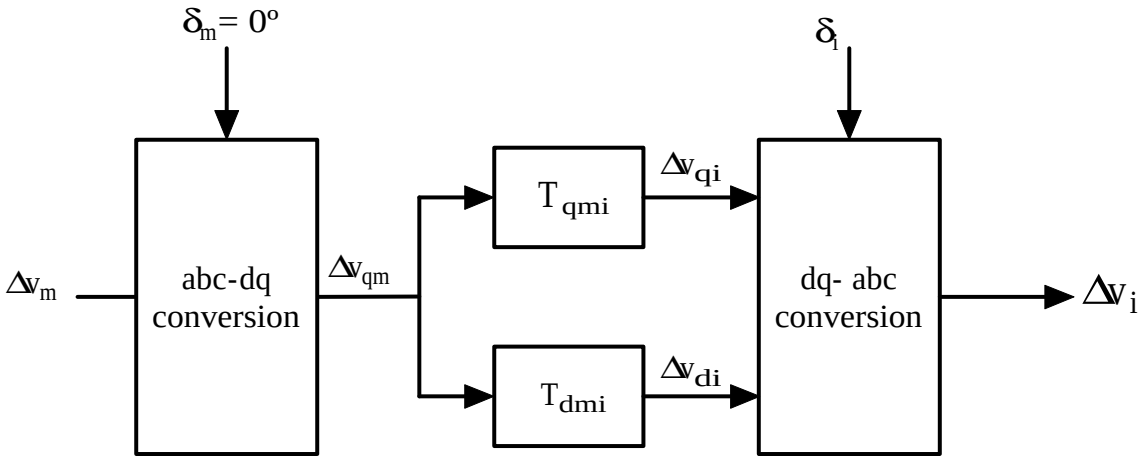

Figure 7.2: Process used to determine the voltage fluctuation at i^{th} node

The process described above is illustrated by the block diagram of Figure 7.2. As the frequency response of (7.22) is employed in the process of evaluating the transfer coefficients, the method of analysis can be considered as a frequency domain approach applicable for flicker transfer studies.

7.3.5 Implementation of the Proposed Method

The application of the proposed frequency domain method is demonstrated using three different interconnected networks;

1. An interconnected network that consists of three nodes where a generator node is not included,

2. An interconnected network that consists of three nodes with one node being a generator node [39, 40],

3. IEEE-14 bus system [39, 40],

and the results are compared with time domain simulations carried out in PSCAD/EMTDC for each case.

Case I: A Three Node Interconnected Network - No Generator Nodes

The first test network used is a simple three node interconnected system shown in Figure 7.3. An industrial load and a residential load are assumed to be connected to two of the three nodes, while the third node is assumed to be the node corresponding to the fluctuating voltage. The reason for not having a generator node in this network is that in small signal analysis the generator node is represented by its subtransient reactance (X'_d) and despite the relatively small magnitude, X'_d is still considered to be a static impedance similar to a passive load. This implies that the absence of the generator node would not affect the dynamic characteristics of the network.

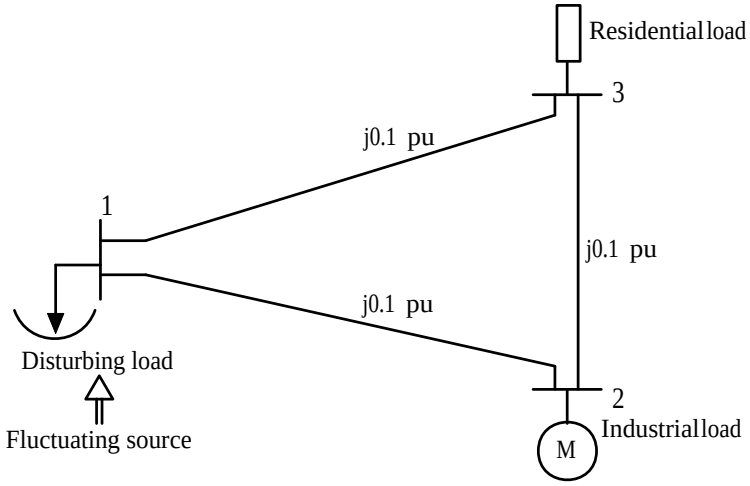

Figure 7.3: Simple interconnected network with three nodes

The system voltage is 2.3kV and the industrial load and the residential load are equivalent in their kVA capacity and power factor. The 2.3kV, 2250hp induction motor [34], as per Chapters 4 and 5 is used to represent the industrial load. Line impedances are given on a 5kVA base. However, the induction motor transfer functions are developed using its own base values. Therefore all the system components including line impedances, generators and passive loads are converted into a common per unit system applicable to the induction motor. As seen in Figure 7.3, node 1

corresponds to the disturbing load with voltage fluctuations of Δv_1 which gives rise to q-axis voltage change of Δv_{q1}.

The $Y(s)$ matrix can be established as given by (7.30) where a, b, c and d are elements of matrix M in (7.13) and (7.16). The subscripts of these elements correspond to node numbers.

$$Y(s) = \begin{bmatrix} a_{12}+a_{13} & -a_{12} & -a_{13} & b_{12}+b_{13} & -b_{12} & -b_{13} \\ -a_{12} & (a_{12}+a_{23}+G_1) & -a_{23} & (b_{12}+b_{23}+G_2) & -b_{12} & -b_{23} \\ -a_{12} & -a_{23} & a_{13}+a_{23}+a_3 & -b_{13} & -b_{23} & (b_{13}+b_{23}+b_3) \\ c_{12}+c_{13} & -c_{12} & -c_{13} & (d_{12}+d_{13}) & -d_{12} & -d_{13} \\ -c_{12} & (c_{21}+c_{23}+G_3) & -c_{23} & -d_{12} & (d_{12}+d_{23}+G_4) & -d_{23} \\ -c_{13} & -c_{23} & (c_{13}+c_{23}+c_3) & -d_{13} & -d_{23} & (d_{13}+d_{23}+d_3) \end{bmatrix} \tag{7.30}$$

The transfer matrix $Z = [Y]^{-1}$ is used to establish d-q axes voltage transfer coefficients from node 1 to 2 and 3 respectively as given by:

$$T_{q12} = \left|\frac{\Delta v_{q2}}{\Delta v_{q1}}\right| = \left|\frac{Z_{2,1} - Z_{2,4}[\frac{Z_{4,1}}{Z_{4,4}}]}{Z_{1,1} - Z_{1,4}[\frac{Z_{4,1}}{Z_{4,4}}]}\right| \tag{7.31}$$

$$T_{d_{12}} = \left|\frac{\Delta v_{d2}}{\Delta v_{q1}}\right| = \left|\frac{Z_{5,1} - Z_{5,4}[\frac{Z_{4,1}}{Z_{4,n+1}}]}{Z_{1,1} - Z_{1,4}[\frac{Z_{4,1}}{Z_{4,4}}]}\right| \tag{7.32}$$

$$T_{q_{13}} = \left|\frac{\Delta v_{q3}}{\Delta v_{q1}}\right| = \left|\frac{Z_{3,1} - Z_{3,4}[\frac{Z_{4,1}}{Z_{4,4}}]}{Z_{1,1} - Z_{1,4}[\frac{Z_{4,1}}{Z_{4,4}}]}\right| \tag{7.33}$$

$$T_{d_{13}} = \left|\frac{\Delta v_{d3}}{\Delta v_{q1}}\right| = \left|\frac{Z_{6,1} - Z_{6,4}[\frac{Z_{4,1}}{Z_{4,4}}]}{Z_{1,1} - Z_{1,4}[\frac{Z_{4,1}}{Z_{4,4}}]}\right| \tag{7.34}$$

The subscripts of Z in (7.31)-(7.34) refer to various elements of the $Z(s)$ matrix.

Figures 7.4 and 7.5 illustrate the variations of the d-q axes voltage transfer coefficients (T_{q12} and T_{q13}) and (T_{d12} and T_{d13}) with modulation frequency (f_m). According to Figure 7.4, q-axis voltage transfer coefficients predicted from the frequency domain method are in close agreement with the time domain simulation, whereas significant differences can be noticed between the predicted d-axis voltage transfer coefficient

and the time domain simulation results. However, both q and d-axes voltage fluctuations are attenuated to a better extent at node 2 where the induction motor load is connected. Values of $T_{q_{13}}$ which are less than unity, yet greater than the corresponding values of $T_{q_{12}}$, indicate that the interconnecting line between nodes 2 and 3 has assisted in attenuating voltage fluctuations at node 3.

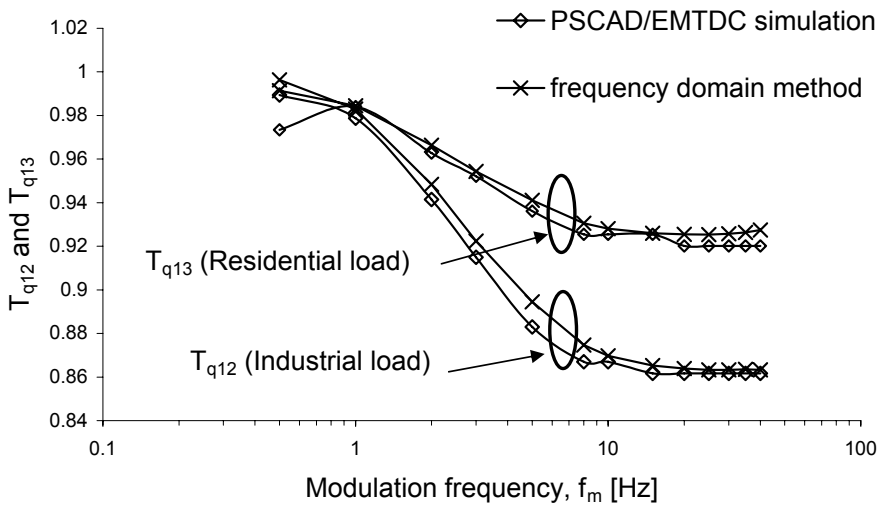

Figure 7.4: Variation of q-axis transfer coefficient with modulation frequency

By following the methodology described in Section 7.3.4, magnitudes of the voltage envelopes at nodes 2 and 3 (Δv_2 and Δv_3) can be established which in turn can be used to determine the corresponding flicker transfer coefficients ($T_{Pst_{12}}$ and $T_{Pst_{13}}$).

$$T_{Pst_{12}} = \left|\frac{\Delta v_2}{\Delta v_1}\right| \tag{7.35}$$

$$T_{Pst_{13}} = \left|\frac{\Delta v_3}{\Delta v_1}\right| \tag{7.36}$$

Variations of $T_{Pst_{12}}$ and $T_{Pst_{13}}$ with modulation frequency (f_m) are illustrated in Figure 7.6 together with the flicker transfer coefficients established using time domain simulation. By using the impedance matrix method, assuming the locked rotor

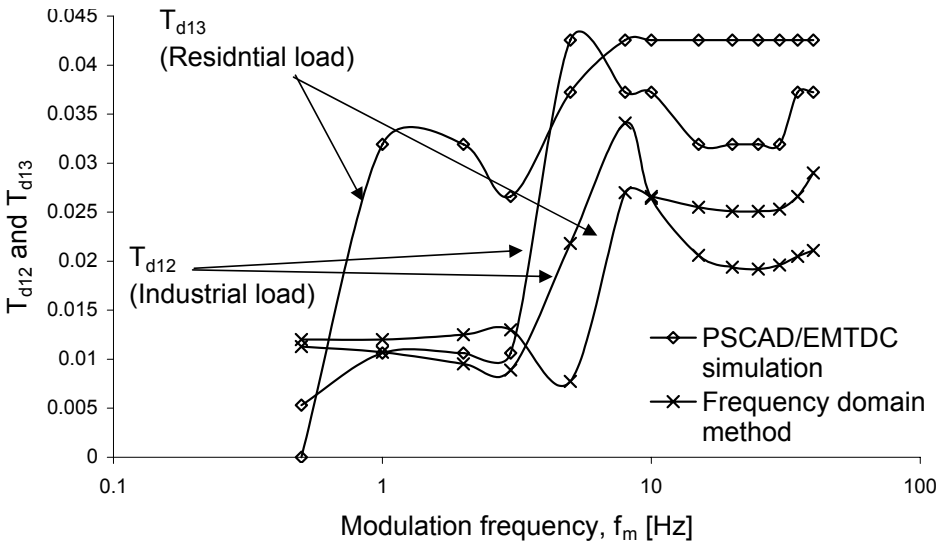

Figure 7.5: Variation of d-axis transfer coefficient with modulation frequency

impedance of the induction motor to be its fixed impedance, $T_{Pst_{12}}$ and $T_{Pst_{13}}$ can be found to be 0.86 and 0.92 respectively. These frequency independent transfer coefficients are also shown in Figure 7.6.

From the results of Figure 7.6 the following conclusions can be drawn:

1. The results of the frequency domain method agree reasonably well with those from the time domain simulations indicating the suitability of the frequency domain analysis for the network under consideration.

2. Similar to the observations in relation to the radial networks, flicker attenuation gets better with increasing modulation frequency (f_m).

3. In relation to load nodes 2 and 3, as the modulation frequency increases the transfer coefficients established using frequency domain method and time domain method are seen to converge to the fixed transfer coefficients determined using the impedance matrix method. The convergence takes place at a modulation frequency around 20Hz.

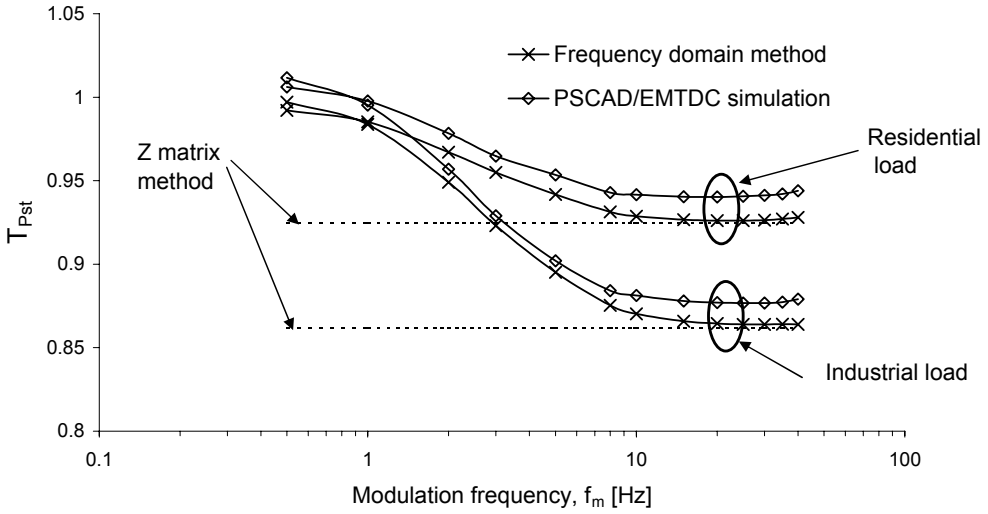

Figure 7.6: Variation of flicker transfer coefficient with modulation frequency for Case I together with those established using impedance matrix method

4. The above observation suggests that at modulation frequencies that are below 20Hz (f_m <20Hz), the impedance matrix method gives less accurate results compared to the frequency domain method.

5. However, at modulation frequencies above 20Hz (f_m >20Hz), the impedance matrix method provides promising results, implying that detailed modelling of the network may not be required if the frequency of voltage fluctuations are relatively high (f_m >20Hz).

Characteristics of flicker transfer and attenuation of flicker in relation to a single modulation frequency established using frequency domain method may depend on the network configurations and the characteristics of the aggregate induction motor loads. Therefore, it is important to assess the frequency domain method in more complex networks before making rigorous conclusions.

Case II: A Three Node Meshed Network - One Generator Node

In order to further demonstrate flicker transfer in interconnected networks and to examine the influence of generator busbars on the level of flicker attenuation at load nodes, a three node network that consist of a generator bus is considered. The network configuration has been extracted from the standard IEEE 14 bus system [39, 40]. The complete network of the IEEE 14 bus system will be investigated in Section 7.3.5.

Nodes 11, 6 and 13 in IEEE 14 bus system are used to represent nodes 1, 2 and 3 in the network under consideration as shown in Figure 7.7.

For the IEEE 14 bus system, the operating voltage is not specified and in the present work it is assumed to be 33kV. Similar to Case I, node 1 is assumed to be the busbar where the fluctuating load is connected. Node 3 is classified as a load busbar where either a passive load or induction motor load is connected, of which further details are given below:

- Motor load: One aggregated motor load, representing a total motor load of 35 $\times$ 500hp, 2.3kV, 50Hz induction motors is used. This amounts to a total P=13.5kW, and Q=5.8kVAr (lagging) at rated speed of the motors. The method discussed in Appendix E is used to aggregate the individual motors. The electrical and mechanical parameters of the aggregated motor load are given in Appendix F.

- Passive load: Constant impedance type (series connected R-L type) load which is equivalent to P=13.5kW and Q=5.8kVAr is used.

Node 2 is a generator node where a 33kV, 50Hz source with subtransient reactance of 0.12 pu is used as prescribed in the network data of the 14 bus system [39, 40].

As described in Case I, the proposed frequency domain method of analysis is used to calculate the flicker transfer coefficients from node 1 to the other two nodes. Fig-

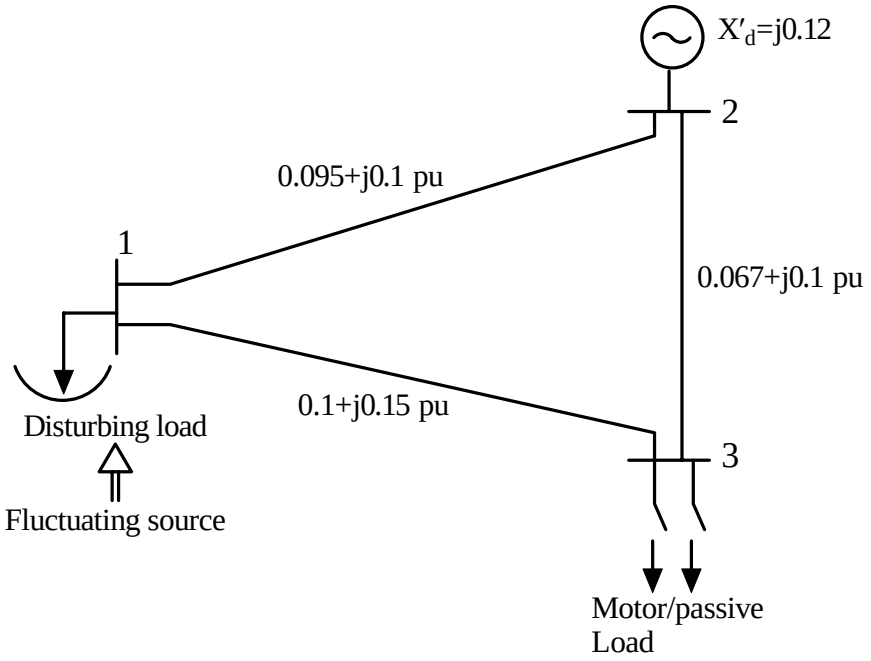

Figure 7.7: A simple three node interconnected network consisting of a generator node (derived from IEEE 14 bus system)

ure 7.8 shows the variation of the transfer coefficients with modulation frequency (f_m), established using the frequency domain method and time domain method (PSCAD/ EMTDC). In addition to the results from frequency and time domain approaches, flicker transfer coefficients calculated using the impedance matrix method [19] using the locked rotor impedance of the aggregate motor are also shown.

The following conclusions can be derived from the results shown in Figure 7.8:

1. Results from the proposed frequency domain method agree well with those from the time domain method.

2. Less flicker level at node 2 compared to node 3 ($T_{Pst_{12}} < T_{Pst_{13}}$) suggests that the contribution of the generator to compensate voltage fluctuations is substantial.

3. As already found in Case I, better flicker attenuation can be seen for higher modulation frequencies.

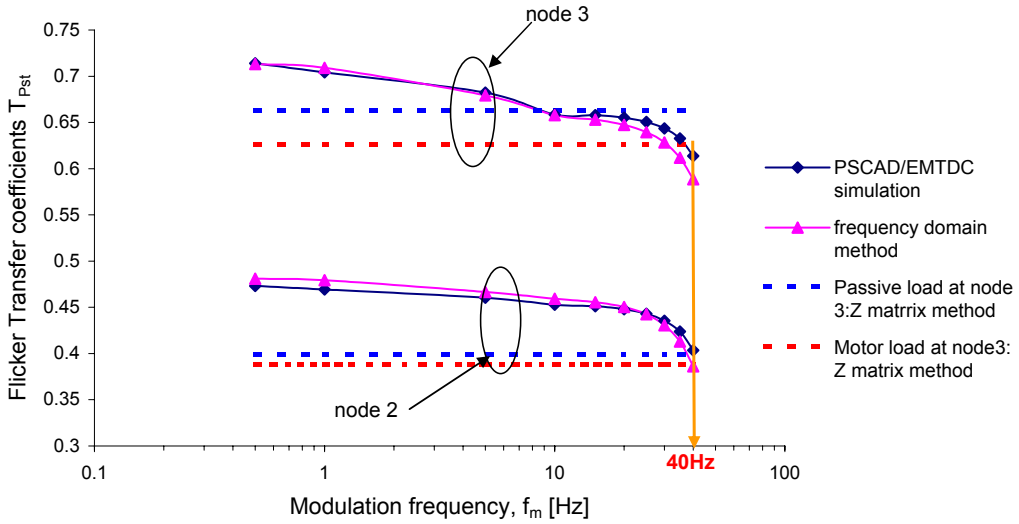

Figure 7.8: Variation of flicker transfer coefficient with modulation frequency for Case II

4. For an induction motor load at node 3, impedance matrix method gives a flicker transfer coefficient which is less than flicker transfer coefficients established using time domain and frequency domain methods. The difference between the results from the impedance matrix method and the frequency domain method (E) can be calculated using (7.37):

$$E = \left(\frac{T_{Pst-freq} - T_{Pst-Z}}{T_{Pst-Z}} \right) \times 100\% \tag{7.37}$$

where, T_{Pst-Z} and $T_{Pst-freq}$ are the flicker transfer coefficients established using impedance matrix method and the frequency domain method respectively. The results obtained using (7.37) are shown in Figure 7.9 which demonstrate that the difference becomes significant at low modulation frequencies (f_m), where a maximum difference of approximately 25% is evident at $f_m = 0.5$Hz.

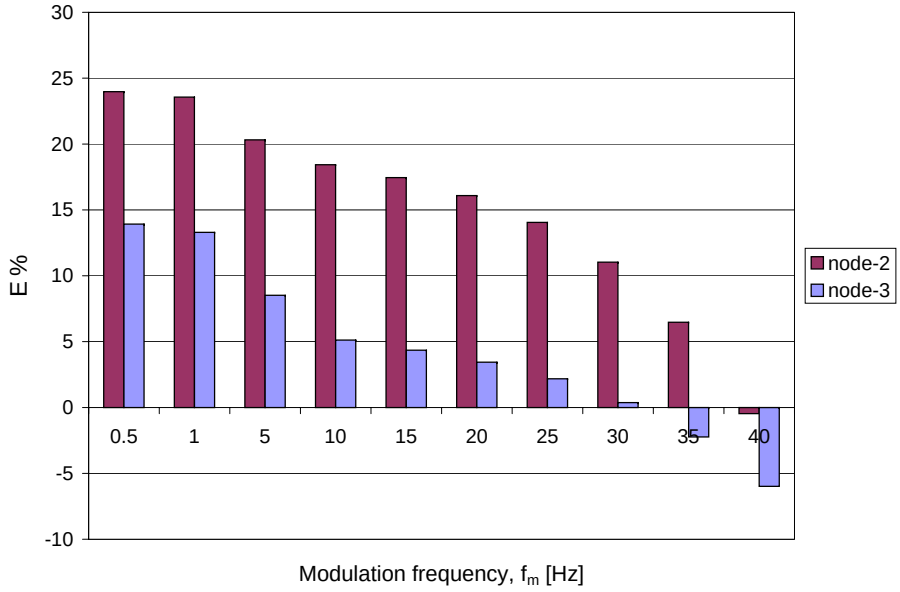

Figure 7.9: Difference between the T_{Pst} values established using impedance matrix method and frequency domain method for the network shown in Figure 7.8

Case III: IEEE 14 bus network [39, 40]

The third interconnected network used for investigations is the IEEE 14 bus system of which the single line diagram is shown in Figure 7.10 [39, 40]. The network consists of five synchronous machines, three of which are synchronous condensers. There are 11 load busbars comprising a total load of P=259MW and Q=81.3MVAr. The network data relevant the synchronous machines, loads, transmission lines are given in Appendix G [39, 40].

Magnitudes and angles of the bus voltages given in Table 7.1 were determined using load flow study carried out using Power World Simulator [40].

The load at node 11 is assumed to be the source of voltage fluctuations, and the load at node 13 is considered to be an industrial load containing a significant component of induction motor load. As it corresponds to P=13.5MW and Q=5.8MVAr the aggregated induction motor load used in Case I is employed in this section. All the other loads are modelled as constant impedance passive loads (series R-L type).

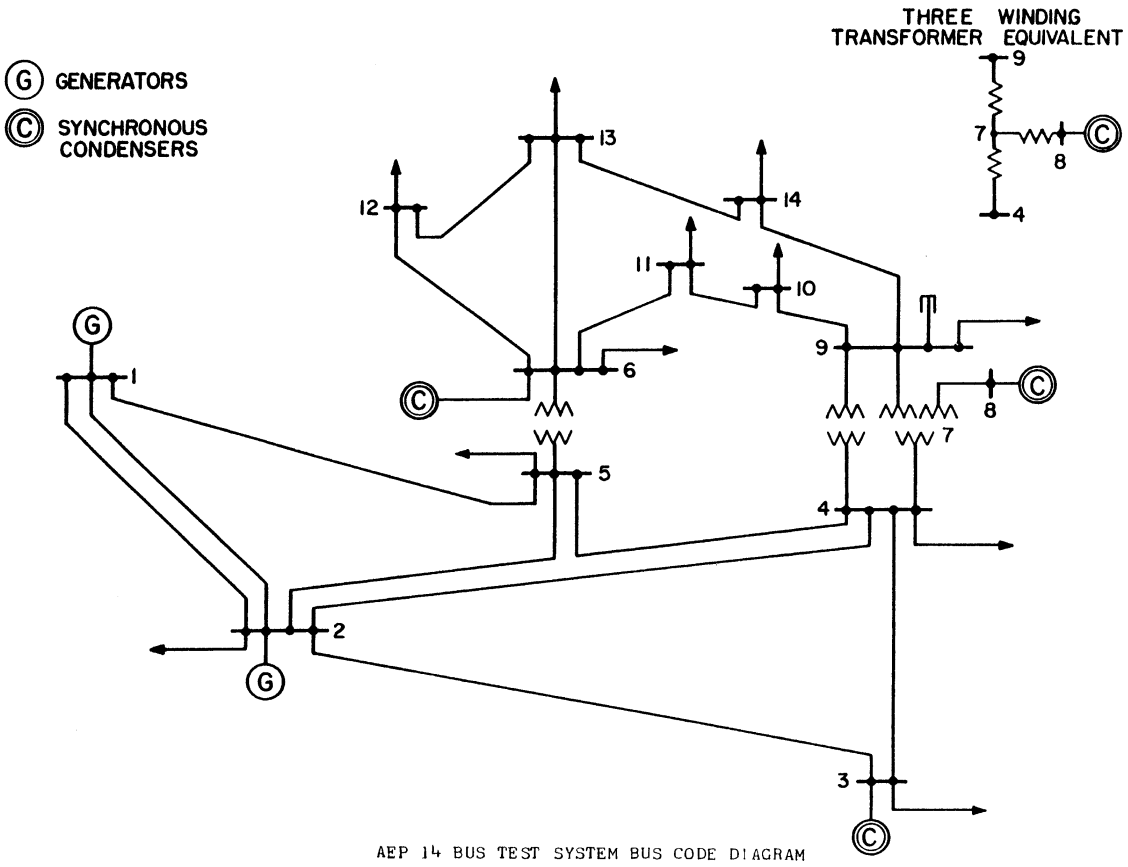

Figure 7.10: IEEE 14 bus network

Table 7.1: Magnitude and angle of bus voltages of IEEE 14 bus system

Node number	Magnitude pu	Angle degrees
1	1.06	0
2	1.045	-4.9964
3	1.01	-12.7803
4	1.0107	-10.2329
5	1.0149	-8.7265
6	1.07	-15.0475
7	1.049	-13.5233
8	1.09	-13.52
9	1.0329	-15.18
10	1.0319	-15.44
11	1.042	-15.36
12	1.054	-15.88
13	1.047	-15.9
14	1.0208	-16.52

Transmission lines are modelled as lumped impedances ignoring the line capacitance.

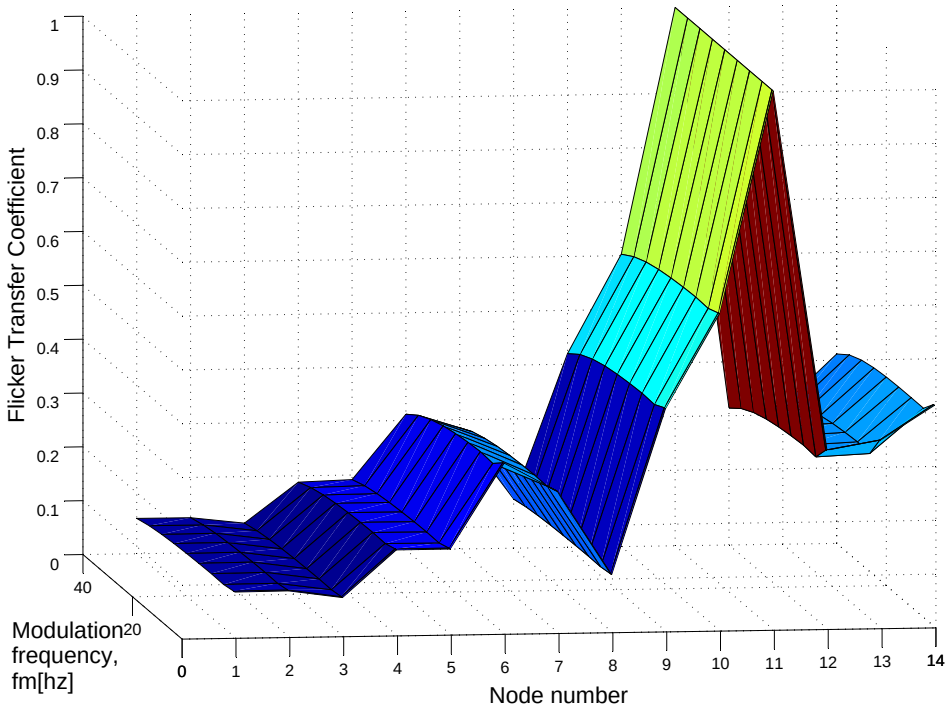

Figure 7.11: Flicker transfer coefficients of the 14 bus system established using frequency domain method

Figure 7.11 depicts the flicker transfer coefficients from node 11 to other nodes established using the frequency domain approach. It is clearly evident that due to the influence of the relatively small generator subtransient reactance, flicker levels at corresponding nodes have become significantly small compared to the flicker levels at the nodes that are in the vicinity of the fluctuating load. Low flicker levels can be identified at nodes 1, 2, 3 and 8. The highest flicker level is seen to appear at node 10 which is one of nodes that is electrically closest to the source of voltage disturbance at node 11. The variation of T_{Pst} with modulation frequency (f_m) is not strongly visible from Figure 7.11 for any of the nodes. In order to illustrate the frequency dependency of T_{Pst}, its variation with modulation frequency (f_m) is plotted in Figures 7.12 and 7.13 respectively in relation to two selected nodes:

(a) node 2: one of the least affected nodes and

(b) node 13: one of the most influential nodes where the induction motor load is connected.

The corresponding flicker transfer coefficients established using Z-matrix method are also shown in Figures 7.12 and 7.13. It is clear from these figures that, as the modulation frequency increases, the flicker transfer coefficient (T_{Pst}) established using frequency domain method decreases at both nodes 2 and 13. However, unlike in Case I and Case II, frequency dependent T_{Pst} values do not converge to the corresponding T_{Pst} values derived using Z-matrix method.

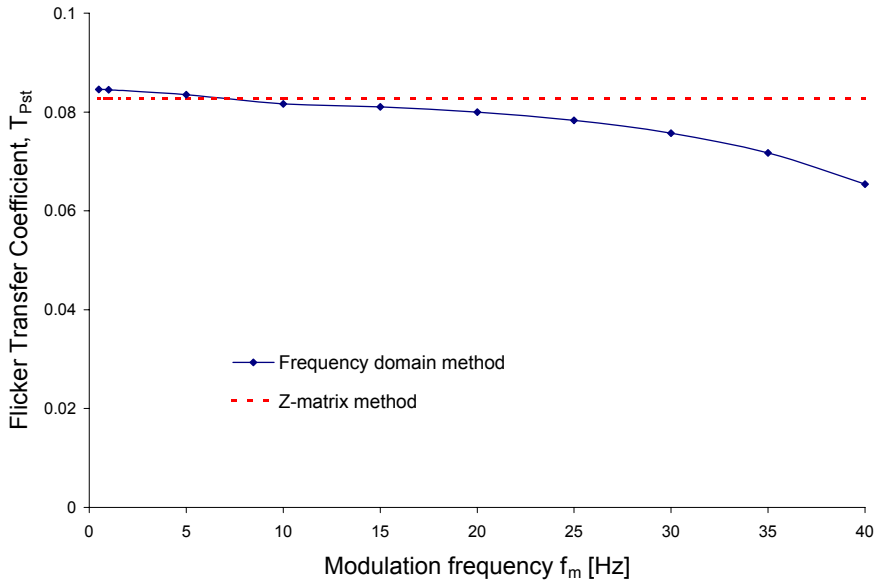

Figure 7.12: Variation of flicker transfer coefficient (T_{Pst}) with modulation frequency (f_m) at node 2

As an alternative means to illustrate the frequency dependency, the net reduction in flicker (ΔT_{Pst}), at each node including node 13 due to the induction motor load is determined using (7.38).

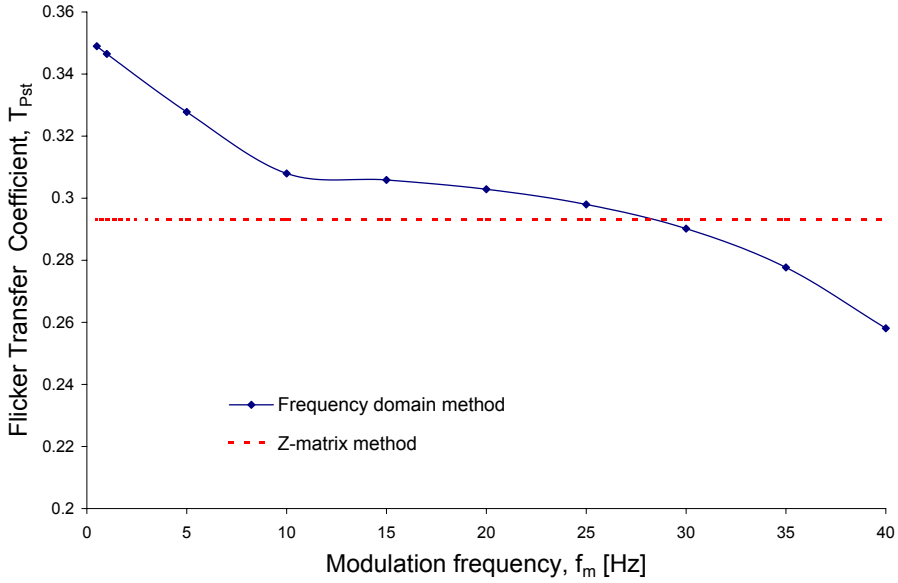

Figure 7.13: Variation of flicker transfer coefficient (T_{Pst}) with modulation frequency (f_m) at node 13

$$\Delta T_{Pst} = \left(\frac{T_{Pst-freq} - T_{Pst-passive}}{T_{Pst-passive}}\right) \times 100\% \tag{7.38}$$

where,

$T_{Pst-freq}$- flicker transfer coefficient calculated using frequency domain method with induction motor load at node 13,

$T_{Pst-passive}$- flicker transfer coefficient calculated using impedance matrix method It is to be noted that $T_{Pst-passive}$ determined using the impedance matrix method assumes node 13 consists of a passive load equivalent to the aggregated induction motor load in terms of its full load MVA and power factor, and is modelled as a constant impedance load.

Figure 7.14 illustrates the reduction in flicker at each node for three different modulation frequencies. It is evident that reduction in the flicker levels is greater at higher modulation frequencies at every node and is maximum (∼22 %) at nodes 1-3, 6, 12 and 13. This suggests that compared to the passive load the induction motor

load at node 13 is seen to help attenuate the flicker levels at remote busbars.

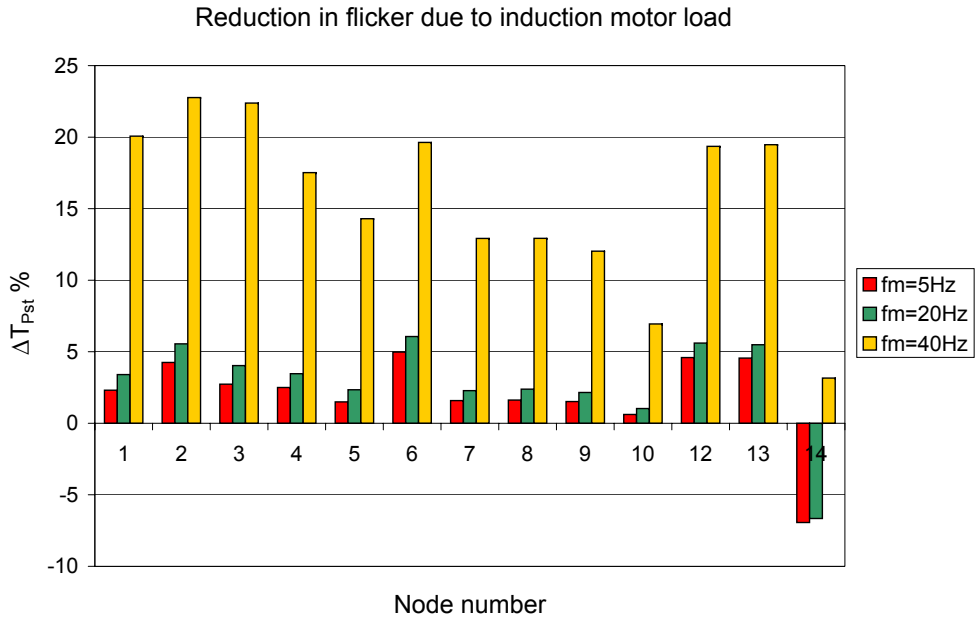

Figure 7.14: Reduction in flicker due to induction motor load at node 13

In order to examine the relative accuracy of Z-matrix method with respect to the frequency domain method, the discrepancy between the estimated transfer coefficients using the two methods can be calculated using (7.37) for each node. Figure 7.15 illustrates the variation of this error with the node number for three different modulation frequencies. For f_m =5Hz and f_m =20Hz the error in the Z-matrix method seen to be relatively small, implying flicker transfer analysis can be performed confidently using the Z-matrix method. For relatively high modulation frequencies the error becomes significant and hence detailed examination would be essential to obtain accurate results. The increase in the error with increasing modulation frequency (f_m) is due to the divergence of $T_{Pst-freq}$ values from the constant flicker transfer coefficient derived using Z-matrix method (T_{Pst-Z}). This behaviour is supported by the variations of T_{Pst} with f_m shown in Figures 7.12 and 7.13.

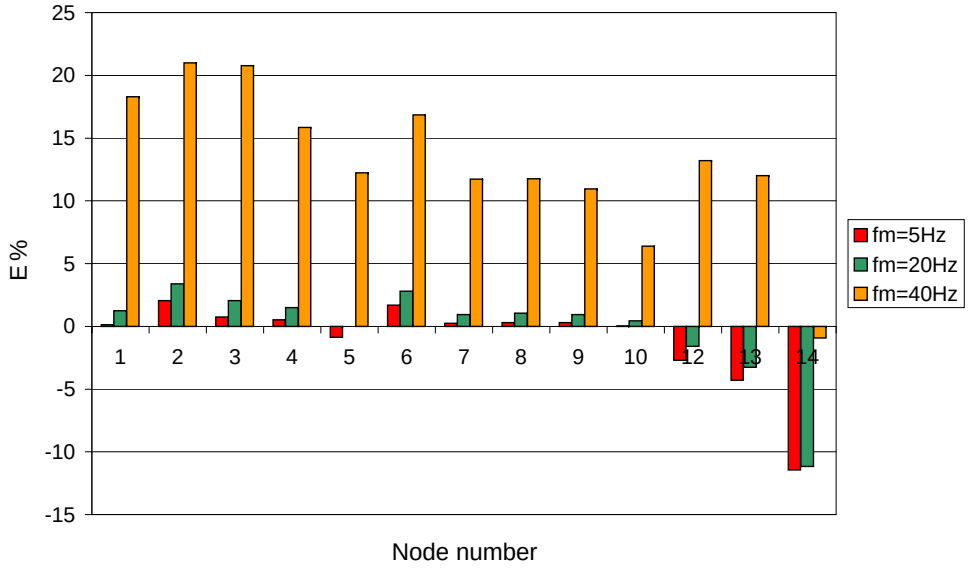

Figure 7.15: Error involved in T_{Pst} determined using Z-matrix method

7.3.6 Multiple Modulation Frequencies - Composite Modulating Signals

The flicker propagation in the example networks of Section 7.3.5 was examined using a voltage envelope (modulating signal) consisting of single modulating frequency. This leads to the hypothesis that the flicker transfer coefficient (T_{Pst}) can be determined using the magnitude of the voltage fluctuation (Δv) measured at two locations of interest as indicated by (3.3). However, practical modulating signals comprise of a range of frequencies and the dynamic response of an induction motor to such a signal in relation to total voltage fluctuation can be expected to be quite complex and hence the application of superposition may not hold true. That is, the voltage transfer coefficient determined in relation to a particular frequency component that is present in a composite modulating signal may not be equal to that predicted using a modulating signal where only that frequency component is present.

In developing a composite test signal which consists of a range of frequencies

the relative amplitudes and the phase relationships have to be considered. This offers a range of possibilities in theoretical studies which is beyond the scope of the present work and hence only a simple analysis is carried out in relation to the network considered in Case I, employing simple composite modulating signals, where the flicker attenuation is established using $T_{\Delta v}$ in relation to each frequency component present. A comparison is however made to examine the validity of superposition with the case by considering a modulating signal having only one frequency component at a time.

The analysis carried out involved the following process:

- Simulate the behaviour of the network using a composite modulating signal that comprises of a range of frequency components (between 1Hz and 40Hz with a separation of 1Hz) of equal magnitudes and equal phase angles.

- Determine the magnitude of each modulation frequency component at the load busbars (e.g. node 2 and 3) by extracting the corresponding modulating signals and using spectral analysis.

- Establish the voltage transfer coefficients ($T_{\Delta v_{12}}$) between node 1 (fluctuating node) and node 2 (load node) for each frequency component present in the composite modulating signal. This was repeated for the case where the modulating signal consisted of one frequency component at a time having a magnitude and a phase angle equal to that used in developing the composite modulating signal.

Figure 7.16 shows a comparison of the voltage transfer coefficient ($T_{\Delta v_{12}}$) of the individual frequency component of the composite modulating signal with that established by considering a modulating signal where each frequency component was present individually. The small difference between the voltage transfer coefficients established using the two approaches tend to suggest that the superposition seems to be valid in the present case. However, further theoretical work is required to

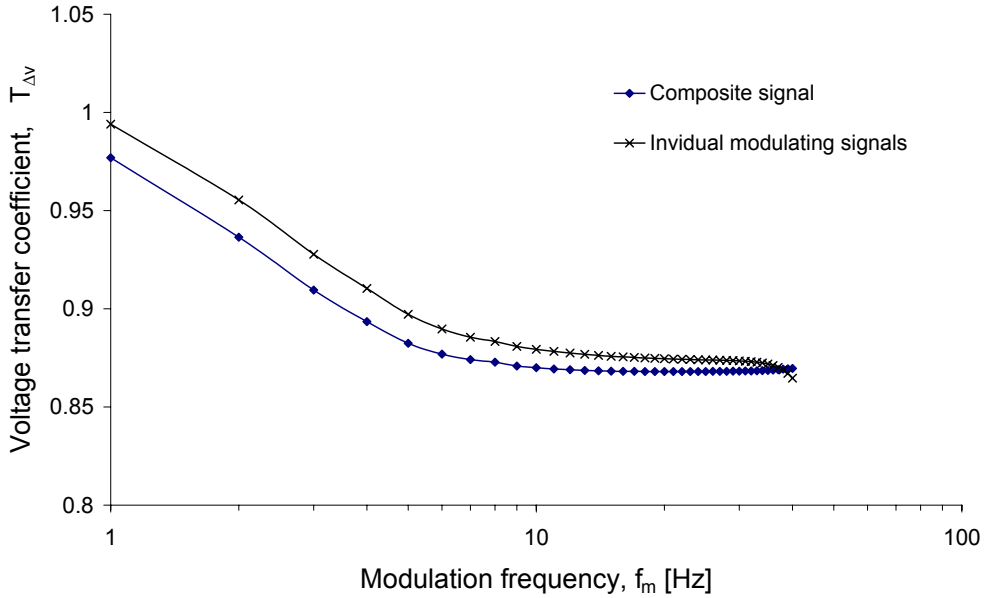

Figure 7.16: Comparison of transfer coefficients of the modulation frequencies in a composite signal with individual modulation frequencies

investigate this behaviour especially in relation to phase angles of the individual frequency components of a composite modulating signal to reach firm conclusions on the propagation of composite modulating signals.

7.4 Summary

This chapter presented a methodology, its implementation and analysis of results of a frequency domain approach that can be used for examination of flicker transfer in interconnected networks.

Small signal models of induction motors were employed to represent aggregated motor loads at industrial load busbars. The frequency domain approach was tested on three different interconnected networks and the results were compared with those obtained using the impedance matrix method.

Analysis of flicker transfer using the frequency domain approach gives more re-

alistic results compared to conventional methods of analysis such as the impedance matrix method. The results of the frequency domain approach agree well with results from time domain simulations. The results of the three example interconnected networks have revealed that the frequency domain approach can be used to establish the flicker transfer coefficient for the entire range of modulation frequencies (0.05Hz-40Hz) accurately. The range of modulation frequencies over which the two methods tend to provide similar results may however depend on the network configuration and the characteristics of the induction motor loads.

Results of the work presented in this chapter tend to suggest that the frequency domain approach is a more rigorous technique that can be used to examine the flicker attenuation behaviour when large proportions of induction motor loads exist. However, the impedance matrix approach provides reasonably valid results when such detailed studies are not warranted.

Chapter 8

Conclusions and Recommendations for Further Work

8.1 Conclusions

Through a comprehensive literature review undertaken it was revealed that the existing knowledge on flicker propagation and the effects of dynamic loads such as induction motors on flicker attenuation need further detailed research in order to develop deeper insight.

This thesis has described the development of theoretical approaches that can be used to investigate the influence of induction motor loads on flicker transfer in radial and interconnected power systems. The outcomes and findings in general will enhance the understanding on flicker propagation and attenuation and will be useful in developing an insight into the dynamics of induction motors in relation to attenuation of flicker.

Preliminary investigations on flicker propagation were carried out using time domain simulations of radial networks and measured waveform data from a sub-transmission network. The general behaviour of flicker transfer from one voltage level

to another in the network and the influence of induction motor loads on attenuation of flicker were examined. In relation to the sub-transmission network considered, spectral analysis was used to establish hypothetical transfer coefficients for voltage fluctuations over a range of frequencies. Simulation results indicated that propagation of voltage fluctuations in a radial network from upstream to downstream is dependent on the downstream load composition.

One of the main objectives of this thesis was to investigate the dynamic response of stand-alone induction motors subjected to regular fluctuations in the supply voltage. This was accomplished through the development of small signal models of induction motors describing their mechanical and electrical response to fluctuations in the supply voltage. Investigations were carried out in relation to two types of sinusoidal voltage fluctuations in the supply voltage where (a) a positive or negative sequence sub-synchronous or super-synchronous frequency component is superimposed on the mains voltage and (b) mains voltage is sinusoidally amplitude modulated. In addition to the small signal models, a d-q domain based large signal model was implemented in MATLAB/Simulink in order to verify the small signal behaviour.

In relation to case (a) above, a positive sequence sub-synchronous or super-synchronous frequency component was found to be much more influential than a negative sequence sub-synchronous or super-synchronous frequency component of same magnitude. It has been found that a positive sequence frequency component gives rise to pulsations in the electromagnetic torque and hence in the rotor speed. Magnitude of the rotor speed oscillations was found to be very much dependent on the superimposed frequency and other parameters of the motor such as X/R ratio and inertia of the combined rotor and the load. At full load, the 2250hp, 2.3kV, 60Hz motor exhibited a maximum rotor speed oscillation of 0.65% of its steady state speed when the supply is sinusoidally amplitude modulated to a depth of 5%. Although the

amplitude of the speed fluctuation is relatively small, it has a strong influence on the variation of stator current over the frequency range of 20Hz-100Hz.

The models revealed that the rotating air gap mmf components of different magnitudes arising from a superimposed frequency component on the stator and the resultant rotor speed oscillations, tend to generate additional emf components on the rotor that would reflect back onto the stator. Hence, the spectrum of the stator current exhibits extra side bands in addition to the mains frequency and the superimposed sub-synchronous or super-synchronous frequency component. This concept of multiple armature reaction was examined in induction motors of various ratings and was found to be relatively significant for large machines for superimposed frequencies closer to the mains frequency. A good correlation was noted between the variation in the magnitude of the extra side band stator currents and the magnitude of the speed oscillations. When the largest machine (2250hp) exhibited a maximum speed fluctuation of 0.65%, the corresponding magnitude of the most dominant extra side band current was approximately 15% of full load current of the motor.

In case (b) above in relation to the amplitude modulation where there are two superimposed positive sequence frequency components, one at a sub-synchronous frequency ($f_b - f_m$) and the other at a super-synchronous frequency ($f_b + f_m$), magnitude of each side band current (at either $f_b - f_m$ or $f_b + f_m$) is governed by the response of the motor to both superimposed frequency components $f_b - f_m$ and $f_b + f_m$. This interdependency which is caused by multiple armature reaction becomes prominent for relatively low modulation frequencies ($f_m << f_b$). Therefore, it can be concluded that the principle of superposition commonly used for analysis of induction motors would not be valid for superimposed positive sequence frequencies that are in the vicinity of the mains frequency. However, in relation to a superimposed negative sequence frequency component, motors respond in a static manner over the frequency

range of interest, accordingly the principle of superposition holds valid.

The small signal analsyis was extended to develop a systematic approach that can be used to examine the flicker propagation from a higher voltage level (upstream) to a lower voltage level (downstream) in a radial network. The influence of the induction motor loads on the flicker transfer coefficient was determined for voltage fluctuations arising from sinusoidal amplitude modulation. As the first step, propagation of voltage side bands was investigated by establishing voltage transfer coefficients corresponding to side band frequencies. Attenuation of voltage side bands was correlated with the attenuation of the voltage envelope, which in turn determines the flicker transfer coefficient. Modulation frequencies between 0.05Hz and 40Hz were investigated covering the perceptible flicker frequency range. Although small signal modelling neglects the secondary effects arising as a result of the multiple armature reaction (i.e. it accounts only for the first additional side band current) the error associated with the models did not exceed 0.5% when compared with the results from the large signal models. The analysis clearly demonstrated that induction motor loads are capable of attenuating most of the modulation frequencies at downstream over the range of frequencies of interest. As the modulation frequency increases flicker transfer coefficient decreases, implying better attenuation of the high modulation frequencies compared to those at relatively low modulation frequencies.

Based on the analysis of motors with different ratings, significant differences in flicker attenuation were identified with large motors compared to small motors at low modulation frequencies. Further, flicker transfer coefficients exhibited a negligible dependance on the modulation depth. Although large voltage excursions can swing the operating point of the iron towards saturation, in practice it is very unlikely that voltage fluctuations could shift the operating point beyond the knee point of the magnetic saturation curve. In contrast to motor loads, passive loads exhibited a

near unity flicker transfer coefficient over the range of flicker frequencies of interest. On the whole it can be stated that the level of flicker attenuation from upstream to downstream in radial networks is significantly governed by the downstream load composition.

An effective sub-synchronous or super-synchronous impedance of induction motors was defined with the intention of generalising the characteristics of flicker attenuation caused by motor loads in relation to sinusoidal voltage fluctuations. The definition of an effective impedance is reliant on the type of the voltage fluctuation. This is mainly due to the nature of the overall current response caused by multiple armature reaction. In contrast to the dynamic impedance of an induction motor which is usually defined at mains frequency, the above effective impedances were evaluated at the individual frequency of each voltage perturbation. It was found that the relatively small effective impedance offered by the motor for most of the frequencies enables the motor to attenuate the corresponding frequency perturbations, leading to overall attenuation of flicker. The effective impedance corresponding to frequencies that are in the vicinity of fundamental frequency was found to be relatively large compared to the full load steady state impedance and could be inductive or capacitive. Voltage perturbations at such frequencies will be magnified at the downstream leading to a flicker transfer coefficient slightly above unity ($T_{Pst} > 1$).

Small signal models of motors were used to examine the sensitivity of flicker transfer to magnitude and angle of line impedance (of the radial network) where the results suggested that larger inductive impedances help attenuate flicker, indicating that the line impedances will also play a vital part.

Based on the overall results from the theoretical findings in relation to radial systems, it can be stated that small signal analysis of induction motors is a constructive and reliable tool for flicker transfer studies compared to the conventional

dynamic induction motor models. The former facilitates examination of both regular and irregular flicker scenarios and allows detailed examination of interdependent characteristics of motor dynamics such as multiple armature reaction and voltage magnification of low modulation frequencies.

In relation to radial systems, some of the characteristics set forth using the theoretical work were supported through laboratory experiments. The test rig used for the experiments replicated a radial network of which the downstream consists of an induction motor and a passive load that can be switched in and out independently. Propagation of flicker generated from sinusoidal amplitude modulation was examined using synchronous flicker measurements and analyses of real time waveforms. Due to the experimental limitations, very low modulation frequencies could not be established. In relation to the 3hp motor used in the experimental set-up, characteristics of flicker transfer determined from the experiments were in close agreement with those established using theoretical modelling. As predicted, better flicker attenuation was observed at higher modulation frequencies while voltage magnification was evident at relatively low modulation frequencies.

The modelling work was extended to cover propagation of flicker in interconnected networks. A frequency domain method was developed which allows establishment of transfer coefficients of voltage perturbations. Compared to the conventional methods, the proposed method employs a more realistic and rigorous representation of induction motors and hence the influence of load dynamics on flicker attenuation is incorporated in deriving the flicker transfer coefficient. This approach can be considered as an extension to the impedance matrix method proposed by Renner and Sakulin [19]. As in the case of radial networks, flicker due to sinusoidal fluctuations in supply voltage was examined.

Implementation of the proposed method in interconnected test networks revealed

that frequency domain analysis is capable of evaluating outputs that are comparable with the results from time domain analysis. The validity of the impedance matrix method where the induction motors are represented by corresponding dynamic impedances was investigated. It was found that impedance matrix method is less accurate compared to frequency domain method at relatively low modulation frequencies where the dynamic response of a motor becomes significantly frequency dependent. In general, the range of modulation frequencies over which the two methods tend to agree has been seen to depend on the network configuration and the characteristics of the induction motor loads. This suggests that, frequency dependency of flicker transfer can be ignored and hence approximate methods such as impedance matrix method has merit where approximate results are acceptable. However, use of the frequency domain analysis helps understand the propagation of voltage fluctuations of variable modulation frequencies and the influence of loads on attenuation of flicker in a more systematic manner.

In order to cater for groups of induction motors connected to load busbars, a method to aggregate the motor loads was developed. In the proposed method the individual motors are aggregated into one or more machines of which the electrical and mechanical parameters are determined using the steady state equivalent circuits and the dynamic characteristics of the electromagnetic torque and rotor speed. The proposed method has been tested under steady state and fluctuating supply conditions for different groups of motors and good correlation was noted between the results from the aggregated motor(s) and the cluster of individual motors.

8.2 Recommendations for Further Work

The work presented in this thesis was primarily focused on the development of deeper theoretical knowledge on the influence of induction motor loads on attenuating flicker.

In this regard, only regular voltage fluctuations were considered. However, in practical situations the modulating signal consists of various flicker (modulation) frequencies of which the magnitude and phase angles are constantly varying with time. Hence, it would be imperative to investigate the combined effect of multiple modulation (flicker) frequencies on the net reduction in the magnitude of voltage envelope. Some preliminary theoretical work has been carried out in Section 7.3.6 of Chapter 7 where the modulating signal consisting of multiple modulation frequencies of identical magnitudes and phase angles. Results revealed that each modulation frequency component attenuates to an extent which is similar to the case as if it was the only modulating frequency component. Nevertheless, when the phase angles of modulation frequency components are different, superposition principle may not be valid due to phase cancellations or addition. Hence, further work needs to be undertaken to examine the flicker attenuation associated with composite modulating signals.

For the work covered in this thesis, the loads are mainly classified into two groups: (a) industrial loads represented by induction motors and (b) residential loads represented by passive loads. Such a representation was used to establish a better understanding on influence of induction motors in comparison to passive loads. Typical power system load busbars supply composite loads which are usually represented by aggregate composite load models. The relationships between the flicker levels and the busbar load compositions and related aspects, such as frequency dependency of flicker, can be examined with the use of aggregate load models applicable for flicker studies. In this regard, modern loads comprising power electronic converters, variable speed drives and lighting loads need to be considered. Hence, development of suitable load models that can be used in flicker studies would be another potential research area which could be considered as an extension to the work presented in this thesis.

References

[1] IEC 60050: International electrotechnical vocabulary (IEV)- chapter 161- electromagnetic compatibility. Technical report, International Electrotechnical Commission, 1990.

[2] J Arrillaga, N R Wtason, and S Chen. *Power System Quality Assessment*. John Wiley and Sons, 2000.

[3] Thomas Keppler. *Flicker Measurements and Propagation in Power Systems*. PhD thesis, Electrical and Electronic Engineering, University of Canterbury, Christchurch, New Zealand, September 1998.

[4] AS/NZS 61000.4.15:2005 electromagnetic Compatibility (EMC) part 4.15: Testing and measurement techniques - flickermeter-function and design specifications. Technical report, Standards Australia, 2005.

[5] AS/NZS 4376:1996, flickeremeter- functional and design specifications. Technical report, Standards Australia/Standard New Zealand, 1996.

[6] A. Testa and R. Langella. Power system subharmonics. In *Power Engineering Society General Meeting, IEEE*, volume 3, pages 2237 – 2242, June 1991.

[7] J. Antenor and S. M. Deckmann. Flicker produced by harmonic modulation. *IEEE Trans. on Power Delivery*, 18(2):387–392, April 2003.

[8] Electromagnetic Compatibility (EMC) part 4.15: Testing and measurement techniques - flickermeter-function and design specifications. Technical report, Inernational Electrotechnical Committee, 2003.

[9] Adly. A. Girgis, John W. Stephens, and Elham B. Makram. Measurement and prediction of voltage flicker magnitude and frequency. *IEEE Transaction on Power Delivery*, 10(3):1600–1604, July 1995.

[10] E De Jaeger, G Borloo, and W Vancoetsem. Flicker transfer coefficients from HV to MV and LV systems. In *Proc.* 14th *International Conference on Electricity Distribution (CIRED97)*, pages 101–102, Birminhgam, UK, June 1997.

[11] S Perera, D Robinson, S Elphick, D Geddey, N Browne, V Smith, and V Gosbell. Synchronised flicker measurement for flicker transfer evaluation in power systems. *IEEE Trans. on Power Delivery*, 21(3):1477–1482, July 2006.

[12] D Stade, H Schau, and A Novitskiy. Flicker analsyis in the hv transmission system. In *Proc.* 10th *International Conference on Harmonics and Quality of Power*, volume 2, pages 541–546, October 2002.

[13] B N Ramos and J L D C Parga. An emtp study of flicker generation and transmission in power systems due to the operation of an ac electric arc furnace. In *Proc.* 9th *International Conference on Harmonics and Quality of Power*, volume 3, pages 942–947, October 2000.

[14] B N Ramos, J F M García, and M P Donsión. Study of flicker generation and transmission in interconnected electric grids. In *Proc.* 10th *International Conference on Harmonics and Quality of Power*, volume 1, pages 66–70, October 2002.

[15] M C Simöes and S M Deckmann. Flicker propagation and attenuation. In *Proc.* 10th *International Conference on Harmonics and Quality of Power*, volume 2, pages 644–648, October 2002.

[16] IEC 909: - short circuit current calculation in three phase ac systems. Technical report, International Electrotechnical Commission (IEC), 1998.

[17] M. Couvreurand E. De Jaeger and A. Robert. The voltage fluctuations and the concept of short-circuit power. In *CIGRE*, 2000.

[18] M. Couvreur, E. De Jaeger, P. Goossens, and A. Robert. The concept of short-circuit power and the assessment of the flicker emission level. In *Proc.* 16th *International Conference on Electricity Distribution (CIRED)*, volume 2, pages 2.36/1–2.36/7, June 2001.

[19] H Renner and M Sakulin. Flicker propagation in meshed high voltage networks. In *Proc.* 9th *International Conference on Harmonics and Quality of Power*, volume 3, pages 1023–1028, October 2000.

[20] Y. Y. Hong and L. H. Lee. Analysis of equivalent 10HZ voltage flicker in power systems. *IEE Proc. on Generation, Transmission and Distribution*, 146(5):447–452, September 1999.

[21] IEC/TR 61000.3.7: Ed.1.0(1996) limits - assessment of emission limits for fluctuating loads in MV and HV systems. Technical report, 2001.

[22] AS/NZS 61000.3.7:2001 limits - assessment of emission limits for fluctuating loads in MV and HV systems, Standards Australia/ Standards New Zealand. Technical report, 2001.

[23] Handbook HB264: Power quality-recommendations for the application of AS/NZS 61000.3.6 and AS/NZS 61000.3.7. Technical report, Standards Australia, 2003.

[24] CIGRE-CIRED Joint Working Group (JWG) C4.1.03. Assessment of emission limits for the connection of fluctuating load installations to MV, HV and EHV

power systems (rev.:IEC 61000-3-7). Technical report, International Council on Large Electric Systems(CIGRE), International Conference on Electricity Distribution (CIRED), March 2006.

[25] Measurement of evaluation of the flicker emission level from a particular fluctuating load, 2nd draft. Technical report, CIGRE/CIRE DWG CC02, June 2000.

[26] A. Baker. Matlab based flickermeter. Undergraduate thesis, University of Wollongong, October 2003.

[27] H. R. Schwenk. Equivalent loading of induction machines for temperature tests. *IEEE Trans. on Power Apparatus and Systems*, PAS-96(4):1126–1131, July/August 1977.

[28] H Tabatabaei-Yazdi C. Grantham and M. F. Rahman. Efficiency evaluation of three phase induction motors by synthetic loading. In *Proc. International Conference on Power Electronics and Drive Systems*, volume 1, pages 103–109, May 1997.

[29] B. C. Lesieutre, P. W. Sauer, and M. A. Pai. Development and comparative study of induction machine based dynamic p.q load models. *IEEE Trans. on Power Systems*, 10(1):182–190, February 1995.

[30] D.V. Hill. Nonlinear dynamic load models with recovery for voltage stability studies. *IEEE Trans. on Power Systems*, 8(1):166–176, February 1993.

[31] T. Omata and K. .Uemura. Aspects of voltage response of induction motor loads. *IEEE Trans. on Power Systems*, 13(4):1337–1344, November 1998.

[32] T. Thiringer. Modelling of the induction machine for supply voltage disturbances. In *Proc. International Conference on Electrical Machines (ICEM'94)*, volume 11, pages 41–46, September 1994.

[33] A. Alexandrovitz and S. Lechtman. Dynamic behaviour of induction motor based on transfer function approach. In *Proc. International Conference on Electrical Machines (ICEM'94)*, volume 11, pages 41–46, September 1994.

[34] P. C. Krause. *Analysis of Electric Machinery*. John Wiley & Sons Inc., 2002.

[35] B. Ozpineci and Leon. M. Tolbert. Simulink implementation of induction machine models - a modular approach. In *Electric Machines and Drives Conference (IEMDC'03) IEEE International*, volume 2, pages 728–734, June 2003.

[36] James B. Dabney and Thomas L. Harman. *The Student Edition of Simulink: Dynamic System Simulation for MatLab, user's Guide Version 2*. Prentice Hall, Upper Saddle River, New Jersey 07458, 1994.

[37] Bimal K. Bose. *Modern Power Electronics and AC Drives*. Prentice Hall, Upper Saddle River, New Jersey 07458, 2002.

[38] N. Mithulananthan, C. A. Canizares, and J. Reeve. Indices to detect hopfbifurcation in power systems. In *In Proc. of NAPS-2000*, volume NAPS-2000, pages 15–18–15–23, October 2000.

[39] Sameh Kamel Mena Kodsi and Claudio A. Canizares. Technical report 2003.3: Modeling and simulation of ieee 14 bus system with facts controllers. Technical report, University of Waterloo, 2003.

[40] J. D. Glover and G. Digby. *Power system analysis and design: Preliminary edition software manual*. PWS Publishing Company, Boston, 1994.

[41] F. Illiceto and A. .Capasso. Dynamic equivalents of asynchronous motor loads. *IEEE Trans. on Power Apparatus and Systems*, PAS-93:1950–1659, 1974.

[42] T. Kataoka and T. Kai. A method for aggregation of a group of motor loads. In *PowerCon 2000. 2000 International Conference on Power System Technology. Proceedings (Cat. No.00EX409), Piscataway, NJ, USA*, volume 3, pages 1683–1688, 2000.

[43] M. M. A. Hakim and G. J. Berg. Dynamic single-unit representation of induction motor groups. *IEEE Trans. on Power Apparatus and Systems*, PAS-95(1):155–165, January/February 1976.

[44] G. J. Rogers, J. Di Manno, and R. T. H Alden. An aggregate induction motor model for industrial plants. *IEEE Trans. on Power Apparatus and Systems*, PAS-103(4):683–690, April 1984.

[45] F. Nozari and M. D. Kankam and W. W. Price. Agregation of induction motors for trasient stability studies. *IEEE Trans. on Power Systems*, PWRS-2(4):1096–1103, November 1987.

[46] M. Taleb, M. Akbaba, and E. A. Abdullah. Aggregation of induction machines for power system duynamic studies. *IEEE Transactions on Power Systems*, 9(4):2042–2048, November 1994.

Appendix A

Major Building Blocks of the Simulink based d-q domain Induction Motor

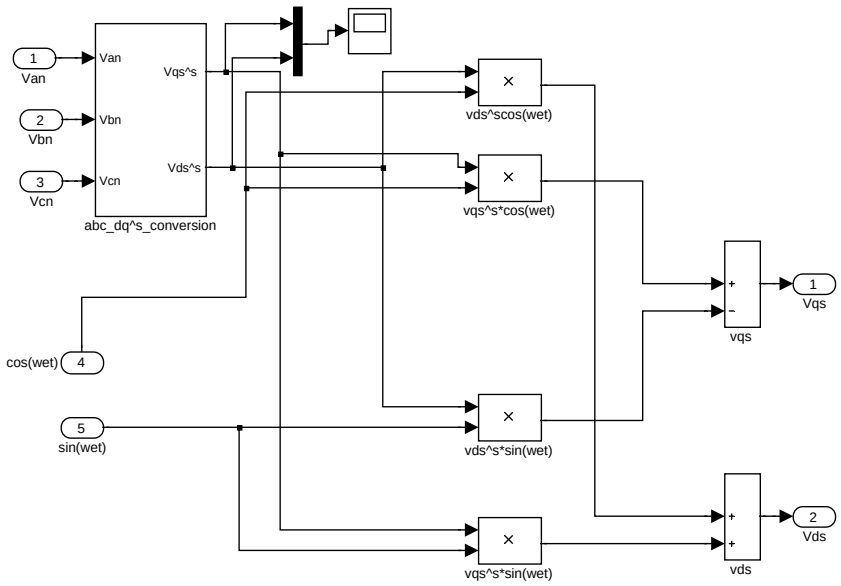

Figure A.1: Conversion of three phase voltages from a-b-c domain to d-q domain

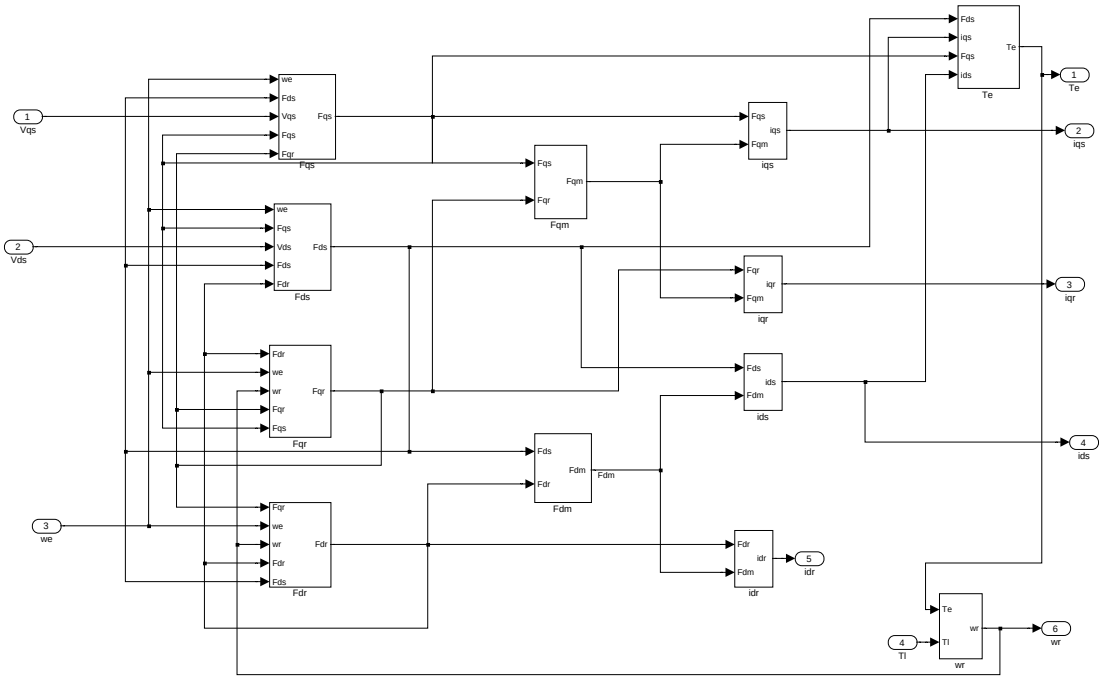

Figure A.2: Establishment of d-q axes currents using voltages-flux linkages

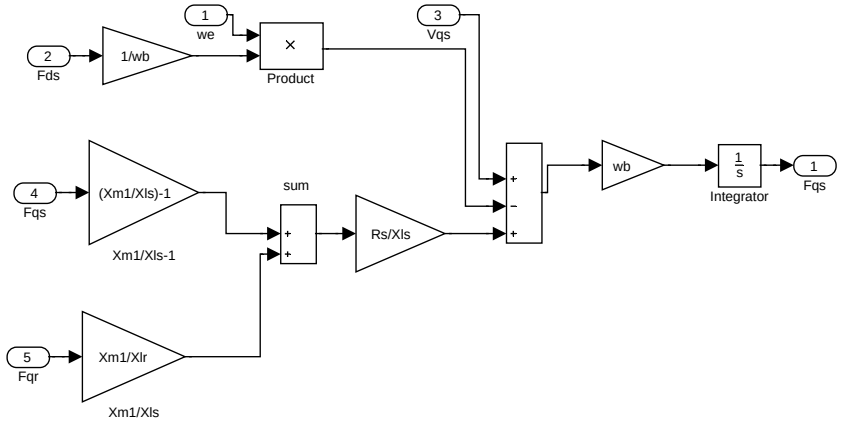

Figure A.3: Determination of q-axis flux linkage

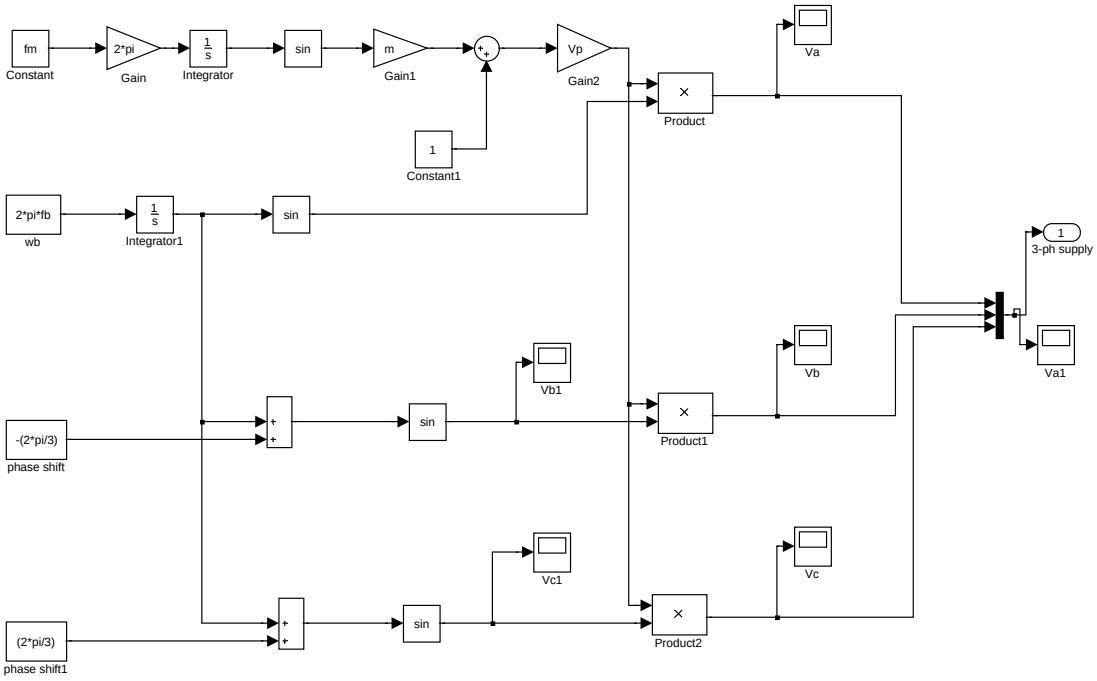

Figure A.4: Generation of sinusoidally amplitude modulated three phase supply

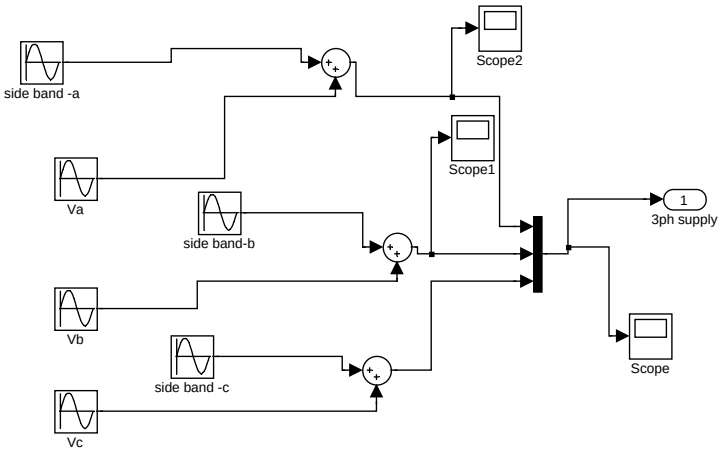

Figure A.5: Generation of three phase supply consisting a superimposed positive or negative sequence frequency component

Appendix B

Discussion on the Positive and Negative Damping

Positive and Negative Damping

A qualitative discussion on the manner in which the magnitude of the speed fluctuation varies over the range of superimposed frequencies can be developed using Figure B.1 (Figure 4.2) in conjunction with Figures B.2 and B.3 (Figures 4.5 and 4.6). In relation to the two latter figures a stator current component at $f_b - f_m$ will provide negative damping and that at $f_b + f_m$ will provide positive damping to the speed oscillations and at all times the magnitude of the speed oscillations will be curtailed by the net damping available. With reference to a particular injected frequency, the corresponding magnitude of the stator side band current will be governed by the effective impedance, whereas the magnitude of the extra side band current will be governed by both the effective impedance and the level induced voltage which is determined by the magnitude of the speed oscillations. Thus, the speed oscillations and the stator currents, especially the extra side band current can be said to be interdependent.

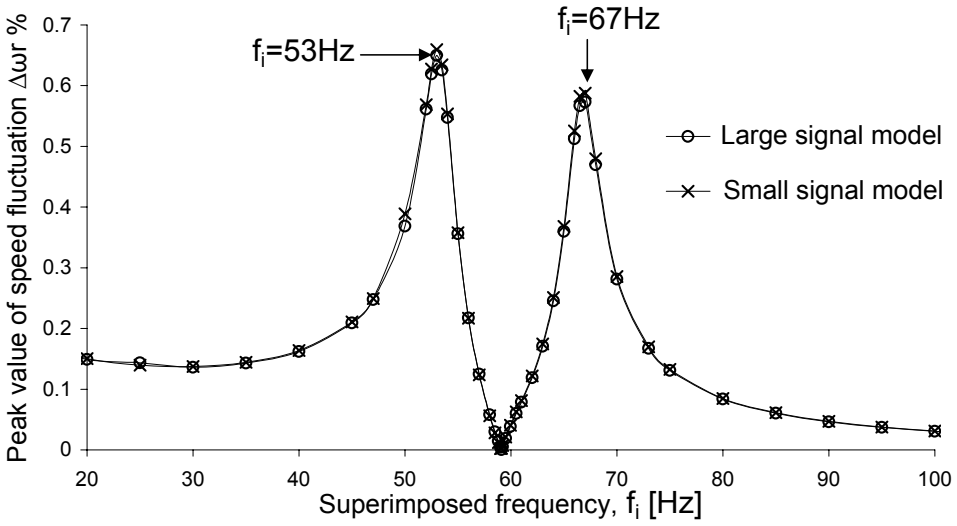

Figure B.1: Rotor speed fluctuation of the 2250hp motor with superimposed frequency established using small and large signal analyses

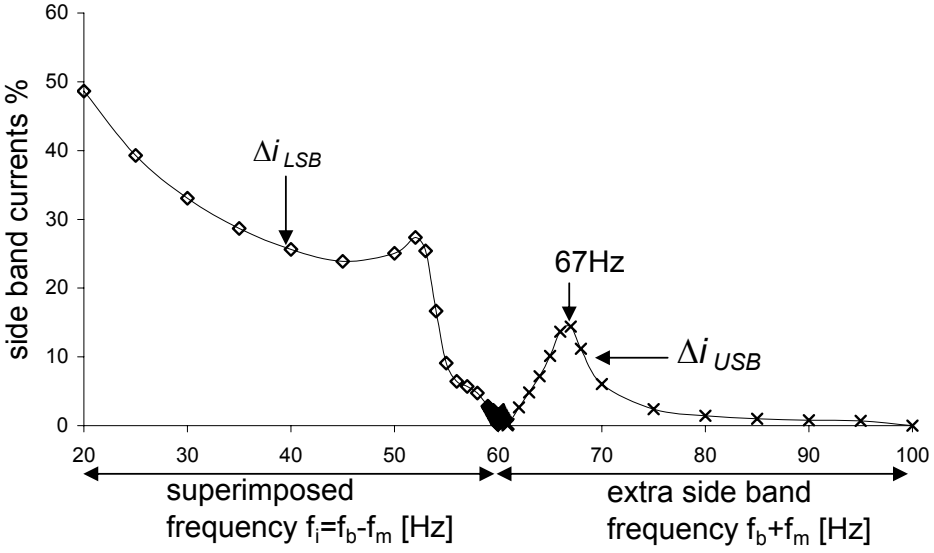

Figure B.2: Variation of stator current side bands for a superimposed lower side band for 2250hp motor: $f_i = f_b - f_m$

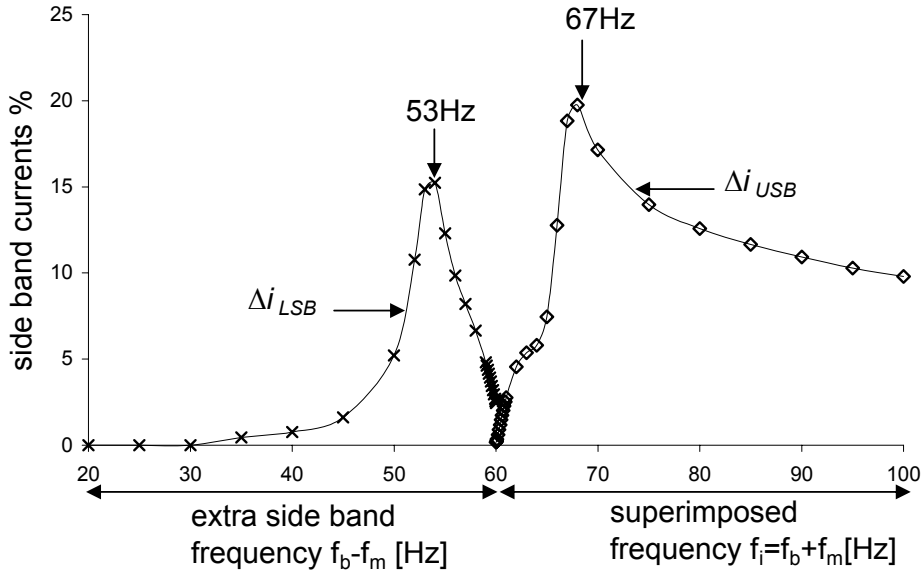

Figure B.3: Variation of stator current side bands for upper side band injection, 2250hp motor: $f_i = f_b + f_m$

Considering the case of lower side band injection, at injected frequencies close to 60Hz, the frequency and the magnitude of speed oscillation and the corresponding lower and upper side band stator currents are relatively small. As the injected frequency is reduced below 60Hz, the corresponding current will increase which is a process essentially governed by the decreasing effective impedance. This current leads to an increasing upper side band induced voltage resulting an increasing upper side band current. Increasing negative damping provided by the lower side band and increasing positive damping provided by the upper side band would lead to speed oscillations with a local maximum at 53Hz as evident from Figure B.1. As the injected frequency is further reduced below 53Hz, the lower side band current continues to increase as a result of the decreasing effective impedance whereas the upper side band current starts to decrease above 67Hz as a result of increasing frequency and reducing induced voltage. Despite the decreasing positive damping provided by the upper side band current in this frequency range (67Hz - 100Hz), the speed oscillations continue to exist well below 53Hz implying that the increasing negative damping provided by

the lower side band current is dominating the net damping.

Considering the case of upper side band injection, closer to 60Hz the upper side band current is seen to increase as a result of the dominating but decreasing positive effective rotor resistance. The corresponding lower side band current magnitude will be governed by the effective impedance at lower frequencies and will continue to provide negative damping. It is seen that the net damping provides a local maxima at an injected frequency of 67Hz. As the injected frequency is further increased beyond 67Hz, both the positive and negative damping are seen to decrease causing the speed oscillations to decrease. It is seen that the lower side band current approaches negligible levels as the speed oscillations diminish.

Appendix C

Theory of Induced EMF Components

C.1 Per Phase Equivalent Circuit of an Induction Motor

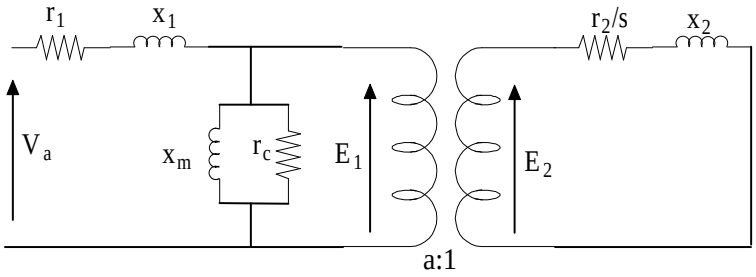

Figure C.1: Per phase equivalent circuit of an induction motor

The per phase equivalent circuit of a three phase motor used to derive the conventional equivalent circuit is illustrated in Figure C.1 where E_1 and E_2 are induced emfs in stator and rotor due to an air gap mmf that revolves at a fixed frequency where,

r_1	stator resistance
x_1	stator leakage reactance
r_2	rotor resistance
x_2	rotor leakage reactance
r_c	core loss resistance
x_m	magnetising reactance
a	stator/rotor turns ratio
V_a	rms line-to-neutral voltage of phase A
s	slip

Induced voltage in the rotor (E_2) can be written as:

$$E_2 = \frac{1}{a} s E_1 \tag{C.1}$$

where s is the slip of the motor. For a constant sinusoidal supply, the slip (s) will be constant at steady state.

C.2 Superimposed Upper Side Band (Super-synchronous) Frequency Component ($f_i = f_b + f_m$) and Fluctuations in Rotor Speed

In relation to a fluctuating supply, where a positive sequence super-synchronous frequency component ($f_i = f_b + f_m$) is superimposed on the mains frequency (f_b), line-to-neutral voltage of phase A can be expressed as:

$$v_a(t) = V_p \cos \omega_b t + V_m \cos(\omega_b + \omega_m)t \tag{C.2}$$

where,

$$\omega_b = 2\pi f_b \tag{C.3}$$

$$\omega_b + \omega_m = 2\pi(f_b + f_m) \tag{C.4}$$

Noting that the rotor speed (ω_r) is pulsating at difference frequency ω_m (i.e. corresponding to $f_i - f_b$), rotor speed can be expressed as:

$$\omega_r = \omega_{ro} + \Delta\omega \cos(\omega_m t + \phi_m) \tag{C.5}$$

where

ω_{ro} = steady state rotor speed in electrical [rad/s],

$\Delta\omega$ = amplitude of the speed fluctuations [rad/s]

Frequencies of the induced emf components on the stator and rotor due to frequency components f_b and $f_b + f_m$ are described in Sections C.3 and C.4.

C.3 Induced emf Components due to Fundamental Frequency ($\omega_b = 2\pi f_b$) in Stator

For fundamental frequency (f_b),

$$E_1 = V_{p1} \cos(\omega_b t + \phi) \tag{C.6}$$

where V_{p1} is the amplitude of E_1,

E_2 can be derived using (C.1):

$$E_2 = \frac{1}{a}(\frac{\omega_b - \omega_r}{\omega_b})V_{p1} \cos(\omega_b t + \phi) \tag{C.7}$$

Using (C.5) and (C.7):

$$E_2 = \frac{1}{a} s_o V_{p1} \cos(\omega_b t + \phi_b) - \frac{\Delta\omega}{2\omega_b a}\Big[\cos((\omega_b + \omega_m)t + \phi_b + \phi_m) + \cos((\omega_b - \omega_m) + \phi_b - \phi_m)\Big] \tag{C.8}$$

where, s_o is the steady state slip of the motor.

C.4 Induced emf Components due to Super-synchronous Frequency, $\omega_b + \omega_m = 2\pi(f_b + f_m)$ in Stator

The stator induced emf corresponding to the air gap mmf revolving at $\omega_b + \omega_m$ is:

$$E_1' = V_{m1} \cos((\omega_b + \omega_m)t + \phi_2) \tag{C.9}$$

where, V_{m1} is the amplitude of E_1'.

Corresponding rotor induced emf, E_2' is:

$$E_2' = \frac{1}{a}\Big[\frac{(\omega_b + \omega_m) - \omega_r}{\omega_b + \omega_m}\Big] V_{m1} \cos((\omega_b + \omega_m)t + \phi_2) \tag{C.10}$$

Using (C.5) and (C.10) it can be shown that:

$$E_2' = \frac{1}{a} s_o' V_{m1} \cos[(\omega_b + 2\omega_m)t + \phi_2] - \frac{\Delta_\omega V_{m1}}{2a(\omega_b + \omega_m)}\Big[\cos[(\omega_b + \omega_m)t + \phi_2 + \phi_m] + \cos[\omega_b t + \phi_2 - \phi_m]\Big] \tag{C.11}$$

where,

$$s_o' = \frac{\omega_b + \omega_m - \omega_{ro}}{\omega_b + \omega_m} \tag{C.12}$$

Equations (C.8) and (C.11) reveal that the combined effect of the rotor speed oscillations and the superimposed frequency component $(\omega_b + \omega_m)$ has resulted in two extra

emf components at angular frequencies $\omega_b - \omega_m$ and $2\omega_b + \omega_m$. Table C.1 gives the list of the dominant set of frequency components that can be found in rotor and stator for a superimposed super-synchronous frequency component.

Table C.1: Frequency components of emf components in rotor and stator caused by rotor speed oscillation at angular speed of $\omega_m = 2\pi f_m$ and a superimposed positive sequence frequency component $(2\omega_b + \omega_m)$; * extra side band frequencies

Stator applied frequency	Rotor frequency	Stator frequency
f_b (base frequency)	$(f_b - f_m) - f_r$	$f_b - f_m$ *
	$f_b - f_i$	f_b
	$(f_b + f_m) - f_r$	$f_b + f_m$
$f_b + f_m$ (upper side band)	$f_b - f_r$	f_b
	$(f_b + f_m) - f_r$	$f_b + f_m$
	$(f_b + 2f_m) - f_r$	$f_b + 2f_m$ *

Table C.1 indicates that an air gap mmf revolving at f_1 caused by the stator terminal voltage combines with oscillations in rotor speed leading to two dominant emf components corresponding to frequencies $f_1 + f_m$ and $f_1 - f_m$ in the stator. Consequently, these dominant emf components would interact with the rotor, which is oscillating at f_m, to produce further stator emf components of which the frequencies are f_m apart in the spectrum as illustrated in Figure C.2. Thus, it can be stated that in general that for a superimposed positive sequence super-synchronous frequency component (upper side band $f_i = f_b + f_m$), extra frequency components will be induced on the stator at $f_b - f_m$ and $f_b \pm 2jf_m$, where j is integer (1, 2, 3, etc.).

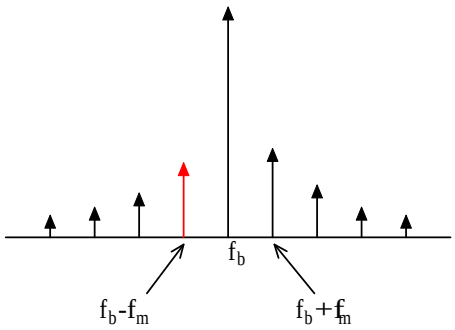

Figure C.2: Spectrum of the stator induced emf components

Comparison of various frequency components given by (C.8) and (C.11) suggests that the emf component at frequency $(f_b - f_m)$ has the largest magnitude which in fact depends on the amplitude of the rotor speed oscillations. Therefore, larger the rotor speed oscillations, larger would be the magnitude of the extra emf component that is closest to the mains frequency (f_b).

In a similar manner, for a superimposed positive sequence sub-synchronous frequency (lower side band $f_b - f_m$), extra frequency components will be induced in the stator at $f_b + f_m$ and $f_b \pm 2jf_m$ After examining the major emf components, it can be shown that $f_b + f_m$ has the largest magnitude among the other extra frequency components.

Appendix D

Derivation of $G_1(s)$ and $G_2(s)$ for the 2250hp Squirrel Cage Induction Motor

The ratings and parameters of the 2.3kV/2250hp induction motor are given in Table 4.1 in Chapter 4.

Matrices A, B and C are as follows:

$$A = \begin{bmatrix} -24.3913 & -376.9911 & 23.9766 & 0 & 0 \\ 376.9911 & -24.3913 & 0 & 23.9766 & 0 \\ 18.0956 & 0 & -18.4349 & -2.9405 & 357.6138 \\ 0 & 18.0956 & 2.9405 & -18.4349 & 55.6439 \\ 4.8634 & 0.7564 & -5.0778 & 0.0190 & -1.3712 \end{bmatrix} \tag{D.1}$$

$$B = 376.9911 \times \begin{bmatrix} 1 & 0 & 0 & 0 \\ 0 & 1 & 0 & 0 \\ 0 & 0 & 1 & 0 \\ 0 & 0 & 0 & 1 \\ 0 & 0 & 0 & 0 \end{bmatrix} \tag{D.2}$$

$$C = \begin{bmatrix} 7.035 & 0 & -6.9137 & 0 & 0 \\ 0 & 7.035 & 0 & -6.9137 & 0 \end{bmatrix} \tag{D.3}$$

Substituting A, B and C in (4.35), along with G defined by (4.30),

$$G_1(s) = \frac{\Delta i_{qs}}{\Delta v_s} = \frac{k_1(s^4 + a_3 s^3 + a_2 s^2 + a_1 s + a_0)}{s^5 + b_4 s^4 + b_3 s^3 + b_2 s^2 + b_1 s + b_0} \tag{D.4}$$

where,

$$\begin{aligned} k_1 &= 2651.57 & b_4 &= 87.02336 \\ a_3 &= 44.845 & b_3 &= 1.4593 \times 10^5 \\ a_2 &= 213.26 & b_2 &= 5.5177 \times 10^6 \\ a_1 &= -7.733 \times 10^4 & b_1 &= 3.1567 \times 10^8 \\ a_0 &= -1.777 \times 10^6 & b_0 &= 4.7028 \times 10^9 \end{aligned}$$

$$G_2(s) = \frac{\Delta i_{ds}}{\Delta v_s} = \frac{k_2(s^3 + c_2 s^2 + c_1 s + c_0)}{s^5 + b_4 s^4 + b_3 s^3 + b_2 s^2 + b_1 s + b_0} \tag{D.5}$$

where,

$$k_2 = 9.9962 \times 10^5$$

$$c_2 = 19.607$$

$$c_1 = 1805.72$$

$$c_0 = -1.230 \times 10^3$$

Appendix E

Aggregation of Induction Motors for Flicker Studies

E.1 Introduction

The literature suggests [41, 42] that aggregation of induction motor loads for dynamic performance studies can be carried out using various methods. Most of the existing methods that have been developed are intended for investigations in relation to power system stability studies where the duration of the investigation is of a few milliseconds, where one or more aggregate motors are used to represent the total motor load at load busbars.

In [41], the third order induction motor model commonly used for transient stability studies to model the equivalent aggregate motor. Weighted average method is used to derive electrical and mechanical parameters of the aggregate machine including transient reactance (X'), rotor open circuit time constant (T_o), and inertia constant (H).

In [43], an aggregate induction motor based on the conventional steady state equivalent circuit and the steady state operation is presented. Condition to be satis-

fied is power invariance. Representation of a composite load of induction motors and passive loads which are interconnected in an arbitrary network by a single equivalent motor and a single passive load is discussed in [44]. A method based on weighted averages of machine parameters is used in [45] where the assumptions made in deriving equivalent circuit are valid for when the individual motors are at stand still. Refined methods of motor aggregation are described in [42, 46]. In [42], the steady state equivalent circuit of the aggregate machine is identified using locked-rotor and no-load conditions of individual motors.

Although it would be possible to use one of the methods stated above to aggregate the induction motors in relation to flicker studies, a simple yet reasonably accurate method is presented in this appendix. The proposed method is based on the steady state equivalent circuit and was employed in Chapter 7 in aggregating motor loads in small signal analysis. Determination of electrical and mechanical parameters and the steps involved in the development of the proposed aggregate machine are given for a case where only two individual machines are considered.

E.2 A Method based on Steady State Equivalent Circuit Theory

E.2.1 Determination of Electrical Parameters

Conventional per phase equivalent circuit of a three phase induction motor (called first induction motor) is shown in Figure E.1, where Z_{11}, Z_{12} and Z_{13} represent stator impedance, rotor impedance and the magnetising impedance (ignoring the core losses) give by:

$$Z_{11} = r_{s1} + jx_{s1} \tag{E.1}$$

$$Z_{21} = r_{r1} + jx_{r1} \tag{E.2}$$

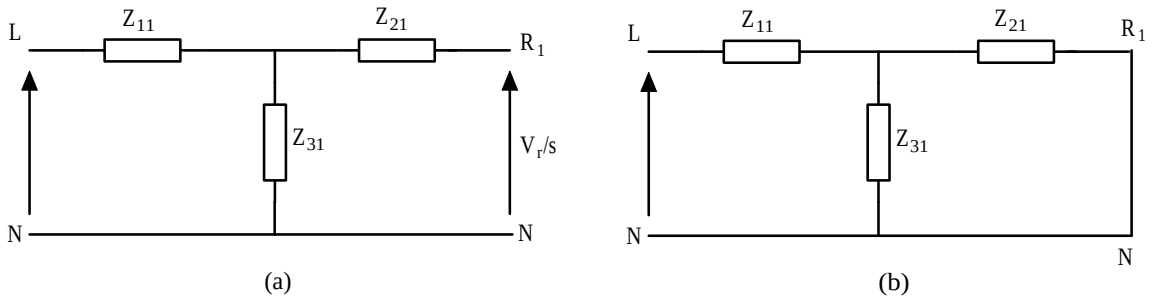

Figure E.1: Per phase equivalent circuits of the first induction motor (T-model)

$$Z_{31} = jx_{m1} \tag{E.3}$$

For a squirrel cage induction motor Figure E.1(a) can be redrawn as illustrated in Figure E.1(b) where the rotor is short circuited. The impedances in stator, rotor and magnatising branches of Figure E.1(a) can be converted into three impedances connected in delta form (Π-model) as shown in Figure E.2.

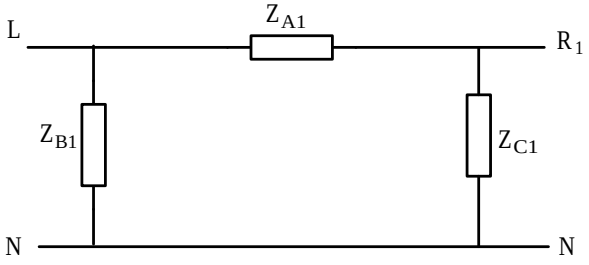

Figure E.2: Per phase equivalent circuit of the first induction motor (Π-model)

Impedances in Figure E.2 are determined as:

$$Z_{A1} = \frac{Z_{11}Z_{21} + Z_{21}Z_{31} + Z_{31}Z_{11}}{Z_{31}} \tag{E.4}$$

$$Z_{B1} = \frac{Z_{11}Z_{21} + Z_{21}Z_{31} + Z_{31}Z_{11}}{Z_{21}} \tag{E.5}$$

$$Z_{C1} = \frac{Z_{11}Z_{21} + Z_{21}Z_{31} + Z_{31}Z_{11}}{Z_{11}} \tag{E.6}$$

The effective impedance of the motor looking into the stator from its terminals

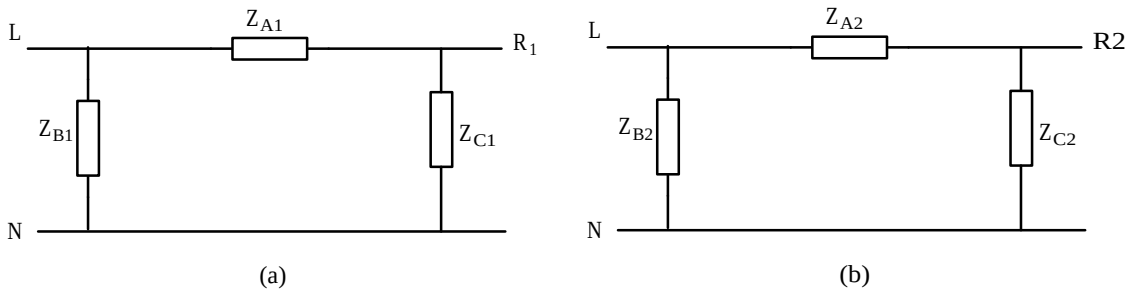

Figure E.3: Equivalent circuits of the both motors

(Z_{LN}) can be derived from the circuit in Figure E.2 by setting Z_{C1} to zero as below:

$$Z_{LN} = Z_{A1}//Z_{B1} = \frac{\frac{\left[Z_{11}Z_{21}+Z_{21}Z_{31}+Z_{31}Z_{11}\right]^2}{Z_{31}Z_{21}}}{\left[\frac{Z_{11}Z_{21}+Z_{21}Z_{31}+Z_{31}Z_{11}}{Z_{31}}\right]+\left[\frac{Z_{11}Z_{21}+Z_{21}Z_{31}+Z_{31}Z_{11}}{Z_{21}}\right]}$$

which is equal to:

$$Z_{LN} = Z_{11} + [Z_{21}//Z_{31}] \tag{E.7}$$

Similarly, impedance branches of the second motor can be transformed into its equivalent delta impedances as described using (E.8)-(E.10) and illustrated in Figure E.3(b):

$$Z_{A2} = \frac{Z_{12}Z_{22} + Z_{22}Z_{32} + Z_{32}Z_{12}}{Z_{32}} \tag{E.8}$$

$$Z_{B2} = \frac{Z_{12}Z_{22} + Z_{22}Z_{32} + Z_{32}Z_{12}}{Z_{22}} \tag{E.9}$$

$$Z_{C2} = \frac{Z_{12}Z_{22} + Z_{22}Z_{32} + Z_{32}Z_{12}}{Z_{12}} \tag{E.10}$$

For the two motors noting that nodes R_1 and R_2 will be at same potential,

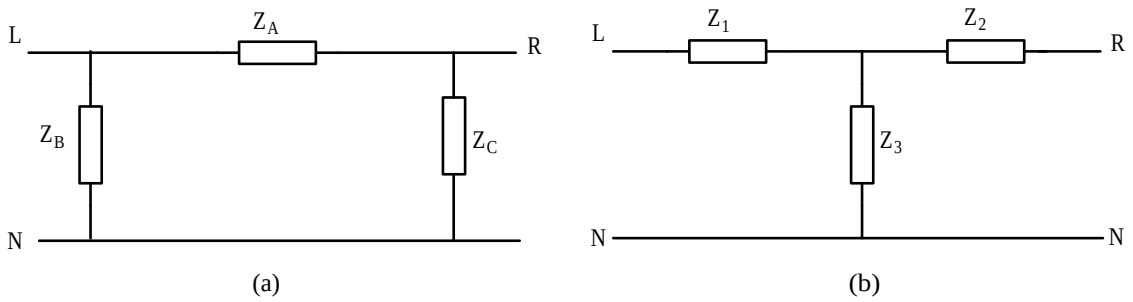

Figure E.4: Hypothetical equivalent circuit of the aggregate machine

$Z_{A1}, Z_{A2}, Z_{B1}, Z_{B2}, Z_{C1}$ and Z_{C2} can be combined as described by (E.11)-(E.13).

$$Z_A = Z_{A1}//Z_{A2} \tag{E.11}$$

$$Z_B = Z_{B1}//Z_{B2} \tag{E.12}$$

$$Z_C = Z_{C1}//Z_{C2} \tag{E.13}$$

Figure E.4 depicts the equivalent circuit of the aggregate machine deduced using (E.11)-(E.13). Stator, rotor and magnatising impedances (Z_1, Z_2 and Z_3) of the aggregate machine can be derived by transforming Z_A, Z_B and Z_C into equivalent star connected impedances as given by: (E.14)-(E.16).

$$Z_1 = \frac{Z_A Z_B}{Z_A + Z_B + Z_C} \tag{E.14}$$

$$Z_2 = \frac{Z_A Z_C}{Z_A + Z_B + Z_C} \tag{E.15}$$

$$Z_3 = \frac{Z_B Z_C}{Z_A + Z_B + Z_C} \tag{E.16}$$

Z_1, Z_2 and Z_3 can be described as per (E.17)-(E.18). The operating slip (s) of the aggregate motor is embedded in (E.18).

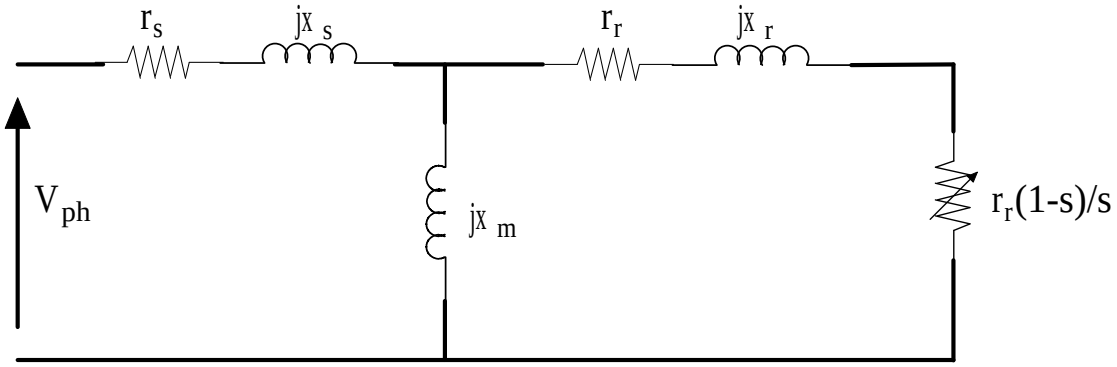

Figure E.5: Steady state equivalent circuit of the aggregate motor

$$Z_1 = r_s + jx_s \tag{E.17}$$

$$Z_2 = \frac{r_r}{s} + jx_r \tag{E.18}$$

$$Z_3 = jx_m \tag{E.19}$$

The steady state equivalent circuit of the aggregate motor is shown in Figure E.5.

E.2.2 Determination of Steady State Slip

The steady state slip of the aggregate machine is determined using the equivalence of the output power of the two individual machines and the aggregate machine as described below.

$$P_{out} = 3\Big(\frac{1-s}{s}\Big)R_r|I_r|^2 \tag{E.20}$$

$$I_r = \frac{V_{ph}}{Z}\Big[\frac{jx_m}{jx_m + (\frac{r_r}{s} + jx_r)}\Big] \tag{E.21}$$

where

$$Z = (r_s + jx_s) + (jx_m//(\frac{r_r}{s} + jx_r)) \tag{E.22}$$

Ideally the total output power of the two individual motors (P_{out1} and P_{out2}) should be equivalent to the output power of the aggregate machine ($P_{out-agg}$).

$$P_{out-agg} = P_{out1} + P_{out2} \tag{E.23}$$

From (E.20), (E.21) and (E.23),

$$P_{out-agg} = \left| \frac{V_{ph}}{(r_s + jx_s) + (jx_m//(\frac{r_r}{s} + jx_r))} \times \frac{jx_m}{jx_m + (\frac{r_r}{s} + jx_r)} \right|^2 = P_{out1} + P_{out2} \tag{E.24}$$

By solving (E.24) unknown s, the operating slip of the aggregate motor can be calculated.

E.2.3 Determination of Inertia

Inertia of the aggregated motor is determined using the principle of kinetic energy conservation as described by (E.25).

$$J_{agg} = \frac{\sum J_i {\omega_i}^2}{{\omega_{agg}}^2} \tag{E.25}$$

where J_i and ω_i are inertia of motor i respectively.

E.2.4 Determination of Load Torque Characteristics

Speed-torque characteristics of the effective load of the aggregate motor can be determined using the following procedure, which takes the torque-speed characteristics of the individual machines into account.

1. Simulate the individual machines using a suitable time domain analysis software (such as PSCAD/EMTDC or Simulink).

2. For each motor, find the electromagnetic torque (T_e), the load torque (T_L) and the rotor speed (ω_1) for the time instance (t_1) while machine is accelerating to steady state. These parameters (T_e, T_L and ω_1) quantifies the output electromagnetic power of the individual machines for the time instance considered as described below.

$$P_{out1-t1} = T_{e1}\omega_1 \tag{E.26}$$

$$P_{out2-t1} = T_{e2}\omega_2 \tag{E.27}$$

   In (E.26) and (E.27) subscripts 1 and 2 denote induction motor-1 and 2 respectively.

3. The total output electromagnetic power of the two machines is determined using the corresponding power outputs of the individual machines as per:

$$P_{out-total} = P_{out1-t1} + P_{out1-t2} \tag{E.28}$$

4. Using (E.28) and (E.20), determine the slip at $t = t_1$ and hence rotor speed of the aggregate machine.

5. Power required by the mechanical load of each motor given by (E.29) and (E.30) are used to determine the power required by the aggregate motor as per (E.31).

$$P_{L1} = T_{L1}\omega_1 \tag{E.29}$$

$$P_{L2} = T_{L2}\omega_2 \tag{E.30}$$

$$P_{L-agg} = P_{L1} + P_{L2} \tag{E.31}$$

E.2.5 Criterion for Aggregation of Individual Motors

Literature suggests that it is not possible to represent all individual motors by a single equivalent aggregate motor [41, 46]. This is due to diversity in dynamic characteristics of motors of various ratings. It has been noted that the open circuit rotor time constant (T'_o) and inertia constant (H) are the key parameters that influence the dynamic behaviour of an induction motor. In this regard [41] suggests that the criterion for aggregating the various machines into a single machine is possible for a group of machines that fulfill:

$$H > \frac{1}{2}T'_o \tag{E.32}$$

The above criterion is employed in deciding on the motors to be aggregated for the work covered in Section E.3 where two examples are illustrated in detail.

E.3 Implementation

E.3.1 Case I: Aggregation of two induction motors

Table E.1 gives the ratings and parameters of two low voltage induction motors that are used by Kataoka in [42] for aggregation. Those two motors are aggregated into a single equivalent motor using the method proposed in this appendix.

Table E.2 gives a comparison of the estimated per phase equivalent circuit parameters and the inertia of the aggregate motor using the proposed method and those determined using method described in [42]. The results of Table E.2 indicate that the proposed method has produced results that are compatible with the method in [42].

Table E.1: Ratings and parameters of individual motors: Case I

Ratings/ Parameters	motor-1	motor-2
Output power, P [kW]	3.7	2.2
Voltage, V [V]	380	200
Frequency, f [Hz]	50	50
Pole pair number, p	3	2
stator resistance, r_s	1.40Ω	0.825 Ω
rotor resistance, r_r	2.00Ω	0.612Ω
stator leakage inductance, L_s	5.77mH	3.15mH
rotor leakage inductance, L_r	6.41mH	3.15mH
magnetising inductance, L_m	217.0mH	94.0mH
slip, s	0.03	0.02
Inertia constant, H	1.23	0.509

Figure E.6 depicts the electromagnetic torque (T_e) and the load torque (T_L) characteristics predicted using the aggregated motor.

E.3.2 Case II: Aggregation of Group of Induction Motors

Table E.3 gives the ratings and parameters of thirteen 415V, 50Hz induction motors, the second set of test motors used.

Table E.4 gives the per phase equivalent circuit parameters of the aggregated motor that represents the total induction motor load of 13 motors. Table E.5 gives the input real and reactive power and power factor of the aggregated motor compared with those obtained with the thirteen motors operating as individual motors where a good agreement is seen.

The response of the aggregated motor to sudden and regular changes of the supply voltage was examined. Figure E.7 shows the response of active power (P) and reactive power (Q) of aggregate motor and the total motor load to a reduction of 0.2pu

Table E.2: Electrical and mechanical parameters of the aggregate motor established using the proposed method and Kataoka's method: Case I - aggregation of two low voltage machines

Parameter	Kataoka's method	Proposed method
r_s	0.972Ω	0.969 Ω
r_r	1.09Ω	1.0892Ω
L_s	3.85mH	3.86mH
L_r	4.11mH	4.095mH
L_m	132.0mH	132.37mH
s	0.0263	0.0262
J	0.459	0.5258

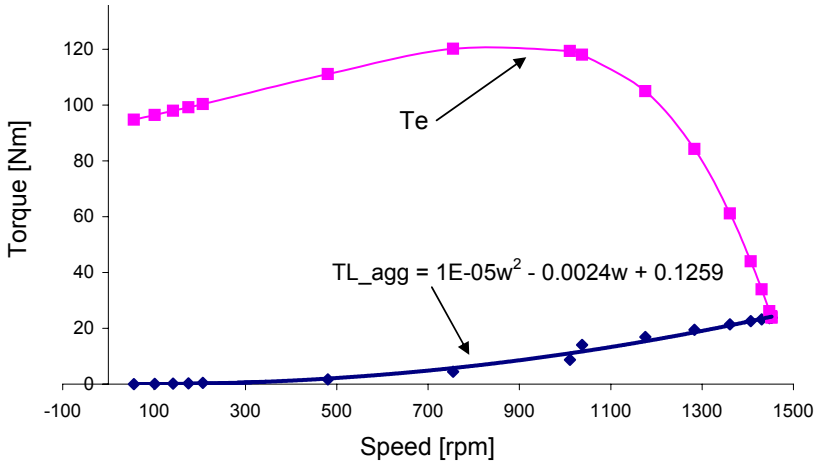

Figure E.6: Electromagnetic torque (T_e) and load torque ($T_{L_{agg}}$) characteristics of the aggregate induction motor

Table E.3: Ratings and parameters of individual motors: Case II

Motor Identity	Output Power [hp], pole pair number	Rated current, I_{rated} [A]	Power factor, pf	Efficiency, η	Inertia J, [kgm^2]
1	150hp 6p	205	0.8	0.93	4.5366
2	125hp 6p	165	0.84	0.927	3.273
3	100hp 6p	132	0.84	0.924	2.8469
4	75 hp 6p	100	0.83	0.921	2.4809
5	60hp 6p	80	0.85	0.917	2.2065
6	200hp 4p	250	0.87	0.94	3.2898
7	175hp 4p	215	0.89	0.938	3.2898
8	150hp 4p	200	0.84	0.935	2.5491
9	125hp 4p	162	0.85	0.93	2.1882
10	100hp 4p	130	0.87	0.928	1.8143
11	75hp 4p	96	0.86	0.925	0.9303
12	60hp 4p	78	0.88	0.92	0.7717
13	50hp 4p	65	0.87	0.915	0.6631

Table E.4: Electrical and mechanical parameters of aggregate motor

Parameter	Value
r_s	0.0045 Ω
r_r	0.00402 Ω
x_s	0.0064 Ω
x_r	0.0091 Ω
x_m	0.3622 Ω
s	0.02751
J	22.284 kgm^2

Table E.5: Comparison of the input power of aggregate machine and the group of individual machines at full load steady state operation

Parameter	Combination of individual motors	Aggregate motor	Error [$\frac{x_{agg}-x_{com}}{x_{com}}$ x:variable;]
Real power, P	1.0899 MW	1.0696 MW	1.9%
Reactive power, Q	0.5283 MVAr	0.5393 MVAr	2.052%
Power factor	0.9048	0.891	1.55%

in supply voltage. The transient variations and recovery of P and Q of the aggregate motor indicate that the aggregate motor is capable of replicating the dynamic characteristics of the total motor load with a reasonable accuracy.

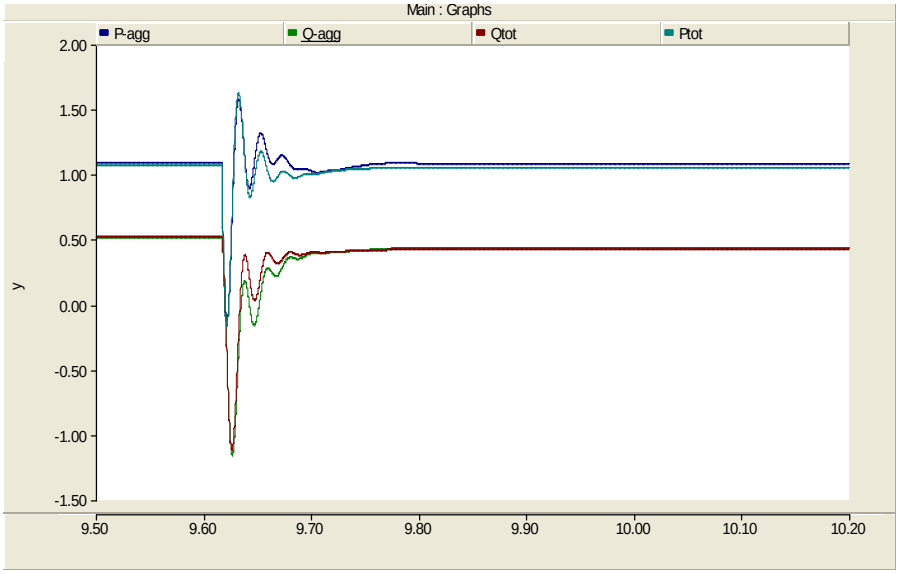

Figure E.7: Comparison of the response of the aggregate motor and the cluster of individual motors to a step change of 0.2pu in the supply voltage

Figure E.8 and E.9 depict variations in supply P and Q for voltage fluctuations of low frequencies (5Hz and 10Hz). A good agreement can be seen between the aggregate motor and the total motor load.

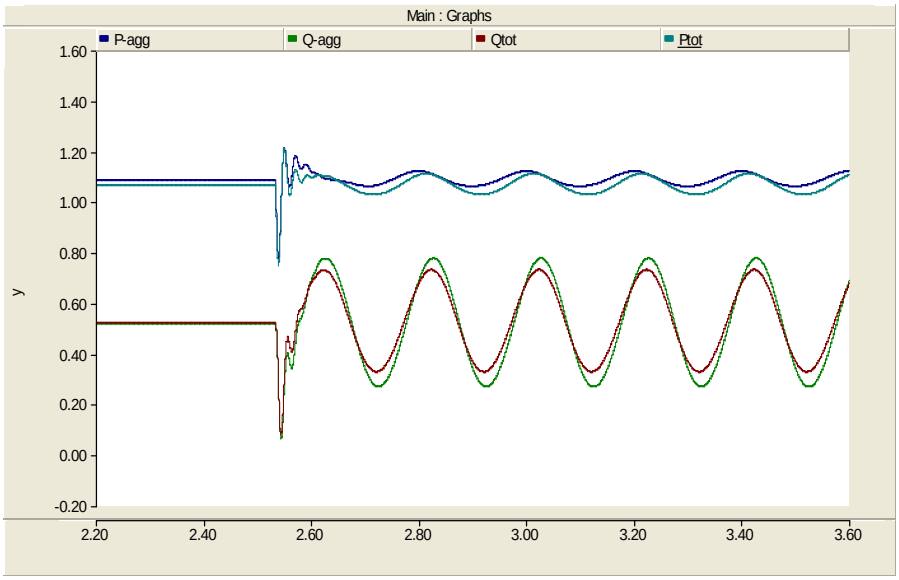

Figure E.8: Comparison of the response of the aggregate motor and the cluster of individual motors to a sinusoidal fluctuation in the supply; frequency of voltage fluctuation=5Hz

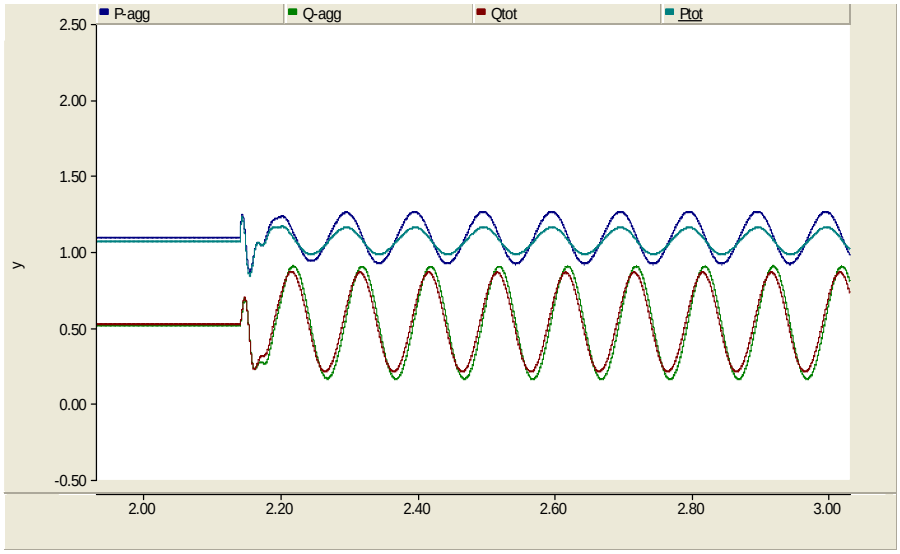

Figure E.9: Comparison of the response of the aggregate motor and the cluster of individual motors to a sinusoidal fluctuation in the supply; frequency of voltage fluctuation=10Hz

The aggregate motor was also examined in relation to its response to the flickermeter when the motor was connected to a sinusoidally amplitude modulated supply of fixed modulation depth and variable modulation frequency through an inductive line impedance. Instantaneous flicker sensation (P_{it}) measured at the source and load ends are used to determine the flicker transfer coefficient (T_{Pst}) from the source to load end for different modulation frequencies (f_m). Simulations were repeated for the cluster of motors as well.

Figure E.10 illustrates the variation of T_{Pst} with modulation frequency (f_m) established for the aggregate motor and combination of individual motors. The absolute error involved in T_{Pst} of the aggregate motor with respect to the cluster of individual motors is given in the bar chart of Figure E.11. Figures E.10 and E.11 suggests that in relation to the flicker attenuation, the aggregate motor exhibits a maximum absolute error about 5.2%. However error becomes negligible for relatively high modulation frequencies.

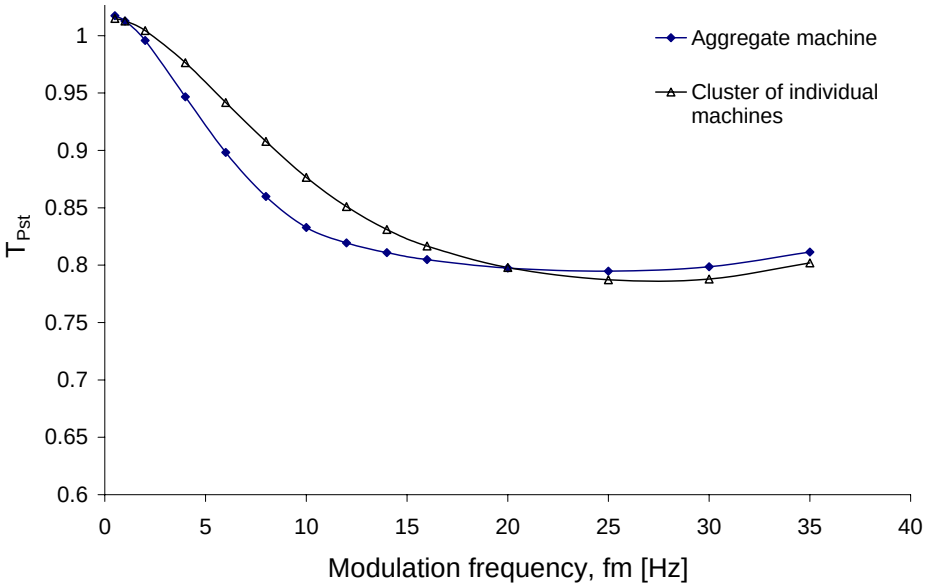

Figure E.10: Variation of T_{Pst} with modulation frequency (f_m) for aggregate induction motor and the cluster of individual motors

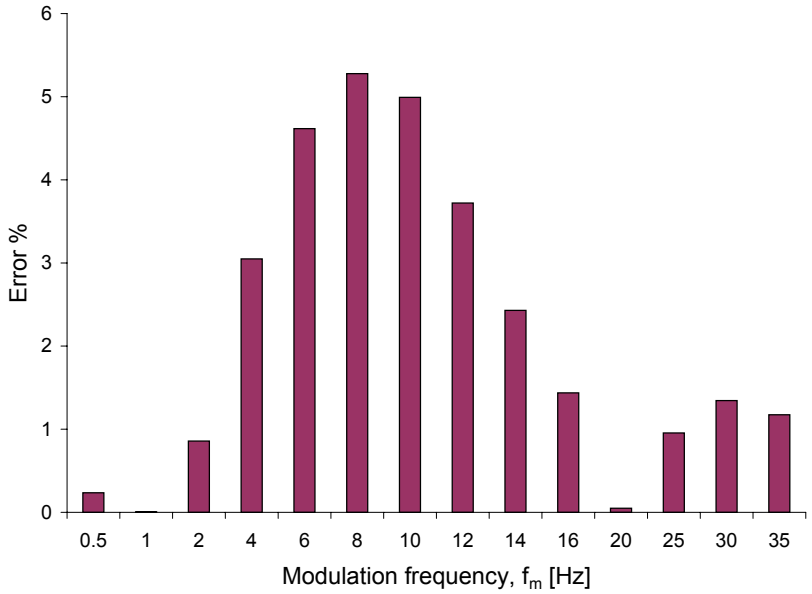

Figure E.11: Error involved in T_{Pst} established for the aggregate machine

Appendix F

Aggregation of 35 500hp Induction Motors

Table F.1: Ratings and parameters of an individual 500hp motor

Parameter	Value
V_{rated}	2.3kV Ω
r_s	0.262 Ω
r_r	0.187 Ω
x_s	1.206 Ω
x_r	1.206 Ω
x_m	54.02 Ω
s	0.015
J	11.06 kgm^2

The rated voltage of an individual motor (500hp) is 2.3kV and hence the equivalent circuit parameters will be converted into operating voltage of the IEEE 14 bus system (33kV) before modelling the aggregate motor as a matrix of transfer function.

Table F.2: Electrical and mechanical parameters of the aggregate motor representing 35 individual motors

Parameter	Value
r_s	0.00748 Ω
r_r	0.00365 Ω
x_s	0.034457 Ω
x_r	0.034457 Ω
x_m	1.54343 Ω
s	0.0103
J	383.406 kgm^2

Appendix G

IEEE 14 Bus System Data

Table G.1: Generator and load bus data

Bus	Generation		Load	
Number	MW	MVAr	MW	MVAr
1 (reference bus)	0	0	0	0
2	40	0	21.7	12.7
3	0	0	94.2	19.0
4	0	0	47.8	3.9
5	0	0	7.6	1.6
6	0	0	11.2	7.5
7	0	0	0	0
8	0	0	0	0
9	0	0	29.5	16.6
10	0	0	9.0	5.8
11	0	0	3.5	1.8
12	0	0	6.1	1.6
13	0	0	13.5	5.8
14	0	0	14.9	5.0

Table G.2: Transmission Line and Transformer Data; Impedances and line charging susceptance in pu on a 100MVA base

Line	Resistance pu	Reactance degrees	Line Charge pu
1-2	0.01938	0.05917	0.0264
1-5	0.05403	0.22304	0.0246
2-3	0.04699	0.19797	0.0219
2-4	0.05811	0.17632	0.0187
2-5	0.05695	0.17388	0.0170
3-4	0.06701	0.17103	0.0173
4-5	0.01335	0.04211	0.0064
4-7	0	0.20912	0
4-9	0	0.55618	0
5-6	0	0.25202	0
6-11	0.09498	0.19890	0
6-12	0.12291	0.25581	0
6-13	0.06615	0.13027	0
7-8	0	0.17615	0
7-9	0	0.11001	0
9-10	0.03181	0.08450	0
9-14	0.12711	0.27038	0
10-11	0.08205	0.19207	0
12-13	0.22092	0.19988	0
13-14	0.17093	0.34802	0

Table G.3: Voltage-controlled bus data

Bus Number	Voltage magnitude [pu]	Minimum MVAr capability	Maximum MVAr capability
2	1.045	40	50
3	1.010	0	40
6	1.070	6	24
8	1.090	6	24

Table G.4: Tap settings of fixed-tap transformers

Transformer Number	Tap setting
4-7	1.022
4-9	1.032
5-6	1.073

Table G.5: Static capacitor data; Susceptance in pu on a 100MVA base

Bus Number	Susceptance [pu]
9	0.19